The Influence Of Microstructure On The Corrosion And Wear Mechanisms Of High Chromium White Irons In Highly Caustic Solutions

G. D. Nelson

School of Mechanical Engineering
The University of Adelaide
South Australia

December 2010

Preface

Wear is a significant problem faced in many industries, and replacement of worn parts can result in considerable costs arising from the cost of the replacement component, labour, loss of production time and reduced productivity from capital equipment. To minimize these costs and attendant downtime of equipment, wear resistant materials are commonly used in high wear environments. One of the most commonly used group of materials for wear resistance are high chromium white irons (AS/NZS 2576:1996).

High chromium white irons may be deposited by welding onto a softer, tougher substrate or used as castings. When deposited by welding the deposit is termed a weld overlay and the process is known as hardfacing. Castings may be used in either the as-cast condition or they may be heat-treated prior to use. The high chromium content of these alloys also provides a degree of corrosion resistance, which coupled with their resistance to abrasive and erosive wear resistance makes them suitable for use in many mineral processing industries (Dogan and Hawk, 1995, Tabrett et al., 1996).

The wear resistance of these alloys is due to their microstructure which comprises hard, wear resistant carbides dispersed in a softer metal matrix. The microstructure of these alloys, and hence the wear performance, is related to the size and distribution of the hard wear resistant carbides, i.e. the carbide morphology, within the microstructure and this depends on both the chemical composition of the alloy and the cooling rate of the alloy from its molten state (Powell, 2002). High cooling rates, generally associated with weld deposits and weld overlays, results in a microstructure that differs substantially from that commonly reported in the literature for castings of similar composition.

High chromium white irons, in the form of weld overlays, are currently used in Australia to line the inside surface of pipelines and fittings used for the transfer of slurries in the early stages (known as the red side) of the alumina refining process. These slurries are highly alkaline and contain a high volume fraction of abrasive quartz (silica sand) particles resulting in wear due to corrosion and erosion. This leads to the premature, and often unpredictable failure of plant components. Weld overlayed pipe sections are generally located in regions subject to high levels of wear, for example adjacent to pumps and valve inlets and outlets, to reduce wear.

Arnold et al. (1998) investigated the wear of high chromium white iron weld overlays in alumina plants. This investigation found that the wear of the weld overlays was due to two mechanisms, abrasive-erosive wear and corrosive wear. The independent contributions of each of these wear mechanisms and any synergistic effects to the total wear, although identified as being very important, were not determined.

A definitive study into these wear mechanisms in high chromium white iron castings and weld overlays was initiated. A collaboration between the major Alumina refineries in Australia, through the joint Welding Technology Institute of Australia (Panel 8 Reclamation),

and the Cooperative Research Centre (CRC) for Welded Structures was formed. The purpose of the thee year research program was to develop an erosion corrosion model which will enable the most appropriate high chromium white iron hardfacing alloy to be selected for a given set of operating conditions on the red side of an alumina plant, minimizing the risk of component failure and downtime.

It was proposed that, following a review of the literature and site visits to several alumina refineries, plant samples of castings and weld overlay components removed from several refineries would be acquired and a detailed examination of their principal features undertaken. There appeared, at this stage, to be little detail on the relationship between the microstructure of the high chromium white irons and the wear mechanisms in the conditions encountered on the red side of alumina refineries.

The following stage would consist of producing a range of experimental alloys with different microstructures through changes in alloy chemical composition, cooling rate and heat-treatment.

Prepared plant samples and experimental alloy samples would be corrosion tested using a potentiostat in solutions and conditions approximating those encountered in the red side of the alumina refinery. These experiments would provide information on the influence of the phases present, the chemical composition of the phases present and their morphology on the corrosion behavior.

Samples of the alloys used for the corrosion tests would be slurry pot tested. The slurry pot tests use the same liquor as used in the corrosion tests but to which abrasive quartz particles have been added. The quartz particles are approximately the same size and distribution as the particles entrained in the liquor on the red side of the alumina refinery. The liquor impinges on the surface of the samples at velocities and angles representative of conditions found in the refineries. These experiments will provide information on the synergistic effect of the impingement of abrasive particles entrained in the corrosive liquor.

A detailed characterization of the plant samples and experimental alloys has been performed, so that together with the results from the corrosion and erosion-corrosion tests mentioned above, a model for the wear mechanism encountered on the red side of the alumina refining process has been developed. This model provides a basis for the selection of high chromium white irons for use in these sections of the alumina refining operation. The results from this investigation also have relevance to other areas of the alumina refining plant and other industries that pump erosive-corrosive slurries.

Part I

Literature Survey

Chapter 1

Literature Survey

1.1 Introduction

It is important that the wear mechanism occurring in a particular wear environment be understood to facilitate the selection of materials to minimize wear. There are many different types of wear mechanisms, with examples including erosive wear, corrosive wear, abrasive wear, adhesive wear, fretting and surface fatigue (MTIA, 1986). It is common for these wear mechanisms to act simultaneously to form a complex wear environment which may have a significantly greater wear rate than the sum of the individual wear components. An example is erosive wear in a corrosive environment resulting in an erosion-corrosion wear mechanism.

In this review, therefore, a brief outline of the alumina refining process is presented to establish the operating environment for the high chromium white iron wear materials. This is followed by a review of the microstructures and the factors that influence the development of microstructures in high chromium white iron castings and weld deposits.

Previous investigations of hardfaced pipes used in the early stages (or red side) of the alumina refining process have suggested that the in service wear was due to a combination of erosive, abrasive and corrosive wear mechanisms (Arnold et al., 1998). These wear mechanisms are also reviewed.

1.2 Industrial Bayer Process

The demand for alumina, the raw material for aluminium production, is continuously increasing due to the increasing world consumption of aluminium with the production of alumina reaching 46.8 mega tonnes worldwide at the end of 1997 (Hind et al., 1999). Australia is the worlds largest producer of alumina providing just below 30 percent of annual world production (Hind et al., 1999). Alumina is produced using the Bayer refining process, which is a

method of extracting gibbsite (alumina trihydrate, $Al_2O_3.3H_2O$) from bauxite ore (Winkhaus, 1989). The Bayer process is cyclic and involves four main steps, digestion, clarification, precipitation and calcination, Figure 1.1.

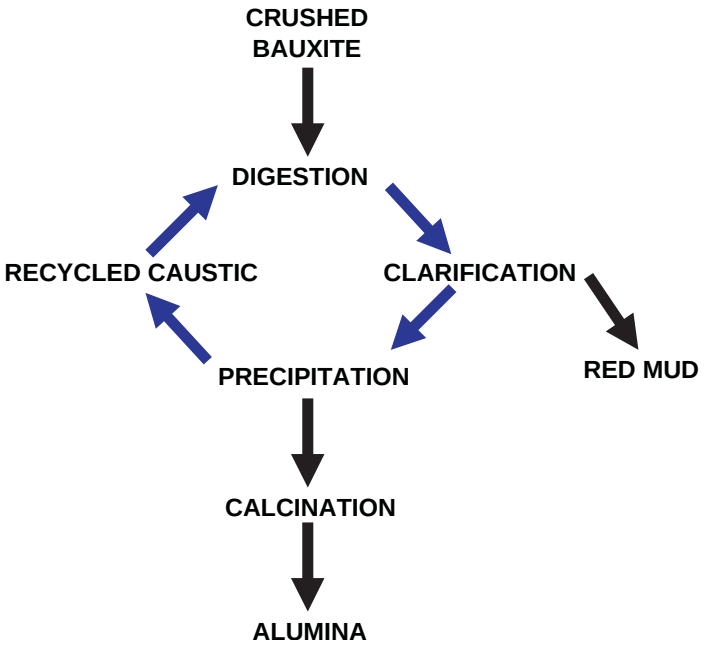

Figure 1.1: Flow diagram of the Bayer process showing the cyclic nature.

The first stage, digestion involves the dissolution of crushed bauxite ore in caustic soda (sodium hydroxide) solution to dissolve the alumina rich component of the ore, Equation 1.1.

$$Al_2O_3.xH_2O + 2NaOH \rightarrow 2NaAlO_2 + (x+1)H_2O \tag{1.1}$$

Bauxite (hydrated alumina) + caustic soda $\rightarrow$ sodium aluminate + water

Varying caustic concentrations, and high temperatures and pressures achieved by the use of high-pressure steam, accelerate this dissolution process. Depending on the grade of bauxite, the digestion temperatures can be of the order of 145°C and caustic solutions of 4-5 M sodium hydroxide concentration (Hind et al., 1999). For lower grade bauxite ores, digestion temperatures can be between 170-265°C and caustic solution concentrations up to 7 M sodium hydroxide. At the completion of the digestion process, a slurry having a liquor phase rich in dissolved alumina and a solid phase of insoluble particles is produced. The insoluble particles are principally particles of silica and oxides of iron and titanium (Queensland Alumina Limited, 2003). Prior to the next processing operation the slurry is flash cooled to atmospheric boiling point in a series of flash tanks operating at successively lower pressures.

The second stage is clarification. This involves the separation of the undissolved solid impurities from the liquor phase. This is done via a settling process with the aid of flocculants to

improve settling rates (Queensland Alumina Limited, 2003). A final filter is used to remove any fine impurities to produce a clear liquor of supersaturated sodium aluminate.

The precipitation stage is the next process of the cycle and involves the precipitation of gibbsite (hydrated alumina) from the supersaturated sodium aluminate solution, Equation 1.2. This is achieved by seeding the supersaturated solution with fine recycled crystals of gibbsite followed by cooling (Hind et al., 1999).

$$2NaAlO_2 + 4H_2O \rightarrow Al_2O_3.3H_2O + 2NaOH \tag{1.2}$$

Sodium aluminate + water → hydrated alumina + caustic soda

The gibbsite from the precipitation stage is removed when it has reached an appropriate size and is washed prior to calcination. Calcination removes any residual moisture and the chemically combined water, Equation 1.3. The resulting product is alumina, which resembles dry white sand.

$$Al_2O_3.3H_2O \rightarrow Al_2O_3 + 3H_2O \tag{1.3}$$

Hydrated alumina → alumina + water

The alumina processing plant is commonly divided into the red side and white side based on the constituents entrained within the slurry. The red side refers to the digestion and clarification processes where the slurry contains high proportions of silica and oxides of iron and titanium. Iron oxide is responsible for the red appearance of the slurry. Once the clarification stage is complete, the slurry no longer contains undissolved particles and from then onwards the processing plant is referred to as the white side

Wear of the pipelines and slurry pumps used to transfer the slurry between process stages on the red side of the alumina refining possess in areas such as the flash tanks is particularly common. This is due to the higher proportion of abrasive silica particles entrained within the slurry compared to other locations in the plants. To reduce the severity of the erosive wear and to prolong service life of the slurry pipelines (referred to as spools) and slurry pumps, the pipelines are commonly weld overlayed on their internal surface with high chromium white irons and pumps are commonly cast out of high chromium white iron. High chromium white iron is used because of its resistance to abrasive, erosive wear and economical cost. However, the slurry, which contains the hot alkaline Bayer liquor, is responsible for an undetermined amount of corrosion of the hardfacing overlays and castings and makes the environment both erosive and corrosive.

1.3 Microstructure of High Chromium White Irons

1.3.1 Introduction

The microstructure of high chromium white irons determines properties such as the mechanical properties and wear performance. Thus, it is fundamental to understand the microstructural development of white iron alloys to determine the relationships between microstructure and mechanical properties to enable the development of superior alloys.

A white iron can be considered a cast iron that generally contains no graphite (AS 2027: 2002). However, this review will specifically concentrate on the commercially produced high chromium white iron alloys which, in the past, have typically contained 11-30 wt% chromium and 1.8-3.6 wt% carbon and form the M_7C_3 type chromium carbides (Tabrett et al., 1996). Currently, due to a more thorough understanding of microstructural development and careful foundry practices, high chromium white irons are being commercially produced with carbon compositions in excess of 4.5 wt% and chromium in excess of 30 wt% (Llewellyn and Dolman, 2004). The general range of chemical compositions for high chromium white irons contains sufficient alloying additions to ensure no graphite is produced during solidification, i.e. the graphite eutectic reaction associated with conventional cast irons does not occur.

This review will cover the solidification of the iron-chromium-carbon (Fe-Cr-C) high chromium white irons with reference to the ternary phase diagram and the relationship between chemical composition and microstructure and heat treatments.

1.3.2 Classification of High Chromium White Irons

1.3.2.1 High Chromium White Iron Casting Alloys

High chromium white iron castings, commonly referred to as abrasion resistant castings, are generally specified according to their chemical composition and hardness. The most recent Australian standard, AS 2027: 2007, has adopted the the ISO 21988: 2006 classification of high chromium white irons and covers five grades ranging in chromium contents from 11 to 40 wt%. The designation and chemical composition ranges of high chromium cast irons are given in Table 1.4. Other international standards such as ASTM A532/A532M-93a: 1999 have similar designations with respect to the chromium composition range but differ in the minimum and maximum amount of additional alloying elements. Table 1.5 shows the different designation of high chromium abrasion-resistant cast irons cross-referenced with other international standards. The most notable difference between the AS 2027: 2007 (adopted from ISO 21988: 2006) together with the previously superseded AS 2027: 2002 standard is the inclusion of ISO 21988/JN/HBW600XCr35 or Cr 35 designation. This particular designation refers to a high chromium cast iron having a chromium and carbon content in the

range of 30 to 40 wt% and 3.0 to 5.5 wt% respectively. These chromium and carbon contents are well above what is specified in other standards (e.g. ASTM A532: 1999).

Table 1.4: Brinell hardness and chemical composition of high chromium abrasion-resistant cast irons (AS 2027: 2007).

Material designation Symbol	Brinell Hardness HBW min	Chemical composition in % (mass fraction)								
		C	Si max	Mn	P max	S max	Cr	Ni max	Mo max	Cu max
ISO 21988/JN/ HBW555XCr13	555	>1.8 to 3.6	1.0	0.5 to 1.5	0.08	0.08	11.0 to 14.0	2.0	3.0	1.2
ISO 21988/JN/ HBW555XCr16	555	>1.8 to 3.6	1.0	0.5 to 1.5	0.08	0.08	14.0 to 18.0	2.0	3.0	1.2
ISO 21988/JN/ HBW555XCr21	555	>1.8 to 3.6	1.0	0.5 to 1.5	0.08	0.08	18.0 to 23.0	2.0	3.0	1.2
ISO 21988/JN/ HBW555XCr27	555	>1.8 to 3.6	1.0	0.5 to 2.0	0.08	0.08	23.0 to 30.0	2.0	3.0	1.2
ISO 21988/JN/ HBW600XCr35	600	>3.0 to 5.5	1.0	1.0 to 3.0	0.06	0.06	30.0 to 40.0	1.0	1.5	1.2
ISO 21988/JN/ HBW600XCr20 Mo2Cu	600	>2.6 to 2.9	1.0	1.0	0.06	0.06	18.0 to 21.0	1.0	1.4 to 2.0	0.8 to 1.2

Table 1.5: High chromium abrasion-resistant cast irons cross referenced with other international standards.

ISO 21988: 2006 / AS 2027 - 2007	AS 2027 - 2002	EN 12513: 2001	ASTM: 1999	DIN 1695: 1981
ISO 21988/JN/ HBW555XCr13		EN-GJNHV600(XCr11)	12 % Cr	
				G-X 300 CrMo 15 3
ISO 21988/JN/ HBW555XCr16	CrMo 15 3	EN-GJNHV600(XCr14)	15 % Cr-Mo	G-X 300 CrMoNi 15 2 1
ISO 21988/JN/ HBW555XCr21	CrMo 20 1	EN-GJNHV600(XCr18)	20 % Cr-Mo	G-X 260 CrMoNi 20 2 1
ISO 21988/JN/ HBW600XCr20 Mo2Cu	CrMoCu 20 2 1			
ISO 21988/JN/ HBW555XCr27	Cr 27 LC and Cr 27 HC	EN-GJNHV600(XCr23)	25 % Cr	G-X 260 Cr 27
				G-X 260 CrMo 27 1
ISO 21988/JN/ HBW600XCr35	Cr 35			

1.3.2.2 High Chromium White Iron Weld Overlays

High chromium white irons can also be used in the form of welding consumables for the deposition of weld overlays. Chromium white irons welding consumables for build-up and wear resistance constitute the major usage of hardfacing alloys (AS/NZS 2576:2005). The classification as per AS/NZS 2576:2005 for chromium white iron alloys is based on a four digit system specifying the alloy class, alloy type and typical undiluted deposit hardness in Rockwell C (AWRA, 1979). An alphanumeric suffix is also included with the four digits that indicates the deposition technique and type of consumable. Of interest to this review is the 2XXX alloy classification that cover the chromium white irons, Table 1.6.

Table 1.6: AS/NZS 2576: 2005 Table 2.2, Alloys-chemical compositions and microstructure for chromium white irons weld overlays.

Type	Alloy description	Microstructure	Chemical Composition, percent											
			C		Cr		Ni		Mo+Nb+Ti+V+W		B		Fe	
			Min	Max	Min	Max	Min	Max	Min	Max	Min	Max		
21XX	Austenitic iron	Austenite dendrites in a carbide-austenitic eutectic matrix	2.0	2.75	15	27	-	12	-	-	-	-	Rem	
22XX	Martensitic iron	Martensite in a carbide-martensitic eutectic matrix	2	2.75	15	27	-	-	-	-	See Note	2	Rem	
23XX	Austenitic chromium-carbide iron	Chromium-rich primary carbides in a carbide-austenitic eutectic matrix	3.5	7.5	18	35	-	-	-	-	-	-	Rem	
24XX	Complex chromium-carbide iron	Chromium-rich primary carbides in a complex carbide-austenitic eutectic matrix	3.5	7.5	18	35	-	-	5	14	-	-	Rem	
25XX	Martensitic chromium-carbide iron	Chromium-rich primary carbides in a carbide-martensitic eutectic matrix	3.5	5.5	18	35	-	-	-	-	See Note	2	Rem	

NOTE: Minimum B levels is determined by austenite-martensite transformation.

1.3.3 Solidification and Microstructural Development of High Chromium White Irons

1.3.3.1 Solidification Under Slow Cooling Conditions

The solidification under slow cooling conditions refers to the cooling rate that would be expected in large castings. The solidification and microstructural development of high chromium white iron alloys is most easily explained by reference to the iron rich corner of the metastable Fe-Cr-C liquidus surface of the ternary Fe-Cr-C system. A number of Fe-Cr-C liquidus surfaces have been published, with the liquidus surface produced by Jackson (1970) cited extensively. Rivlin (1984) constructed a liquidus projection of the Fe-Cr-C system based on reviewing data from a number of sources. However, there still remained some ambiguity regarding the phase boundaries of the liquidus projection, particularly with regard to the extent of the $M_{23}C_6$ phase field (Thorpe and Chicco, 1985). Thorpe and Chicco (1985) reviewed the liquidus surface produced by Jackson using more accurate experimental techniques and higher purity metals to experimentally determine the iron-rich corner of the metastable Fe-Cr-C liquidus surface shown in Figure 1.2 with an illustrative three dimensional version shown in Figure 1.3. The liquidus surface produced by Jackson (1970) and by Thorpe and Chicco (1985) are the most accepted liquidus surfaces in the literature (Wiengmoon et al., 2005b, Tabrett et al., 1996, Laird II et al., 2000, Dogan et al., 1997). Later work by Chicco and Thorpe (1993) confirmed the positions of points U1 and U2 and the associated transformations shown on the liquidus surface in Figure 1.2.

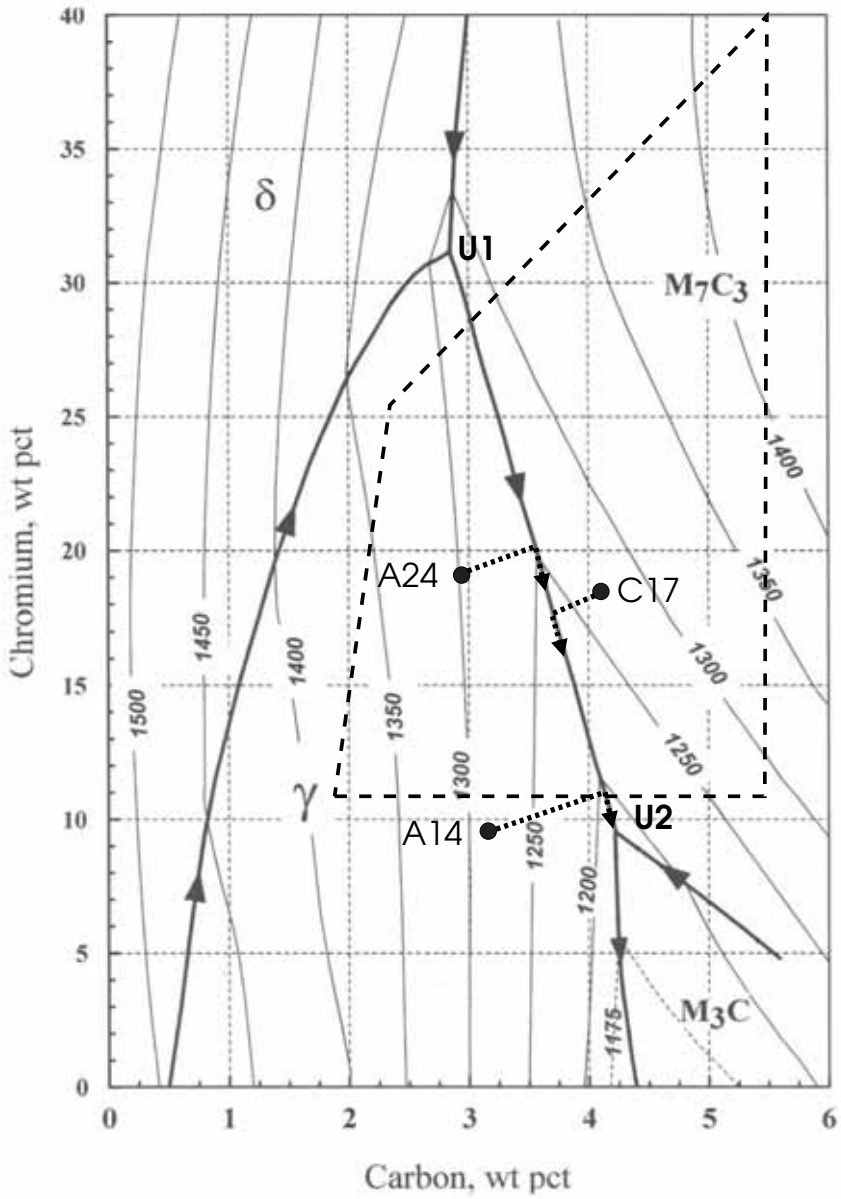

Figure 1.2: The Fe-rich corner of the metastable Fe-Cr-C liquidus surface (after Thorpe and Chicco (1985) adapted from Laird II et al. (2000)). The dashed box indicates typical compositional ranges for high chromium white iron alloys. Points A24, C17 and A14 on the liquidus surface indicate the solidification sequence for alloys having different chemical compositions.

The majority of commercial high chromium white iron compositions fall within the dashed box shown in Figure 1.2 (AS 2027: -2007). Alloys with chemical composition falling within the austenite (γ) phase field solidify as hypoeutectic alloys, alloys with a chemical composition corresponding to the line U1 to U2 solidify as eutectic alloys and alloys with a chemical composition falling within the M_7C_3 field solidify as hypereutectic alloys.

The typical solidification sequence of a hypoeutectic alloy is described with reference to point A24 (2.94 wt% C and 19.0 wt% Cr) on the liquidus surface, Figure 1.2 (Thorpe and Chicco, 1985). Under near equilibrium conditions at point A24, primary austenite is nucle-

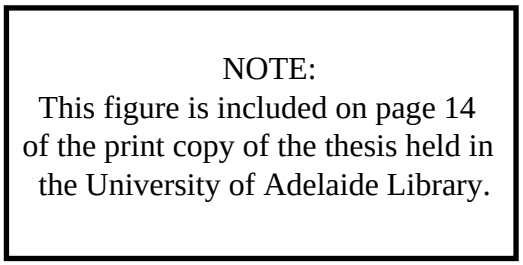

Figure 1.3: Three-dimensional view of the Fe-rich corner of the metastable Fe-Cr-C liquidus surface (Laird II et al., 2000).

ated and will grow as dendrites until reaching the eutectic valley. On reaching the eutectic valley, U1 - U2, the eutectic of austenite and eutectic M_7C_3 (M is Cr, Fe or Fe, Cr) carbides is nucleated and grows along the eutectic valley until solidification is complete at some point before reaching U2.

The eutectic reaction is described by Equation 1.4. In the majority of cases the eutectic reaction is complete before reaching U2. However, alloy compositions that are close to U2 or below about 12% chromium, for example point A14 (3.24 wt% C and 9.55 wt%Cr) can undergo an additional peritectic reaction where the the remaining eutectic liquid can transform to M_3C as given by Equation 1.5 (Thorpe and Chicco, 1985, Pearce, 1984). The M_3C carbide forms as a shell around the eutectic M_7C_3 carbide, in the solid state, and is commonly referred to as a duplex carbide microstructure (Thorpe and Chicco, 1981, Pearce and Elwell, 1986, Randle and Laird II, 1993).

$$liquid \rightarrow \gamma + M_7C_3 \tag{1.4}$$

$$liquid + M_7C_3 \rightarrow M_3C \tag{1.5}$$

The typical solidification sequence of a hypereutectic alloy, point C17 (4.14 wt% C and 18.1 wt%Cr) Figure 1.2, is the nucleation and growth of primary M_7C_3 carbides until the eutectic

valley is reached. On reaching the eutectic valley the normal eutectic transformation of liquid to austenite and M_7C_3 given by Equation 1.4 is initiated and grows until solidification is complete at some point before U2.

The morphology of the primary M_7C_3 carbides that form during solidification have commonly been referred to as needles or being acicular in shape (AS/NZS 2576: 2005). However, based on three-dimensional examination of deep etched samples, the primary M_7C_3 carbides are better described as rods of hexagonal cross section (Powell, 1980, 1979). The carbide rods may also have a hollow core that can extend to the periphery of the carbide. The core contains austenite or one of its transformation products. The morphology of the eutectic M_7C_3 carbides are a scaled down version of the primary M_7C_3 carbides. Depending on the cooling rate, the eutectic M_7C_3 carbides have been found to have a blade like morphology which represents the joining of two or more rods. The blade like carbide morphology is favored by slower growth rates as occurs in slowly cooled castings. Powell (1980) using deep etching techniques and scanning electron microscopy found that the eutectic M_7C_3 carbides formed interconnected (or continuous) grains in three-dimensions. This interconnectivity has also been confirmed by electron back scattered diffraction (Randle and Powell, 1993, Randle and Laird II, 1993, Kootsookos and Gates, 2004).

Upon solidification significant amounts of austenite, both primary and eutectic, can be retained at ambient temperatures (Powell and Bee, 1996). This austenite is metastable as it is supersaturated with carbon and chromium. Austenitic structures are generally favoured by faster cooling rates and high Cr/C ratios although there is always some transformation to martensite in as-cast structures (Pearce, 2002). If the chemical composition of the austenite raises the M_S temperature (martensite start temperature) above ambient, there will be an increased transformation of austenite to martensite on cooling. The increased transformation of austenite to martensite is also favoured if the cooling rate is sufficiently slow to allow the precipitation of secondary carbides within the matrix which raises the $M_S$temperature (Tabrett et al., 1996). The precipitation of secondary carbides lowers the carbon and chromium composition of the austenite.

The segregation of alloying elements within the austenite dendrites of as-cast white irons has been investigated by Dupin et al. (1982), Powell and Laird II (1992) and Powell and Bee (1993) using electron microprobe analysis. Dupin et al. (1982) investigated a 17Cr-2C white iron alloy and found the carbon and chromium content to increase slightly from the core of the dendrite towards the carbide before decreasing adjacent to the carbide/austenite interface, Figure 1.4(a). An increase in the silicon content adjacent to the carbide/austenite interface was also noted. Powell and Laird II (1992) investigated three different alloys ranging in compositions from 9 to 29%Cr and 2.5 to 3.0%C respectively. In all of the alloys investigated, the carbon content was found to be reasonably uniform across the dendrite but the chromium decreased within approximately $2\mu m$ of the eutectic carbide, Figure 1.4(b). Comparison of Figure 1.4(a) and (b) indicates some discrepancies between the results for elemental distri-

bution within the dendrites. However, the results of Dupin et al. (1982), Figure 1.4(a) are plotted on a linear scale and the chromium and carbon measurements vary by approximately 0.5 and 0.3 wt % respectively (Kootsookos, 1995, Hann, 1998). It was also noted by Powell and Bee (1993) that while Dupin et al. (1982) reported a reduction in chromium adjacent to the eutectic carbide, the absolute values for the matrix chromium composition approximated the nominal chromium composition of the sample, which can not be correct for an alloy having a CVF around 30%. However, it is agreed that the distribution of chromium and carbon across the dendrites is reasonably uniform, except for a small region adjacent to the eutectic carbides.

NOTE:
This figure is included on page 16
of the print copy of the thesis held in
the University of Adelaide Library.

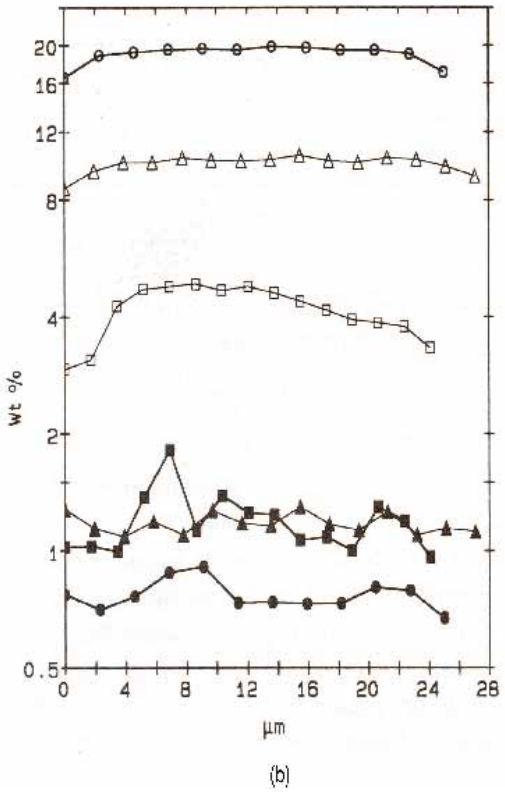

Figure 1.4: Distribution of elements across austenite dendrites of as-cast hypoeutectic high chromium white irons. (a) Chromium, carbon and silicon distributions (Dupin et al., 1982). (b) Chromium (hollow points) and carbon (solid points) distribution for three different high chromium white iron alloys. Note that the ordinate is logarithmic and abscissa is linear (Powell and Laird II, 1992).

Powell and Bee (1993, 1996) found that the depletion of chromium and carbon in the austenite adjacent the eutectic M_7C_3 carbide/austenite interface was responsible for the formation of two thin martensite layers that surrounded the carbide in a 18Cr-3C as-cast white iron. Immediately adjacent to the carbide was an extremely thin layer of high carbon martensite that was surrounded by a thicker layer of low carbon lath martensite adjacent the austenite. Dogan et al. (1995) also confirmed martensite surrounding the eutectic M_7C_3 carbides. Transmission electron microscopy and energy dispersive x-ray spectroscopy analysis of the

thin martensitic region around the carbides and the austenitic matrix away from the carbide found a depletion of chromium in the martensitic region. Carpenter et al. (2004) reported that the region surrounding the eutectic carbides is sufficiently denuded in chromium to allow the formation of martensite in a 27Cr-2.7C alloy. Bedolla-Jacuinde et al. (2005) also reported martensite surrounding eutectic carbides in a 16% Cr white iron.

1.3.3.2 Solidification Under Fast Cooling Conditions

The previous section discussed the solidification of high chromium white irons and microstructural development under slow cooling conditions which are more commonly associated with large castings. However, there are a number of cases where the solidification is much faster, for example, during the solidification of weld overlays or the solidification of a casting adjacent to a chill face. At these faster cooling rates, the microstructure of high chromium white irons has been found to differ from the microstructure that would be expected under slow cooling conditions (Powell, 1990, Powell et al., 1994, Sare, 1979, Powell, 2002).

Faster cooling rates have been found to have a more significant effect on hypereutectic compositions resulting in different microstructures to that expected under slow cooling conditions (Powell, 1990, Powell et al., 1994). The effect of faster cooling rates on hypoeutectic and eutectic compositions is minimal, resulting in a similar microstructure to that obtained under slow cooling conditions, except the eutectic M_7C_3 carbides is finer due to the increased growth rate (Powell, 1990).

Powell (1979), reported that hypereutectic high chromium white iron weld overlays solidifying under fast cooling conditions could form pro-eutectic carbide clusters that had three fold rotational symmetry and did not grow in the direction of thermal gradients. These three fold clusters of carbides were found to be monocrystalline, hence, interconnected and referred to as the complex regular microstructure (Powell, 1990, Randle and Powell, 1993, Powell et al., 1994, Powell and Bee, 2000). The term complex regular eutectic is used to differentiate the undercooled microstructure from the regular non-undercooled microstructure. The complex regular microstructure has also been reported as a refinement to the carbide structure observed at the chill face of hypereutectic castings, Figure 1.5(a) (Sare, 1979). For comparison, Figure 1.5(b) is the same alloy but of a slowly cooled hypereutectic casting showing the large randomly orientated primary M_7C_3 carbides in a eutectic of M_7C_3 and austenite or transformed austenite. The complex regular microstructure consists of a large number (>1000) of rods of hexagonal cross section that have a size between primary and eutectic carbides and form monocrystalline arrays that can be measured millimetres in width. The clusters often consist of a number of intersecting equilateral triangles and in weld overlays, are frequently found adjacent to the steel substrate or between successive weld layers, Figure 1.6. The presence of the complex regular microstructure is due to undercooling which is the

measure of cooling below the liquidus temperature before solidification starts to take place. Undercooling is common in eutectic alloys that have faceted-nonfaceted phases as is the case with the Fe-Cr-C system. The faceted phase is the M_7C_3carbide and the nonfaceted phase is the austenite (Gigliotti Jr et al., 1970, Powell, 1990).

(a)

NOTE:
These figures are included on page 18 of the print copy of the thesis held in the University of Adelaide Library.

(b)

Figure 1.5: (a) Area near the chill face of a 35%CrB alloy, showing what was called *microstructural refinement* produced by rapid cooling, which is now known as the complex regular microstructure, 250x magnification. (b) Area away from chill face (towards the centre of the casting) of the same alloy showing large primary carbides surrounded by carbide-transformed -austenite eutectic, 250x magnification (Sare, 1979).

Figure 1.6: Complex regular microstructure of M_7C_3 carbides in a hypereutectic weld overlay. In this micrograph the carbide rods are aligned at right angles to the plane of the micrograph. Note that these carbide rods form arrays of equilateral triangles (arrowed). Etchant: acid ferric chloride (Powell et al., 2003).

By considering white irons as nonfaceted-faceted eutectic and applying Kofler's theory of coupled growth for a pseudo binary eutectic of austenite and M_7C_3, Powell (2002) explained the wide variation in microstructures developed in hypereutectic high chromium white irons. Variations in microstructure include the complex regular carbide morphology, precipitate free zones around primary carbides or halos and the branched primary carbide morphology. The pseudo binary eutectic for austenite and M_7C_3 is shown in Figure 1.7. In this diagram the liquidus curves have been extended below the eutectic temperature and show a zone of coupled eutectic growth where the austenite and M_7C_3 must grow in unison.

The complex regular microstructure forms when undercooling is approximately 100°C below the eutectic temperature, for example the cooling of composition A from T1 to T2 within the zone of coupled growth, Figure 1.7.

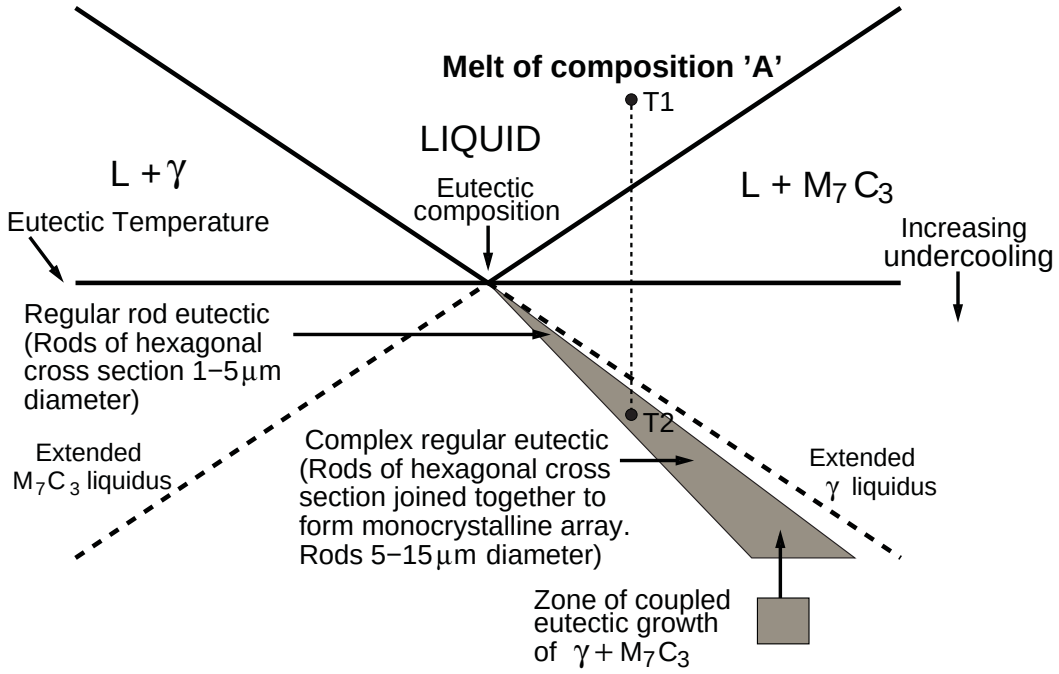

Figure 1.7: Pseudo binary eutectic for austenite (γ) and M_7C_3 showing zone of coupled eutectic growth. The complex regular monocrystalline array occurs when a melt of composition A is undercooled to T2 within the coupled zone (Powell, 2002, Powell et al., 2003).

The formation of precipitate free zones around the primary M_7C_3carbides, Figure 1.8, or halos occurs due to undercooling. The amount of undercooling required for halo formation is less than what is required for the complex regular eutectic, however, depending on the degree of undercooling the halo can be planar, cellular or dendritic. The development of a halo of austenite can be explained by reference to Figure 1.9. Undercooling from temperature T1 to T2 causes primary M_7C_3 to nucleate and the temperature recalesces to T3 due to the release of latent heat from the growth of the M_7C_3 carbides. As the carbides grow, the composition of the liquid follows the M_7C_3liquidus to T4. At T4 the composition of the liquid is to the left of the zone of coupled eutectic growth. The austenite is then nucleated by the primary M_7C_3carbides and grows around the carbide giving the characteristic halo appearance. The composition of the liquid is then moved to T5, the zone of coupled eutectic growth, where the regular eutectic of austenite and M_7C_3carbides is nucleated and grows.

Figure 1.8: Secondary electron micrograph showing halos (grey and arrowed) surrounding primary M_7C_3 carbides in a hypereutectic high chromium white iron weld overlay (Powell et al., 2003).

Figure 1.9: When nucleation of M_7C_3 occurs at T2 in a melt of composition A, the temperature recalesces to T3 with the growth of primary M_7C_3. At T3 the melt follows the M_7C_3 liquidus down to T4 when austenite is nucleated and grows as a halo around primary M_7C_3 (Powell, 2002).

Another variation in microstructure of hypereutectic high chromium white irons as a result of undercooling is the branched primary carbide morphology shown in Figure 1.10. Electron back scatter diffraction has confirmed that all the primary carbides have the M_7C_3 crystal structure, have the same orientation and are therefore interconnected and monocrystalline.

Figure 1.10: Micrograph of branched primary M_7C_3 carbides in a hypereutectic high chromium white iron weld overlay. The carbide rods are almost normal to the plane of the micrograph (Powell et al., 2003).

1.3.4 The Effect of Composition on Microstructure

1.3.4.1 Carbon and Chromium

The microstructure of high chromium white irons depends on the chemical composition of the alloy and the cooling rate (Powell, 1980). The microstructure is generally controlled by two main alloying elements; carbon and chromium. The combination of carbon and chromium affect the carbide volume fraction (CVF), the type of carbides, the composition of the carbides and the composition of the austenite (primary and/or eutectic) (Tabrett et al., 1996, Laird II et al., 2000).

Carbon has the more significant influence on the CVF than chromium. Maratray and Usseglio-Nanot (1970) experimentally determined the relationship (Equation 1.6) between the carbon and chromium compositions and the CVF. Inspection of Equation 1.6 shows that for a 1% increase in carbon, the CVF can increase by 12% but an increase in chromium content of 1% can only increase the CVF by approximately 0.6%. At CVF of greater than 35 to 40%, primary carbides are found in the microstructure and the alloy is hypereutectic (Maratray and Usseglio-Nanot, 1970, Pearce, 1984).

$$CVF = 12.33(\%C) + 0.55(\%Cr) - 15.2 \quad (\pm 2.13 \; standard\,deviation) \tag{1.6}$$

Chromium is a carbide forming element and its proportion is important in determining what type of carbides form in high chromium white irons. Alloys with chromium contents above

approximately 12% generally form eutectic M_7C_3 carbides (Pearce, 2002, Laird II et al., 2000). Below approximately 12% chromium, white irons can form M_3C carbides or a mixture of both M_7C_3 and M_3C carbides. The M_3C carbides have a lower hardness (approximately 1000 HV) than the M_7C_3 carbides and form continuous carbide networks which significantly reduces the toughness of the alloy (Powell, 1980, Pearce, 2002).

The chromium distributes between the carbides and the matrix with a large proportion of the chromium contained within the carbides, substituting for iron in the M_7C_3 carbides. The chromium content of the M_7C_3 carbides has been found to increase regularly with increasing chromium/carbon ratio and approaches a limiting value (Maratray and Usseglio-Nanot, 1970). The maximum chromium to iron ratio of the M_7C_3 carbides was found to be a little lower than $(Cr_5Fe_2)C_3$ (i.e. approximately 70% Cr and 30% Fe) when the chromium to carbon ratio exceeds about 8. Other investigators have reported similar trends for castings of increasing chromium content of the M_7C_3 carbides with increasing chromium to carbon ratio (Powell and Laird II, 1992). Powell and Laird (1992) found that in a 29Cr-2.5C alloy (Cr/C of 11.7) the eutectic M_7C_3 carbides contained approximately 66 wt% chromium, which is in close agreement with the limiting value of $(Cr_5Fe_2)C_3$ proposed by Maratray and Usseglio-Nanot (1970). Dogan and Hawk (1995) also found the chromium content of the eutectic M_7C_3 carbides in a 25Cr-3C casting (Cr/C of 7.9) to be $(Cr_{4.8}Fe_{2.2})C_3$, which also agrees with the previously reported results. The chromium content of the primary M_7C_3 carbides was found to be slightly different from that of the eutectic M_7C_3 carbides when the chromium to carbon ratio was less than about 5.5 for a series of castings (Maratray and Usseglio-Nanot, 1970). Svensson et al. (1986) found the primary M_7C_3 carbides in a Fe-34Cr-4.5C wt% (Cr/C of 7.6) hardfacing to have approximately 4 wt% less chromium than the eutectic M_7C_3 carbides (51.5% compared with 55.8%).

The hardness of the M_7C_3 carbides is reported to gradually increase with increasing chromium contents in an approximately linear fashion (Kagawa et al., 1992). The hardness of the M_7C_3 carbides has also been reported to vary depending on there orientation (Maratray and Usseglio-Nanot, 1970, Dogan and Hawk, 1995). Maratray and Usseglio-Nanot (1970) found that the M_7C_3 carbides are much harder on planes transverse to the axis of the carbide rod than on planes parallel to the axis of the carbide rod. Dogan and Hawk (1995) also found the eutectic M_7C_3 carbides to be harder on the transverse plane rather than on the parallel plane. The hardness values for the M_7C_3 carbides from a selected number of references are given in Table 1.7. It is clear from inspection of Table 1.7 that there is no consistent agreement between the hardness of the M_7C_3 carbides with hardness values significantly different between researchers. It is also common to have standard deviations in excess of $\pm$150 HV or ranges in values over 400 HV (Kagawa et al., 1992, Berns and Fischer, 1997).

Table 1.7: Reported hardness values of M_7C_3carbides.

Type	Approximate Chromium comp. of carbide	Hardness	Reference
eutectic M_7C_3-Transverse	-	1444 $HV_{0.05}$	Maratray and Usseglio-Nanot (1970)
eutectic M_7C_3-Longitudinal	-	950 $HV_{0.05}$	
eutectic M_7C_3-Transverse	$(Cr_{4.8}Fe_{2.2})C_3$	1587 $HV_{0.05}$	Dogan and Hawk (1995)
eutectic M_7C_3-Longitudinal	approx 68 wt %	1346 $HV_{0.05}$	
eutectic M_7C_3	60 wt% 50 wt% 40 wt% 30 wt% 20 wt%	2145 $HV_{0.1}$ 2022 $HV_{0.1}$ 1904 $HV_{0.1}$ 1834 $HV_{0.1}$ 1695 $HV_{0.1}$	Kagawa et al. (1992)
M_7C_3	>13 wt%	1227-1475 HV	Angus (1976)
primary M_7C_3 weld overlays	various	1190-1800 HV	Berns and Fischer (1997)
primary M_7C_3 weld overlays	-	1248-1289 HV	Lee et al. (1996)

A large proportion of the chromium in high chromium white irons is contained within the M_7C_3 carbides. Depending on the ratio of chromium to carbon, insufficient chromium can be left in the matrix and transformation of the austenite to pearlite on solidification can occur. It is also sometimes desirable to have greater than 12% chromium in the matrix for it to have the corrosion resistance properties like stainless steels (Steigerwald, 1974, Powell and Bee, 1993). It is worthwhile to reiterate that in this thesis and in the literature that reference to the matrix in hypoeutectic high chromium white irons includes both the primary austenite and the eutectic austenite or their transformation products (Pearce, 2002). The difference in chromium content between primary austenite and eutectic austenite for hypoeutectic high chromium white irons is seldom made in the literature. However, Carpenter et al. (2004) have found primary austenite contained more chromium than the eutectic austenite by a little less than 2 at% (approximately 1.8wt%). As discussed in Section 1.3.3.1, the chromium is also found to vary throughout the austenite with a region depleted in chromium adjacent the carbides. Thus, the majority of the austenite chromium contents reported in the literature are average values.

Maratray and Usseglio-Nanot (1970) found that the chromium content of the matrix in as-cast chromium-molybdenum alloys could be related to the chromium to carbon ratio by Equation 1.7. The standard deviation in the estimation of the austenite chromium content,

Equation 1.7, was found to be 2.11%Cr.

$$\%Cr_m = 1.95\frac{\%Cr}{\%C} - 2.47 \ (\pm 2.11) \tag{1.7}$$

Other reported chromium and carbon compositions of the austenitic matrix for castings and weld overlays are given in Table 1.8. In this table it can be seen from the work of Powell and Laird II (1992) that as the Cr/C ratio increases, the amount of chromium in the matrix increases and the carbon content decreases. Comparison of the chromium values with those calculated using Equation 1.7, shows that the measured chromium contents fall within the the standard deviation of the experimentally derived equation. The chromium content of the eutectic austenite in a hypereutectic weld overlay was reported by Svensoon et al. (1986) to be about 16%. Comparing this value with the calculated value using Equation 1.7 shows that Equation 1.7 grossly under estimates the chromium composition of the matrix. This could be due to the faster solidification rate, which can have an affect on diffusion and partitioning of alloying elements (Laird II et al., 2000). The average hardness of the austenitic matrix on all of the 42 Chromium-Molybdenum white irons investigated by Maratray and Usseglio-Nanot (1970) was 420±42 $HV_{0.1}$. No significant effect of the chromium/carbon ratio or molybdenum content was found. Laird II and Powell (1993) reported a lower austenitic matrix hardness for a pure 18Cr-3C alloy of 303±15 $HV_{0.1}$.

Table 1.8: Comparison between chromium composition of austenite and the chromium composition calculated using Equation 1.7 for selected references.

Bulk Chemical Composition	Cr/C	Measured Cr (wt%)	Measured C (wt%)	Calcualted Cr equation 13 (wt%)		± standard deviation of 2.11%	Reference
8.8Cr, 3.0C, 5.7Ni hypoeutectic as-cast	2.9	4.7	1.4	3.19	min	1.08	Powell and Laird II (1992)
					max	5.30	
17.7Cr, 3.1C, 1.1Mo hypoeutectic as-cast	5.7	10.1	1.2	8.65	min	6.54	
					max	10.76	
29.3Cr, 2.5C hypoeutectic as-cast	11.7	19.3	0.7	20.35	min	18.24	
					max	22.46	
26.6Cr, 2.72C hypoeutectic as-cast	9.8	18.4 primary*	-	16.64	min	14.53	Carpenter et al. (2004)
		16.6 eutectic*			max	18.75	
34Cr-4.5C hyper. weldoverlay (actual 33.6Cr, 4.46C)	7.5	16.43	0.45	12.16	min	10.05	Svensoon et al. (1986)
					max	14.27	

* The chemical composition of the primary austenite and austenitic matrix was reported as 19.5 ± 0.5 at.% and 17.6 ± 1.4 at.% respectively. The values were converted to wt.% assuming that the other constituent was iron.

1.3.4.2 Alloying Additions Other Than Carbon and Chromium

Alloying additions are included in high chromium white iron alloys to achieve an alloy that can be suitably hardened by subsequent heat treatments, to avoid the formation of undesir-

able phases during casting and to improve mechanical properties. Some of the most common alloying additions in castings are manganese, nickel, molybdenum and copper with typical ranges covered in the relevant standards (see Tables 1.4 and 1.6) (Tabrett et al., 1996). Other metallic alloying elements include strong carbide forming elements such as boron, titanium, vanadium, and tungsten which are added to help improve properties such as hardness. The carbide forming elements, depending on concentration, can form carbides that are much harder than the M_7C_3carbides which can lead to improvements in wear resistance. The hardenability of the matrix is determined by the alloying elements that are contained within the matrix and not by those contained within the carbides (Laird II et al., 2000). Therefore, it is of significance to know how the alloying elements partition between the carbides and the matrix. The effect of alloying element additions on the microstructure and properties of high chromium white iron castings and weld overlays is discussed briefly below.

Manganese

Manganese is a weak carbide forming element and is not strongly rejected by growing austenite dendrites and can substitute for Fe and Cr in the M_7C_3 carbides (Laird II et al., 2000). In low concentrations (less than 1%), manganese partitions approximately equally between the matrix and carbides. Manganese lowers the M_s temperature of the austenite (Tabrett et al., 1996).

Nickel

Nickel has negligible solubility in the M_7C_3 carbides and remains almost entirely within the matrix (Pearce, 2002). Nickel stabilizes the austenite during the cooling after solidification and prevents the formation of pearlite. Nickel has also been found to lower the $M_s$temperature of the austenite (Tabrett et al., 1996). Since nickel almost exclusively segregates to the matrix, it is possible to calculate the expected nickel composition of the matrix by knowing the CVF through Equation 1.8 (Laird II et al., 2000).

$$Ni_{Matrix} = \frac{Ni_{Melt}}{(1 - \frac{CVF}{100})} \tag{1.8}$$

A similar approach can be used for other alloys that are not soluble in the carbide phase such as silicon and copper.

Molybdenum

Molybdenum is a carbide forming element and is soluble in the M_7C_3 carbide but can also form other carbides such as Mo_2C if in concentrations over 2 wt% (Pearce, 2002, Laird II et al., 2000). Mo_2C carbides have a blade-like morphology and a hardness between 1500 to 1800 HV. Molybdenum is primarily used to stabilize the austenite during cooling after solidification and to prevent the formation of pearlite. One of the major advantages of molyb-

denum is that it has little effect on the M_s temperature, compared with other elements that tend to decrease the M_s temperature and over stabilize the austenite (Tabrett et al., 1996). Quantities of molybdenum less than about 1.0% have been found to be insufficient to suppress the formation of pearlite in heavy section castings, while amounts greater than 3.0% have no additional benefit in suppressing pearlite formation (Norman, 1985). Molybdenum, if alloyed in conjunction with nickel, copper and manganese has been found to enhance the pearlite suppressing ability of these elements (Norman, 1985, Tabrett et al., 1996). However, molybdenum is relatively expensive and recent alloy developments have sought to decrease the amount used or replace it altogether.

Copper

Copper has little solubility in the M_7C_3 carbides and remains exclusively in the matrix (Laird II and Powell, 1993, Pearce, 2002). Copper, particularly when used in conjunction with molybdenum, reduces the likelihood of transformation to pearlite on cooling after solidification (Norman, 1985). The use of copper is usually limited to a maximum of about 1.5% due to its limited solubility in austenite.

Silicon

Silicon is not a carbide forming element and is insoluble in the M_7C_3 carbide phase segregating exclusively to the matrix (Laird II and Powell, 1993, Pearce, 1984). It tends to promote the formation of pearlite during cooling in the solid-state (Diesburg and Borik, 1974). Pearce (1984) stated that the silicon content should be kept below 1.2% to minimize pearlite formation. Silicon has been found to segregate within the austenite dendrites and have a higher concentration at the austenite-eutectic carbide interface, Figure 1.4(a) (Dupin et al., 1982). During solid-state cooling from the eutectic liquidus temperature, silicon has been found to lower the carbon and chromium content of the austenitic matrix by promoting the growth of carbides (Laird II and Powell, 1993). The lower carbon and chromium content of the austenite results in an increase in the M_S temperature and a greater transformation to martensite in the as-cast condition (Laird II and Powell, 1993, Powell, 2002). In addition, in hypoeutectic alloys, increased silicon was found to inhibit the nucleation of the M_7C_3 carbides. This did not effect their subsequent growth or the partitioning of carbon and chromium between the carbides and matrix, but resulted in slightly larger eutectic carbides upon solidification.

It has been reported that the addition of silicon to hypereutectic compositions used for weld overlays changes the morphology of the M_7C_3 carbides towards a more equiaxed shape (Atamert and Bhadeshia, 1990). However, this change in carbide morphology was better explained due to undercooling (Powell et al., 1994) (see Section 1.3.3.2). Silicon has been found to promote undercooling in hypereutectic compositions which results in the change in morphology of the M_7C_3 carbides to the complex regular microstructure that can significantly reduce the toughness of hypereutectic alloys.

Boron

Boron is a carbide stabilizer but if present in sufficient quantities can form extremely hard borides (Ma et al., 1990, Angus, 1976). The borides have a higher hardness than M_7C_3 carbides with the M_3B_2 type boride containing 46 to 58% chromium having a hardness between 1600 and 2400 HV (Berns and Fischer, 1997). Boron can substitute for carbon in the M_7C_3 carbides, which increases the hardness of the carbides. Berns and Fischer (1997) found that up to 2.8% boron could substitute for carbon in the M_7C_3 carbides but Petrovic et al. (2005) found boron would only substitute for carbon in M_3C carbides and not in the M_7C_3 carbides. Increasing boron contents up to about 0.6% were found to increase the CVF and increase the size or coarsening of the eutectic carbides in a 13Cr-2.3C alloy (Petrovic et al., 2003, 2005) and in 27% high chromium white irons (Ma et al., 1990). Ma et al. (1990) explained the increase in CVF and carbide coarsening in terms of the activating effect of boron that lowers the surface energy of the carbide which increases the growth rate.

Boron has been found to have a similar effect to silicon in that it reduces the carbon and chromium contents of the austenite and promotes the formation of a martensitic matrix in weld overlays and castings (Powell and Bee, 2000, Petrovic et al., 2003, 2005, Ma et al., 1990). Boron may also promote undercooling, and may favour the development of the undercooled complex regular microstructure in hypereutectic alloys (Powell and Bee, 2000). It is also reported that boron lowers the toughness of 28%Cr alloys with an optimum combination of toughness and wear resistance in alloys containing approximately 0.2% boron (Ma et al., 1990).

Titanium

Titanium is a strong carbide forming element. The titanium carbide (TiC) forms at a temperature above the Fe-Cr-C eutectic temperature. Therefore, in the case of hypoeutectic alloys, the TiC particles appear as small particles within the primary (proeutectic) austenite dendrites (Bedolla-Jacuinde et al., 2005). Due to the TiC consuming carbon, a small decrease in the volume fraction of eutectic M_7C_3 carbides has been found to occur. However, the matrix microhardness is increased due to the presence of hard, small TiC particles. TiC is the most inert and hardest of all the carbides commonly found in white irons and has a hardness value between 2000 to 3100 HV (Laird II et al., 2000). The increase in matrix hardness also increases the bulk hardness of the as-cast alloys (Bedolla-Jacuinde et al., 2005). Titanium is however costly and is very prone to oxidation, and can form small solid TiC particles within the melt, which requires special conditions for alloying when using non controlled atmosphere foundry techniques (Laird II et al., 2000, Bedolla-Jacuinde et al., 2005). Due to titanium's ability to form TiC particles within the melt, it has sometimes been used as an inoculant which can act as a nucleant for austenite and carbide growth.

Niobium

Niobium is also a strong carbide forming element and forms NbC carbides with a hardness value between 1900 and 2400 HV (Berns and Fischer, 1997). Niobium carbide only appears in the pure form. Niobium has negligible solubility in other phases such as austenite and M_7C_3 carbides (Laird II et al., 2000). At concentrations below about 0.6%, NbC will form a thin petal like eutectic cluster within the centre of the austenite dendrites. At concentrations above 1%, primary NbC will from as compact, blocky carbides.

Vanadium

Vanadium is a carbide forming element and is also soluble in the M_7C_3 carbides. It can form its own carbide (e.g. VC) or combine with chromium and molybdenum to form $V_xCr_yMo_zC$ carbides (x>0.5, x+y+z=1) (Laird II et al., 2000, Pearce, 2002). The hardness of vanadium carbides varies according to the composition and can have a hardness value from 2000 to 3000 HV. The morphology of the vanadium carbides is discrete rods that grow from a central nucleation point.

Additions of vanadium up to 4.73% in a 19Cr-2.9C hypoeutectic white iron alloy were found to increase the CVF fraction due to an increase in the proportion of the eutectic M_7C_3 carbides and V_6C_5 carbides as well as increase the amount of transformation to martensite in the as-cast microstructure (Radulovic et al., 1994). The eutectic M_7C_3 carbides were also found to decrease in size with increasing vanadium content. Wiengmoon et al. (2005a) also found a similar trend in that vanadium additions up to 3.7% in a 30Cr-2.3C alloy producing a finer M_7C_3 eutectic carbide structures while also increasing the CVF. The vanadium was found to segregate to the M_7C_3 carbides rather than forming vanadium carbides. The proportion of vanadium in the eutectic M_7C_3 carbides ranged from 7.7 to 14.7 wt% in alloys having a bulk composition of 1.5 to 3.75 wt% vanadium respectively.

1.3.5 Heat Treatment of High Chromium White Irons

High chromium white iron alloys, both castings and weld overlays, solidify with a predominately austenitic matrix which is retained at ambient temperatures. The austenite is metastable as it is supersaturated with carbon and chromium, and possible alloying elements (Laird II et al., 2000). The aim of most heat treatments is to destabilize the metastable austenite so that on subsequent cooling the matrix will transform to martensite (Tabrett et al., 1996). The most commonly used destabilization heat treatment involves holding at a temperature between 800^0C and 1100^0C to allow the precipitation of secondary chromium carbides (Pearce, 1984, Pearce and Elwell, 1986, Powell and Laird II, 1992, Wiengmoon et al., 2005a). Cryogenic treatments have also been used, in conjunction with destabilization heat treatments, to increase the proportion of martensite. High temperature heat treatments have also been investigated as a means to improve the fracture toughness. After destabilization

heat treatments, a temper is done to temper the martensite and to transform as much residual austenite as possible (Wiengmoon et al., 2005a).

This section will discuss the mechanism and effect of destabilization and high temperature heat treatments and the resulting changes in microstructure and properties.

1.3.5.1 Destabilization Heat Treatments

Conventional destabilization heat treatments involve holding at temperature ranges between 800^0C and 1100^0C for times depending on section thickness (Pearce, 1984, Pearce and Elwell, 1986, Powell and Laird II, 1992, Wiengmoon et al., 2005a). Between these temperatures solid state precipitation of secondary carbides occurs with a consequent reduction in the carbon and chromium content of the austenitic matrix. A reduction in carbon and chromium content of the austenite significantly raises the martensite start temperature (M_S) so that on cooling to room temperature the matrix can transform to martensite. This is suggested by Equation 1.9, which has been derived experimentally for a series of alloy steels (Honeycombe and Bhadeshia, 1995). However, Equation 1.9 is not directly applicable to describe the relationship between M_S and alloy content of the austenite in high chromium white irons due to the austenite being supersaturated with carbon and chromium (Powell, 2007). Equation 1.9 is useful in illustrating the qualitative effect carbon, chromium and other alloying elements have on the M_S temperature. The alloying elements commonly added to high chromium white iron to improve hardenability such as Mo, Mn, Ni and Cu, lower the M_S temperature (Laird II et al., 2000).

$$M_S(^OC) = 539 - 423(\%C) - 30.4(\%Mn) - 17.7(\%Ni) - 12.1(\%Cr) - 7.5(\%Mo) \quad (1.9)$$

Depending on the composition of the matrix and the time at temperature, the secondary carbides that precipitate can be M_3C, M_7C_3, $M_{23}C_6$ or a combination (Powell and Laird II, 1992, Powell and Bee, 1996). Powell and Laird (1992) have found that by using the solid state isotherms for the Fe-Cr-C system, it was possible to predict the dominant, equilibrium, secondary carbide, Figure 1.11. This was experimentally confirmed for the alloys investigated by Powell and Laird (1992) given previously in Table 1.8. Examination of the solid state isotherms shows that chromium has a more significant effect than carbon on the type of secondary carbides precipitated.

Figure 1.11: Solid-state isotherms of Fe-Cr-C system at 870^0C (a) and 1000^0C (b) after Rivlin (1984).

In low chromium white irons of less than approximately 10% Cr, the secondary carbides are M_3C (Powell and Laird II, 1992). The M_3C carbides heterogeneously nucleate within the austenite as growth does not occur on the eutectic carbides. As the time at temperature

increases, the number of secondary M_3C carbides increases without a change in morphology. The morphology of the secondary M_3C carbides is plate-like, Figure 1.12(a).

The secondary carbides in 15 to 20% Cr hypoeutectic high chromium white irons have been confirmed to be M_7C_3 (Pearce, 1983, 1984, Powell and Laird II, 1992, Tabrett et al., 1996, Wiengmoon et al., 2005a). However, Powell and Bee (1996) found that in 18Cr-3.1C-1.1Mo alloy having an austenitic matrix composition of 10.1Cr-1.2C-0.4Mo, that after a short duration at a destabilization temperature of 1000^0C, extensive $M_{23}C_6$ secondary carbides had heterogeneously nucleated within the austenite and not the expected M_7C_3 carbide. Sub-grain boundaries, formed in the as-cast state due to the difference in the coefficient of thermal contraction of carbides and austenite matrix, have been found to be preferential nucleation sites for the initial precipitation of secondary carbides (Bee et al., 1994). The secondary $M_{23}C_6$ carbides have the appearance of discrete cubes in two-dimensions and their cuboidal shape was confirmed when deep etched and examined in an electron microscope, Figure 1.13 (Powell and Laird II, 1992). The preferential formation of $M_{23}C_6$ rather than the equilibrium M_7C_3 carbide was explained in terms of the reduced activation energy required for nucleation due to the good lattice matching between austenite and $M_{23}C_6$ carbides. After a longer destabilization time of 4 hours, further precipitation and growth of the secondary carbides occurs, and the equilibrium M_7C_3 carbide, having the morphology of discrete rods of hexagonal cross section or plate-like shapes, had also precipitated, Figure 1.12(b). It would appear that due to the kinetics of nucleation and growth, it is possible to have a destabilized microstructure consisting of the non-equilibrium carbide ($M_{23}C_6$) and equilibrium carbide (M_7C_3).

In high chromium white iron alloys of 25-30%Cr, the secondary carbides that precipitate within the austenite have been confirmed to be $M_{23}C_6$ (Pearce, 1983, Powell and Laird II, 1992, Tabrett et al., 1996, Wiengmoon et al., 2005a). The $M_{23}C_6$ secondary carbides have the appearance of fine fibers and are rod-like in shape and tend to join together to form an interconnected network, Figure 1.12(c) (Powell and Laird II, 1992, Wiengmoon et al., 2005a). Higher destabilization temperatures result in coarser secondary carbide particles and a greater tendency for a network of carbides to form (Wiengmoon et al., 2005a, 2004).

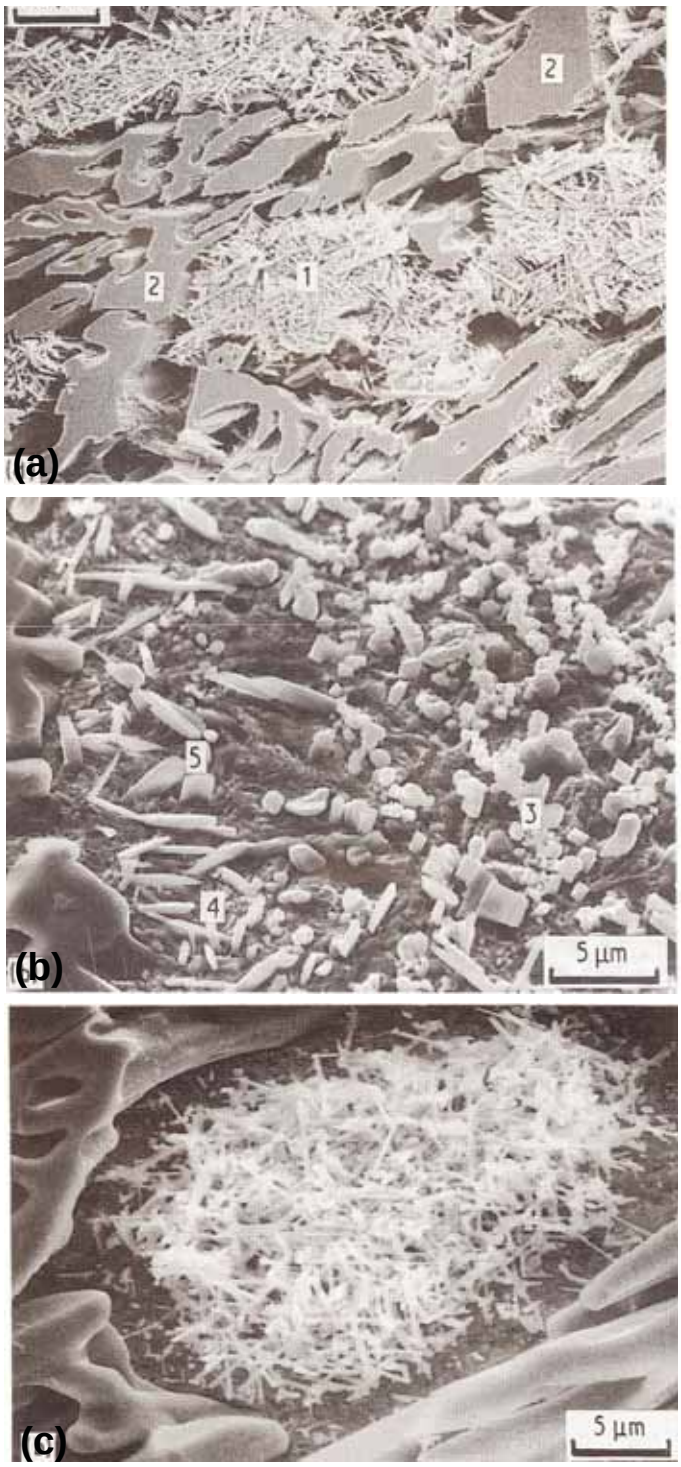

Figure 1.12: Scanning electron micrographs of heat treated high chromium white iron castings after deep etching (a) A 9Cr-3C alloy destabilized at 800^0C for 4 hours. Secondary M_3C carbides (marked 1) have precipitated within the prior austenite. The larger carbides are the eutectic M_7C_3 carbides (marked 2). (b) A 18Cr-3.1C-1.1Mo alloy destabilized at 1000^0C for 4 hours. Secondary M_7C_3 carbides (marked 4 and 5) have precipitated within the prior austenite. The secondary M_7C_3carbides marked 4 are discrete rods and carbides marked 5 are plate-like in shape. (c) A 29Cr-2.5C alloy destabilized at 1000^0C for 4 hours. Secondary $M_{23}C_6$ carbides have precipitated within the prior austenite. The secondary $M_{23}C_6$ carbides are very fine fibers (fibrous) which appear to be connected (Powell and Laird II, 1992).

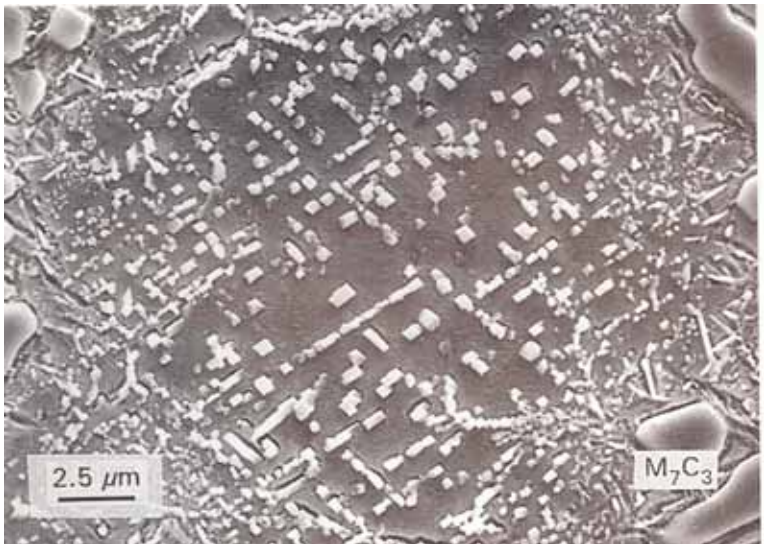

Figure 1.13: Scanning electron micrographs of heat treated high chromium white iron castings. Sample is a 18Cr-3.1C-1.1Mo alloy destabilized at 1000^0C for 0.25 hours (same alloy as Figure 1.12(b)). The secondary $M_{23}C_6$ carbides have a cubic faceted morphology (Powell and Bee, 1996).

During the conventional destabilization heat treatments of 10-25% high chromium white irons, the eutectic M_7C_3 carbides remain unaffected and no change in morphology occurs (Pearce and Elwell, 1986, Powell and Laird II, 1992, Wiengmoon et al., 2005a). The secondary carbides form heterogeneously within the austenitic matrix and do not nucleate and grow on the eutectic carbides. Powell and Laird II (1992) found that the destabilization of a 29Cr-2.5C white iron gave secondary $M_{23}C_6$ carbides that had heterogeneously precipitated within the austenite and there was no transformation of the eutectic M_7C_3 carbides.

In a 30Cr-2.4C alloy, Pearce and Elwell (1986) found that the eutectic M_7C_3 carbides would undergo an in-situ transformation to $M_{23}C_6$ during normal destabilization heat treatments. In the heat treated condition, the eutectic M_7C_3 rods were surrounded by a complete or partial shell of $M_{23}C_6$, forming a duplex carbide. It is believed that the $M_{23}C_6$ carbides nucleate at the original interface between the eutectic M_7C_3 and the matrix before growing inwards, consuming the M_7C_3 carbide. $M_{23}C_6$ carbides were also found to precipitate within the prior dendritic austenite matrix as well as forming the duplex carbides. Wiengmoon et al. (2005a) also confirmed the transformation of eutectic M_7C_3 to $M_{23}C_6$ in a 30Cr-2.3C white iron with and without additions of vanadium.

There exists an optimum destabilization temperature to provide maximum hardness for white iron alloys (Maratray and Poulalion, 1982, Sare and Arnold, 1995, Tabrett et al., 1996). The maximum hardness has been found to depend on the ratio of martensite to retained austenite, Figure 1.14 (Maratray and Poulalion, 1982). At higher than optimum destabilization temperatures, the hardness decreases due to an increase in the amount of retained austenite and the secondary carbides are fewer and coarser (Sare and Arnold, 1995, Tabrett and Sare, 1998). The increase in retained austenite is due to the increase in the solid solubility of carbon in

austenite with increasing temperature (Figure 1.11) which decreases the driving force for secondary carbide precipitation and therefore the lowering of carbon and chromium within the austenite. The higher carbon and chromium content of the destabilized austenitic matrix results in a lowering of the M_S temperature, Equation 1.9, which decreases the amount of transformation to martensite. However, the martensite that has transformed is of a higher carbon content and therefore of a higher hardness. At lower than optimum destabilization temperatures, secondary carbide precipitation is usually extensive, causing a significant reduction of carbon within the austenite. On cooling, near complete transformation to martensite occurs, but the carbon content of the martensite is low and therefore has a lower hardness (Tabrett et al., 1996).

Figure 1.14: Influence of destabilization temperature on hardness and retained austenite content (Maratray and Poulalion, 1982).

1.3.5.2 High Temperature Heat Treatments

High temperature heat treatments at temperatures between 1160 to 1190^{o}C followed by air cooling results in the dissolution of secondary carbides to form a homogenized austenitic matrix microstructures generally free of secondary carbides (Skoblo et al., 1991, Tabrett et al., 1996). At the higher temperatures, the carbon and chromium solubility in the austenite is increased, which is evident in the solid state isotherms shown in Figure 1.11, and the driving force for carbide precipitation is reduced (Tabrett et al., 1996, Hann and Gates, 1997). The

higher carbon content of the matrix results in a substantial lowering of the M_S temperature producing high retained austenite levels in air cooled structures. It has been reported that regardless of how high the heat treatment temperature used, that there is always less carbon in the matrix after heat treatment than in the as-cast condition (Hann and Gates, 1997).

High temperature heat treatments above 1100^{o}C have been investigated to improve the fracture toughness of hypoeutectic high chromium white irons by changing the carbide morphology (Pearce, 2002, Kootsookos et al., 1995). It has been reported that these high temperature heat treatments can reduce the continuity and angularity of the original eutectic carbides and produce a limited amount of coarse secondary carbides in an otherwise stabilized austenitic matrix which improves the fracture toughness (Pearce, 2002). However, with the exception of the alloy compositions that form the duplex carbide morphology previously discussed in section 1.3.5.1, the morphology of the eutectic M_7C_3 carbides cannot be altered by high temperature heat treatments irrespective of how high the heat treatment temperature (Skoblo et al., 1991, Kootsookos, 1995, Hann, 1998). High temperature heat treatments have been found to give improvements in fracture toughness in certain alloys, but as a result of improved matrix characteristics and the formation of strain induced martensite (Kootsookos et al., 1995, Hann and Gates, 1997, Hann et al., 1997). It is also believed that the high temperature re-austenisation heat treatments improve toughness by removing the transformed matrix band that often surrounds the eutectic carbides, improving carbide-matrix cohesion (Tabrett et al., 1996).

1.4 Corrosion

1.4.1 Introduction

Corrosion is the chemical or electrochemical reaction between a material, usually a metal, and its environment that produces a deterioration of the material and its properties (ASTM G15-99). Corrosion being electrochemical in nature, involves the transfer of electrons during the chemical reaction (Thompson and Payer, 1998, Jones, 1992). During corrosion simultaneous oxidation and reduction reactions occur on the metals surface. The oxidation reaction results in the generation of electrons at anodic areas of the corroding metal resulting in metal dissolution. The reduction reaction consumes electrons at cathodic areas of the metal and frequently results in the discharge of hydrogen ions or the reduction of oxygen. In all cases, the rate of the oxidation (anodic reaction) is equal to the rate of reduction (cathodic reaction) as no current accumulates on the metal surface.

There are many different forms of corrosion that are categorized by the appearance of the corroded metal (Fontana, 1986). The forms of corrosion, commonly referred to as the eight forms of corrosion, are: uniform attack, galvanic corrosion, crevice corrosion, pitting, in-

tergranular corrosion, selective leaching, erosion-corrosion and stress corrosion. The significant forms of corrosion in the alumina processing plant environments are uniform attack, galvanic corrosion, pitting corrosion and stress corrosion (May and Orchard, 1988).

Uniform attack is the most common form of corrosion (Fontana, 1986, Jones, 1992). It involves a uniform electrochemical reaction over the entire exposed surface that results in the gradual thinning of the material being corroded.

Galvanic corrosion is a form of electrochemical corrosion associated with dissimilar metals in electrical contact. When two metals are in electrical contact, there usually exists a potential difference between them that induces a flow of electrons from the anode (less corrosion resistant or more active metal) to the cathode (the more corrosion resistant or noble metal). The cathode will corrode very little, if at all and the anode will preferentially corrode at a faster rate than if the materials were not in electrical contact. Galvanic corrosion can also occur between different microstructural phases in a material.

Pitting corrosion is an extremely localized form of attack that can results in holes in the metal. A pit is a cavity or hole with the surface diameter being about the same or less than that of the depth.

Stress corrosion or stress corrosion cracking (SCC) is a form of corrosion that results in the cracking of a metal due to the combined action of a tensile stress and corrosive environment.

Corrosion is usually studied using thermodynamic and kinetic principles. Thermodynamics gives an understanding of the energy changes involved in the electrochemical reactions and the available driving force to control the spontaneous direction of the electrochemical reaction (Jones, 1992). Thermodynamic principles are useful in determining conditions where corrosion is thermodynamically impossible. However, corrosion is thermodynamically possible for most environmental conditions and it is of significant importance to know how fast corrosion will occur. Chemical kinetics is a study of the rates of electrochemical reactions and can provide quantitative information to estimate the rate of material deterioration.

The controlling parameters of a corrosion reaction are potential (volts), current (amperes) and resistance (ohms) (Thompson and Payer, 1998). The potential provides a value for the driving force for the corrosion reaction to proceed, and the current provides a measure of the rate at which the reaction proceeds. The magnitude of the corrosion current that flows for a given potential is determined by the resistance elements throughout the cell (greater resistance results in less current flow). Controlling or measuring either the current or the potential enables the corrosion reaction to be studied and quantified. A device often used for these measurements is a potentiostat.

Under equilibrium conditions a corroding metal will reach a steady state potential which is specific for a particular metal and aqueous solution environment, referred to as the rest potential or corrosion potential (Ecorr). The rest potential depends on the anode and cathode reactions, which determines the rate that electrons can be exchanged (Jones, 1992). The rest

potential of a corroding metal can be altered by altering the rate of electron flow, such as making electrons available to the metal via an external source which will cause the potential to shift in the negative direction. This process is referred to as polarization and a shift in potential in the negative direction is cathodic polarization and a shift is the positive direction is anodic polarization.

Anodic polarization generally results in the enhanced dissolution (corrosion) of the metal as a greater driving force for corrosion to occur is created as the anodic potential increases. However, above a critical anodic potential, the corrosion rate can significantly decrease due to the formation of a thin, protective corrosion-product surface film that acts as a barrier to the anodic dissolution reaction. This reduction in corrosion rate, even at highly anodic potentials, is referred to as passivity. Some common examples of metals that exhibit passivity are iron, chromium, nickel, titanium and cobalt.

1.4.2 Potential-pH (Pourbaix) Diagram

The potential-pH diagrams, commonly referred to as Pourbaix diagrams, are maps of possible phases that are thermodynamically stable in an aqueous electrochemical system (Jones, 1992, Beverskog and Puigdomenech, 1996, Pourbaix, 1966). These diagrams are useful for studying the corrosion behaviour of many metallic materials, including alloys.

Three areas are readily identified on the potential-pH diagrams, these being immunity, passivation and corrosion. These are shown in Figure 1.15 for iron at 25°C and atmospheric pressure. The area designated immunity indicates corrosion is thermodynamically impossible under the conditions of potential and pH and represents the stability of the metal itself. The area designated passivation refers to the development of a corrosion product that covers the surface and can significantly reduce the rate of corrosion. For iron this layer could be hydrated magnetite (Fe_3O_4) or haematite (Fe_2O_3). The area designated corrosion refers to the dissolution of the material into a soluble ion form via electrochemical means, for example, at high pH values as dihypoferrite ions ($HFeO_2^-$).

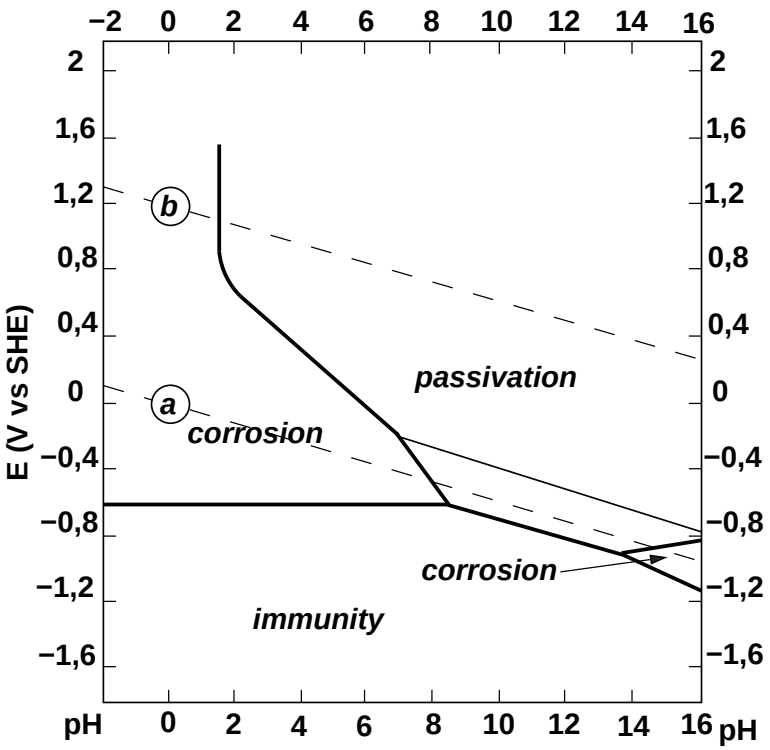

Figure 1.15: Potential-pH diagram for iron at 25°C and atmospheric pressure showing the regions of immunity, corrosion and passivation (Pourbaix, 1966).

For conditions where corrosion is possible no prediction can be made as to the corrosion rates, that is the kinetics of the reaction can not be determined. However, increasing temperatures usually results in faster reaction rates and diagrams based on thermodynamic considerations become more relevant at predicting the actual corrosion mechanism (Beverskog and Puigdomenech, 1996). The original work by Pourbaix (1966) presented potential-pH diagrams for a range of metallic materials at 25°C and at atmospheric pressure. For some of the more common metallic elements such as Fe, Cr, Ni, more recent work has seen the potential-pH diagrams revised for higher temperature environments up to 300°C (Townsend Jr, 1970, Beverskog and Puigdomenech, 1996, 1997).

The change in the potential-pH diagrams for iron and chromium at temperatures from 25 to 100°C are shown in Figures 1.16 and 1.17 respectively. For iron, the most notable change is the large increase in area of stability of the dissolved $HFeO_2^-$ ion species at alkaline pH values and the corresponding decrease of the stability of species in adjacent fields (Townsend Jr, 1970, Beverskog and Puigdomenech, 1996). Similarly the potential-pH diagrams for chromium with increasing temperature show changes in the size of the different areas of immunity, passivation and corrosion, Figure 1.17. The corrosion area for chromium at alkaline pH values increases due to the increased stability of the chromite ions ($Cr(OH)_4^-$) (Note: the ?? mark after the $Cr(OH)_4^-$ ion in Figure 1.17 was included as the exact stoichiometry of the chromite ion is unknown).

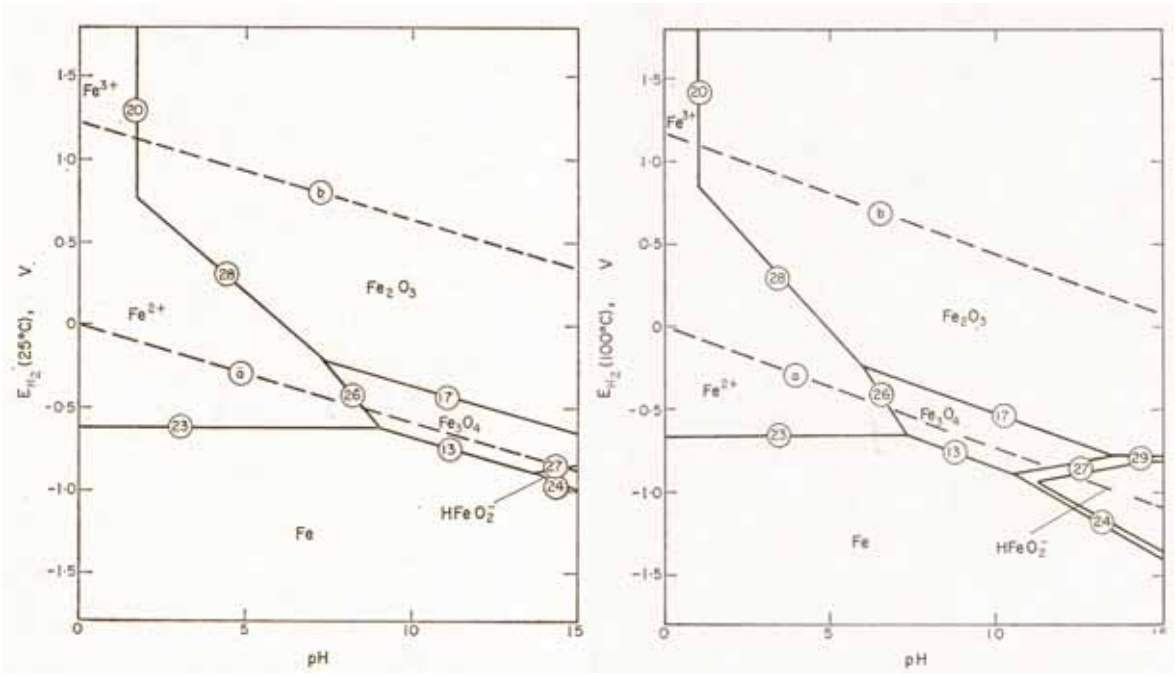

Figure 1.16: Potential-pH diagrams for iron at 25°C and 100°C (Townsend Jr, 1970).

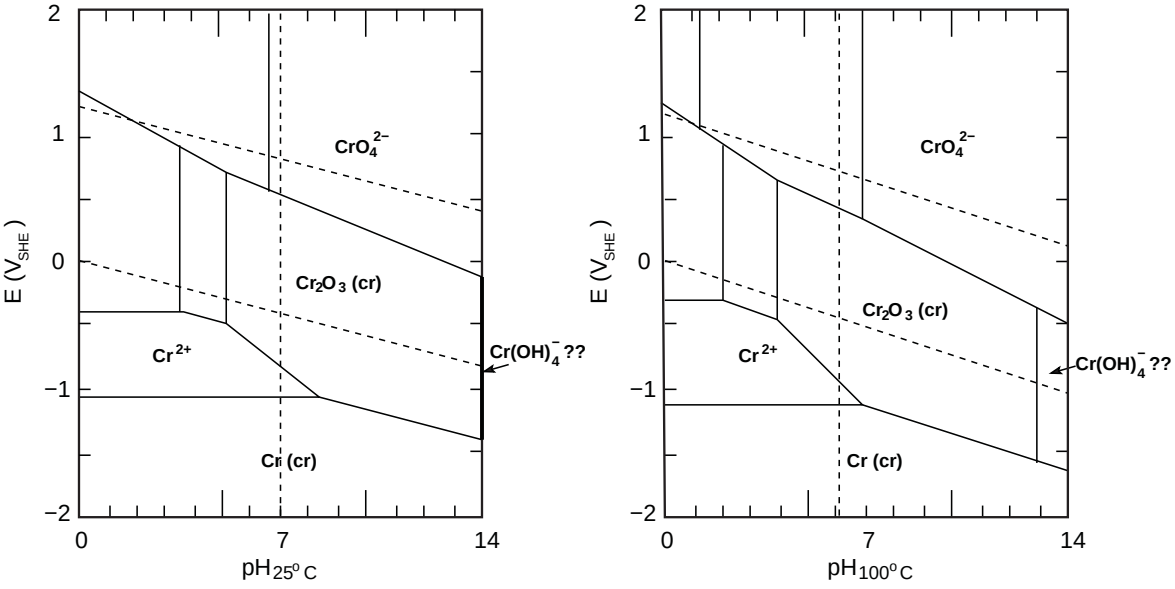

Figure 1.17: Potential-pH diagrams for chromium at 25°C and 100°C. Activities of dissolved substances taken as 10^{-6}m. Pressure taken as 1 atm. (Beverskog and Puigdomenech, 1997).

It should be noted that the potential-pH diagrams are based on model environments free from contaminants, such as chloride and sulphate ions, which can adversely effect the corrosion behaviour of the material (Pourbaix, 1966, Meulendyke et al., 1987). It has also been discussed by Beverskog and Puigdomenech (1997) that due to the lack of thermodynamic data, in particular for chromium, that the potential-pH diagrams are based on the limited available data. Nevertheless, potential-pH diagrams can be used to identify potential and pH values

where metals and alloys are susceptible to corrosion, passivation or immunity and the likely chemical products.

1.4.3 Corrosion of High Chromium White Irons

1.4.3.1 Introduction

Only a limited number of corrosion studies on high chromium white irons have been reported in the literature. The majority of the corrosion studies have investigated the corrosion of cast alloys in a wide variety of environments. Only a few of these studies have investigated the corrosion of high chromium white ions in highly alkaline environments similar to those found in the alumina processing industry. Table 1.9 summarizes the corrosion studies, which used highly alkaline pH environments and and Table 1.10 summaries the corrosion studies for a range of pH values from strongly acidic to slightly alkaline. Comparing the number of investigations in Table 1.9 and 1.10 it can be seen that the corrosion studies in highly alkaline environments are very limited.

Table 1.9: Summary of corrosion investigations on high chromium white irons in highly alkaline environments.

Author	Solution	pH	Alloy
Arnold et al. (1998)	Alumina plant environment	14	Investigation of worn hypereutectic weld overlay plant components
Tu et al. (2006)	303 g/L NaOH Temp 85^{o}C	14	1.9C, 13.6Cr and 3.0C, 26.7Cr
Tu et al. (2004)	Slurry, 25% caustic, 34.3% alumyte Temps up to 100^{o}C	Alkaline	1.9C, 13.6Cr and 1.7C, 12.3Cr, 1.3Ni, 1.4Mo and 3.0C, 26.7Cr

Table 1.10: Summary of corrosion investigations on high chromium white irons in a range of corrosive environments from highly acidic to alkaline.

Author	Solution	pH	Alloy
Naiheng et al. (1989)	Acidic H_2SO_4 Alkaline NaOH Temp ambient	1, 3, 7, 10	2.3C, 27Cr, 2Cu, 0-0.6B and 2.9C, 28Cr, 2Cu and 3.2C, 13.8Cr, 1.3Cu
Pitt and Chang (1986)	Slurry	5.5, 6.5, 7.5, 8.5, 9.5, 10.5	3.4C, 18Cr
Neville et al. (2006)	1000ppm NaCl, NaOH	8.5	2.5C, 26Cr and 3.0C, 28Cr, 1.8Mo and 4.3C, 40Cr
Lu et al. (2006)	Recycled cooling water Temp 22-60^{o}C	8.05	2.0-3.9C, 10-39Cr, 0.2-2.5Mo, 0.5-6.4Ni
Watson et al. (1995)	1N Na_2SO_4	6.8	2.7C, 13.5Cr
Zumelzu et al. (2002, 2003)	Sugar juice	5.2	0.5-1.5C, 14-35Cr, 0.2-8.2Ni, 0-2.2Cu
Zhang et al. (2004)	5% H_2SO_4 Temp 20^{o}C	1.5	2.5C, 14Cr and 2.6C, 23Cr
Kumar and Patwardhan (1993)	5% NaCl		3.1C, 6.0Cr, 6.0Mn, 1.0Cu

1.4.3.2 Corrosion of Castings

The corrosion of high chromium white iron castings for all pH environments occurs by the preferential corrosion of the matrix while the carbides remain inert and therefore the corrosion of high chromium white iron castings is dominated by the matrix phase (Neville et al., 2006, Meulendyke et al., 1987, Ma et al., 1990, Zhang et al., 2004, Day, 1982). Generally the corrosion of the matrix occurs preferentially at the carbide-matrix interface and is commonly referred to as inter-phase corrosion. Interface corrosion results in the corrosion surface having the appearance of pitting corrosion.

The multiphase nature of high chromium white irons, consisting of intermetallic carbides and a ferrous based matrix, can lead to galvanic corrosion between the two phases (Day, 1982, Neville et al., 2006, Zhang et al., 2004, Ma et al., 1990, Watson et al., 1995). The carbides form the cathode and remain inert and the matrix forms the anode and preferentially corrodes in aqueous electrolytes. The potential difference between the carbides and the matrix in a pH 1.5 H_2SO_4 solution has been found by Zhang et al. (2004) to vary between about 70 and 50 mV for hypoeutectic heat treated high chromium white irons. This was believed to be the main reason for the corrosion of the matrix and inter-phase corrosion. Ma et al. (1990) also believed that the inter-phase corrosion of the matrix was due to galvanic interaction with the carbides and was further influenced by the spacing of the carbides. The galvanic current

density was thought to be highest in the region of the matrix immediately surrounding the carbide. A smaller inter-carbide spacing intensified the galvanic current between the carbides and matrix accelerating the galvanic corrosion of the matrix.

Due to the galvanic interaction between the carbides and matrix, a higher CVF is expected to increase the galvanic interaction and increase the overall corrosion rate (Kumar and Patwardhan, 1993, Tu et al., 2004). The presence of secondary carbides within the matrix of destabilized heat treated high chromium white irons is also likely to increase corrosion of the matrix (Ma et al., 1990, Pearce, 2002). However, Neville et al. (2006) found CVF is not a good indicator of corrosion performance as a hypereutectic alloy having a carbide volume fraction of 51% had superior corrosion performance to alloys having a CVF of 30 and 39%.

The matrix chromium content of high chromium white irons is believed to have a significant influence on corrosion behaviour. Several authors suggested that corrosion resistance, in all environments, improves with increasing matrix chromium composition above approximately 12% (Steigerwald, 1974, Arnold et al., 1998, Svensson et al., 1986, Dupin et al., 1982, Sailors and Owens, 1982, Lu et al., 2006, Rajagopal and Iwasaki, 1992). The improvement in matrix corrosion performance is due to the formation of a continuous, adherent and self-regenerating Cr_2O_3 oxide film similar to that formed on stainless steel materials. For ambient temperature oxidizing environments, a minimum of 12% chromium, in solid solution, is necessary to produce a stainless iron matrix in high chromium white irons. If the matrix chromium content is less than approximately 12%, the corrosion behaviour in aqueous environments will be similar to that of iron (Steigerwald, 1974). Further increasing matrix chromium composition above 12% is believed to be beneficial in enhancing the ability of the matrix to passivate, maintain its passivity over a broader range of operating conditions, improve resistance to pitting and improve resistance to higher temperature corrosion (Steigerwald, 1974, Meulendyke et al., 1987, Svensson et al., 1986). Increases in matrix chromium content can be achieved by increasing the bulk chromium content while holding the carbon content constant, or by reducing the carbon content (AS 2027: 2007).

Hypereutectic high chromium white iron alloys having a high CVF are generally found to have inferior corrosion performance compared with the lower CVF alloys (Llewellyn et al., 2002, Llewellyn and Dolman, 2004). This is due to the increased carbon contents required to achieve hypereutectic microstructures. The carbon combines with chromium to form carbides which depletes the matrix of chromium. In practice, to improve the corrosion performance of high chromium white irons, lower carbon (1.5% min) and high chromium bearing alloys having a low CVF and a ferritic and austenitic matrix have been used (Llewellyn et al., 2002, Llewellyn and Dolman, 2004, Pearce, 2002). However, more recent work has found that it is possible to have a CVF above 40% and still maintain greater than 18% chromium in the matrix and comparable corrosion performance to lower carbon and CVF alloys (Llewellyn and Dolman, 2004, Neville et al., 2006).

The corrosion investigation by Neville et al. (2006) found that the corrosion performance

of a hypereutectic alloy in a pH 8.5 solution having a CVF of 51% and a matrix chromium composition of 18.8% had superior corrosion performance to alloys having lower CVF of 30 and 39% and matrix chromium compositions of 15.1 and 13.3% respectively. Likewise, Llewellyn and Dolman (2004) claimed that a hypereutectic alloy having a CVF of 40% and matrix chromium composition of about 19% had similar corrosion resistance to a hypoeutectic alloy having a CVF of 25% and matrix chromium composition of 19%. Unfortunately, specific corrosion environments or corrosion analysis methods were not reported. These results would indicate that matrix chromium compositions have more of an influence on corrosion performance than the unfavourable effects due to increased galvanic activity between the carbides and matrix for high CVF alloys.

Tu et al. (2006) reported the corrosion in static concentrated caustic of a 3C, 27Cr alloy with a matrix chromium composition of about 16% was greater than a 1.9C, 14Cr alloy with a matrix chromium composition of approximately 12%. They suggested that the increasing matrix chromium composition resulted in the increased dissolution of the matrix in the concentrated caustic environment for the 3C, 27Cr alloy.

Alloy segregation, particularly chromium, within the matrix has also been proposed as a reason for the preferential corrosion surrounding the carbides, or inter-phase corrosion, commonly found with high chromium white iron alloys (Powell and Bee, 1993, Neville et al., 2006, Pearce, 2002). The chromium content of the matrix adjacent to the carbide-matrix interface is lower in chromium than the bulk of the matrix. The mechanism by which this occurs is discussed in detail in Section 1.3.3.1. The lower matrix chromium content at the carbide-matrix interface and/or galvanic interaction between the matrix and carbides is the primary mechanism for inter-phase corrosion (Meulendyke et al., 1987, Zhang et al., 2004, Ma et al., 1990). Powell and Bee (1993) found that the chromium depleted matrix adjacent to the eutectic carbides would result in a transformed layer of martensite surrounding the eutectic carbides. This location of the low chromium martensite surrounding the carbides was consistent with the pitting corrosion in wet grinding applications.

The addition of nickel to high chromium white irons has been found to enhance the corrosion resistance of the alloys (Neville et al., 2006, Zumelzu et al., 2002, 2003). The nickel, which segregates almost exclusively to the matrix, has been found to improve the corrosion performance in acidic pH sugar juice media (Zumelzu et al., 2002, 2003) and in slightly alkaline pH 8.5 cooling water (Neville et al., 2006). It is believed that the nickel participates in the protection mechanism and therefore the corrosion behaviour does not exclusively depend on the chromium composition.

1.4.3.3 Corrosion of High Chromium White Iron Weld Overlays

The information reported in the literature on the corrosion of high chromium white iron weld overlays, in any corrosive environment, is extremely limited. Arnold et al. (1998)

investigated worn hypereutectic high chromium white iron weld overlays used in alumina processing plants. The investigation found that the matrix of the weld overlays was severely corroded. The matrix of the hypereutectic high chromium white iron weld deposits (AS/NZS 2576: 2005 - 25XX type) was found to contain approximately 7% chromium. The matrix content being lower than 12% chromium was believed to result in the preferential dissolution of the matrix, which removed the support for the M_7C_3 carbides.

Hypereutectic high chromium white iron weld overlays contain check cracks due to the brittle nature of the alloy and the deposition process (Arnold et al., 1998). The check cracks have been found to act as an access path for corrosive liquid to attack the interface between the weld overlay and steel substrate.

1.5 Erosive Wear

1.5.1 Introduction

Erosive wear is the progressive loss of original material from a solid surface due to mechanical interaction between the surface and a fluid, a multicomponent fluid, or impinging liquid or solid (ASTM G40-98b, 1999). Erosive wear is more specifically classified as cavitation erosion, liquid impingement erosion, or solid particle erosion. Of particular interest to this work is solid particle erosion, which is the wear of a solid surface due to solid particle impingement contained within a moving fluid. Solid particle erosion is often likened to low-stress, or scratching abrasion which occurs when lightly loaded abrasive particles move across a wear surface without particle fracture. The distinguishing difference between erosion and low-stress abrasion is that the erosive process involves impingement at a reasonably high velocity and the contact stress is applied as a result of kinetic energy transferred from the particle to the wear surface (Rabinowicz, 1965, Sarkar, 1980). Erosive wear is further categorized into impingement-erosion and abrasion-erosion, Figure 1.18. Impingement-erosion or impact erosion occurs if the particles impinge the surface at approximately normal angles. Abrasion-erosion is commonly used to describe solid particle erosion in which the particles move nearly parallel to the solid surface and is commonly associated with the wear environment in slurry pumps, cyclone classifiers and the hydraulic transfer of slurries (MTIA, 1986, Llewellyn and Dolman, 2004). The wear mechanisms for erosion and low-stress abrasion are similar and the wear characteristics produced by erosive wear are analogous to those produced by low-stress abrasive wear (Rabinowicz, 1965). Erosion is associated with the progressive thinning of components. The appearance of eroded wear surfaces includes a macroscopic scooping appearance following the particle flow direction, surface roughening ranging from polishing to severe roughening, depending on particle size and velocity, lack of directional grooving characteristic of abrasion and in some cases the formation of ripple patterns on metals.

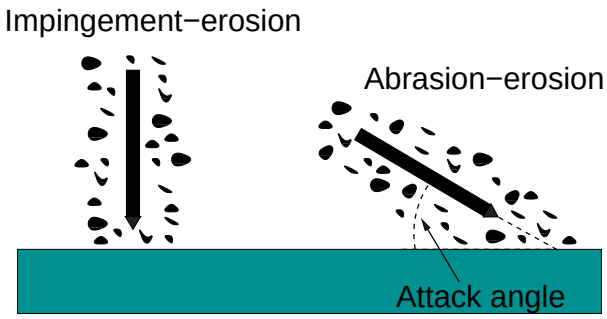

Figure 1.18: Schematic of representation of the different types of solid particle erosion..

Erosive wear mechanisms include ploughing or extrusion, fragmentation or microcracking and cutting (Tabrett et al., 1996, Zum Gahr, 1998). Ploughing occurs when material is plastically displaced or extruded away from the wear particle to form plastically deformed ridges adjacent the wear groove. No material is removed during ploughing, however, the highly deformed material is removed by subsequent passages of abrasive particles. The cutting mechanism involves the direct removal of material as primary debris or microchips with little or no displacement of material adjacent to the wear groove and is akin to a micromachining process. Fragmentation or microcracking occurs when highly concentrated stresses are imposed by abrasive particles causing material to become detached from the surface due to crack formation and propagation. Microploughing and microcutting are generally considered the dominant wear mechanisms on ductile materials while microcracking is generally considered the dominant wear mechanism on brittle materials.

In erosive wear environments the cutting removal mechanism was at one stage thought to account for the majority of material removal in the erosion of ductile metallic materials such as aluminium alloys and plain carbon steels (Levy, 1995, Zum Gahr, 1998). However, more recent research has found that an extrusion-forging mechanism at all particle impact angles, referred to as the platelet mechanism of erosion, is the dominant material removal mechanism. The platelet mechanism of erosion consists of a sequential plastic deformation process, as a result of ploughing, that continually extrudes and work hardens the material until it reaches the maximum strain rate and material is removed as small fractured chips, Figure 1.19. The erosion of brittle materials, such as ceramics and tool steels, is generally a result of the impacting abrasive particles causing cracking and fragmentation of micro-sized pieces of materials.

Figure 1.19: Platelets at edge of primary erosion zone on 1100-0 aluminium. Velocity, 62 m/s, impingement angle 60°, 20x magnification (Levy, 1995) .

During erosion there are a number of inter-related factors that act synergistically which can influence the rate of erosion. One of the most important factors effecting the erosion wear rate is the particle velocity which has been shown experimentally to obey a power law relationship with respect to velocity (i.e. erosive wear rate = Velocity to the power n) (MTIA, 1986, Adler and Dogan, 1999, Sarkar, 1980, Zum Gahr, 1998). Typical velocity exponents (n) on ductile materials range between 2 to 3, while on brittle materials a range from 3 to 4 can be expected.

The particle attack angle is another important factor that has a strong influence on the rate of erosive wear. Ductile metallic materials show a higher wear rate under abrasion-erosion or at impingement angles less than about 30°, Figure 1.20 (Zum Gahr and Doane, 1980). This is due to the ability of the erosive particles to more effectively microcut, microplough and extrude material on the wear surface. At increasing attack angles, the erosive wear of ductile materials reduces, reaching a minimum at approximately 90°. This is due to the ability of the material to plastically deform and absorb the impact energy. Brittle materials show increasing wear with increasing attack angles reaching a maximum under impingement erosion conditions at 90°, Figure 1.20. At low impingement angles or under abrasion-erosion conditions, the high hardness and the high strength of the microconstituents of brittle materials reduces the ability of abrasive particles to penetrate the surface and remove material by microcutting or microploughing. Due to the lower toughness of brittle materials, under impingement erosion conditions the mechanism of material removal is dominated by microfracture and cracking as a result of Hertzian stresses produced due to particle impingement. The attack angle is influenced by the hydraulic conditions, with turbulent flows resulting in a mixture of attack angles and accelerated erosive wear (Day, 1982). Smooth flows, or laminar flows,

carrying solid particles generally result in lower erosive wear rates.

Figure 1.20: Variation in erosion rate for varying impingement angles for ductile and brittle materials. (a) Aluminium (ductile) and aluminium oxide (brittle) eroded by 127 μm silicon carbide particles at 152 m/s. Note the differences in scale for aluminium and aluminium oxide (Finnie, 1995). (b) Aluminium and glass eroded with 300 μm iron spheres at 10 m/s (ASM, 1992) .

The size, shape and physical properties of the abrasive particles influence the erosion of a material. Decreasing abrasive particle size below about 100 μm generally results in lower wear rates as there is an increased tendency for elastic rather than plastic deformation (ASM, 1996). Abrasive particles that are more likely to fracture can create additional sharp cutting edges (Zum Gahr, 1998). Angular particles are more effective at indenting and micromachining the surface than rounded particles. In general, angular particles cause a higher wear rate than rounded or spherical particles for a given average size. The hardness of the abrasive particle relative to the hardness of the material being eroded is a critical parameter in abrasive and erosive wear. An abrasive having a high hardness is more effective at indenting and removing material than an abrasive with a lower hardness. However, as the hardness of the wearing material approaches the hardness of the abrasive, a reduction in wear can occur because the nature of contact can become elastic.

The plastic deformation characteristics of a material influence the extent of ploughing and cutting material removal mechanisms (Tabrett et al., 1996, MTIA, 1986). Materials that exhibit high fracture toughness and ductility with a relatively low yield strength are likely to be eroded by ploughing. A material with high yield strength and with low ductility and fracture resistance will erode by fragmentation.

The hardness of a material is an indication of the resistance to penetration by a hard indentor (Zum Gahr, 1998). Therefore, a higher material hardness, or more importantly the hardness of the wearing surface, affects the ability of the abrasive particles to penetrate the wear

surface and their ability to deform or cut material. However, the hardness of a material is not always a good indication of erosion performance.

1.5.2 Erosive Wear of High Chromium White Irons

There is limited literature on the erosive wear of high chromium white iron castings or weld overlays. Many of the erosive wear investigations have used a gas-blast test apparatus or a test apparatus that gives impact velocities in excess of 25 m/s. A summary of the relevant investigations, together with impact velocity, impingement angle(s), the type(s) of abrasive particles used and the test apparatus is given in Table 1.11. The work by Llewellyn and Dolman (2004) and Llewellyn et al. (2002) investigated the erosive wear of high chromium white iron casings used for service in the minerals processing industry to transfer slurries. The erosion tests results from the Coriolis erosion test apparatus used by Llewellyn and Dolman (2004) were found to correlate well with plant service trials. It should be noted that although there are several similarities between low-stress abrasion and erosion, the erosion of dual phase materials such as high chromium white irons does not follow the same characteristics observed for abrasion (Aptekar and Kosel, 1985, Stevenson, 1995, Sapate and Rama Rao, 2004).

Table 1.11: Summary of some relevant erosion investigations on high chromium white irons.

Author	Impingement velocity (m/s)	Impingement Angle (°)	Abrasive Particle	Erosion Test Apparatus
Aptekar and Kosel (1985)	40-43	30, 50, 70, 90	Alumina Rounded quartz Crushed quartz	Gas-blast Rotating arm
Stevenson and Hutchings (1995)	40	20, 30, 60, 90	Quartz Silicon carbide Blast furnace sinter	Gas-blast
Sapate and Rama Rao (2004)	25, 50, 90	30, 90	Quartz Alumina Blast finance sinter	Gas-blast
Adler and Dogan (1999)	40, 70, 100	90	Tungsten carbide spheres Alumina	Gas-blast Rotating arm
Chatterjee and Pal (2006)	30	90	Quartz Iron ore	Gas-blast

High chromium white irons are a dual phase material, consisting of a brittle carbide phase and a more ductile, tougher matrix phase. The duplex microstructure of high chromium white irons results in a mixed mode of material removal mechanisms (Levy, 1995, Day, 1982). The erosion behaviour is sometimes characterized as being intermediate between ductile materials and brittle materials (Aptekar and Kosel, 1985, Sapate and Rama Rao, 2006). Depending on the erosive wear environment, the erosive wear of high chromium white irons can result in the preferential removal of the softer matrix phase leaving the carbides standing proud of the matrix, or the preferential removal of the carbide phase leaving the carbides recessed with respect to the matrix. The erosive wear resistance of high chromium white irons depends on a number of different microstructural parameters such as the volume fraction, spacing and size of the carbides, the properties of the matrix and the interfacial bonding between the carbides and the matrix (Zum Gahr, 1998, Stevenson, 1995). However, it is generally agreed that the susceptibility of the carbides to fracture is the rate controlling factor in the erosive wear of high chromium white irons (Stevenson, 1995, Aptekar and Kosel, 1985) (all of them using gas jet).

The erosive wear environment has a strong influence on the ability to fracture or damage the carbides with the type of abrasive particle being the most significant factors. Abrasive

particles having a hardness equal or greater than the M_7C_3 carbides, such as silicon carbide or alumina (Table 1.12) are more effective at indenting, scratching and fracturing the carbides as well as efficiently removing the matrix. Quartz, which is the most common abrasive mineral present in virtually all of the solids being pumped around the red side of the alumina refinery, is softer than the M_7C_3 carbides and can not effectively indent the carbides (Day, 1982). However, quartz is effective at fracturing the carbides below the surface causing a gross loss of material, or chipping the edges of exposed carbides (Aptekar and Kosel, 1985, Stevenson and Hutchings, 1995)). After the abrasive particles have caused carbide fracture the carbides are left level with the matrix or recessed with respect to the matrix at the wear surface. The shape of the abrasive particles also influences the ability to fracture the carbides. Rounded quartz particles are found to be more effective at fracturing the carbides than crushed, angular quartz particles due to their ability to create larger Hertzian cracks. The crushed quartz particles were more effective at removing the matrix but not at causing significant cracking of the carbides. When the abrasive particles are much softer than the carbides, such as blast furnace sinter or iron ore, the ability to fracture and chip the carbides is not as significant and the carbides usually protrude above the matrix.

Table 1.12: Hardness of microstructural phases present in high chromium white irons and the hardness of abrasive phases (Tabrett et al., 1996).

The erosion of high chromium white irons and the susceptibility of carbides to fracture is further influenced by the impingement angle. While some investigations have found that there was no significant relationship between impingement angle and the rate of erosion (Aptekar and Kosel, 1985), others have found the erosion rate to increase with increasing impingement angle up to about 90^o, with peaks in erosion having been reported at impingement angles of about 60^o (Sapate and Rama Rao, 2004, Stevenson, 1995, Sapate and Rama Rao, 2006). In a particular instance, the erosive wear rate of a hypereutectic high chromium white iron weld overlays under normal impingement conditions using quartz and silicon carbide

abrasives was greater than the erosive wear rate of a low carbon steel. At lower impingement angles of 20 and 30°, the erosive wear rate of the weld overlays was found to be far superior to that of the low carbon steel. The variation in the erosion resistance with varying impingement angle was explained in terms of the susceptibility of the carbides to fracture. At high impingement angles, carbide fracture is found to occur more readily but at oblique impingement angles, carbide fracture does not occur as readily and the carbides can afford the matrix more protection (Stevenson and Hutchings, 1995, Stevenson, 1995). The carbide-matrix interface is often considered the weakest part of the material and is the origin of crack nucleation (Stevenson, 1995).

The carbide volume fraction (CVF) of primary and/or eutectic M_7C_3 carbides is one of the common microstructural features used to model the erosive wear resistance of high chromium white irons. The CVF increases with increasing carbon content from hypoeutectic to eutectic to the high CVF hypereutectic alloy compositions. If carbide fracture is the dominant wear mechanism, increasing the CVF will generally lead to an increase in the erosion rate. However, if wear of the matrix is the dominant wear mechanism, increasing the CVF will lead to an improvement in erosive wear resistance. The effect of CVF on the erosive wear of high chromium white iron weld overlays is most easily illustrated by reference to Figure 1.21. A decrease in the erosive wear rate with increasing CVF was found to occur under mild erosive conditions where the carbides remained proud of the matrix irrespective of impingement angle Figure 1.21(a). The influence of the impingement angle is illustrated in Figure 1.21(b) where gross fracture of the primary carbides was noticed to occur at 90° and erosion increased with increasing CVF, but at 30° impingement the carbides were found to be proud of the matrix and erosion decreased with increasing CVF under moderately severe erosion conditions. Under severe erosion conditions, the carbides were found to be level with or depressed with respect to the matrix for both 30 and 90° impingement angles. Increasing the CVF only slightly decreased the erosive wear resistance at 30° impingement but greatly increased erosive wear at 90° impingement, Figure 1.21(c).

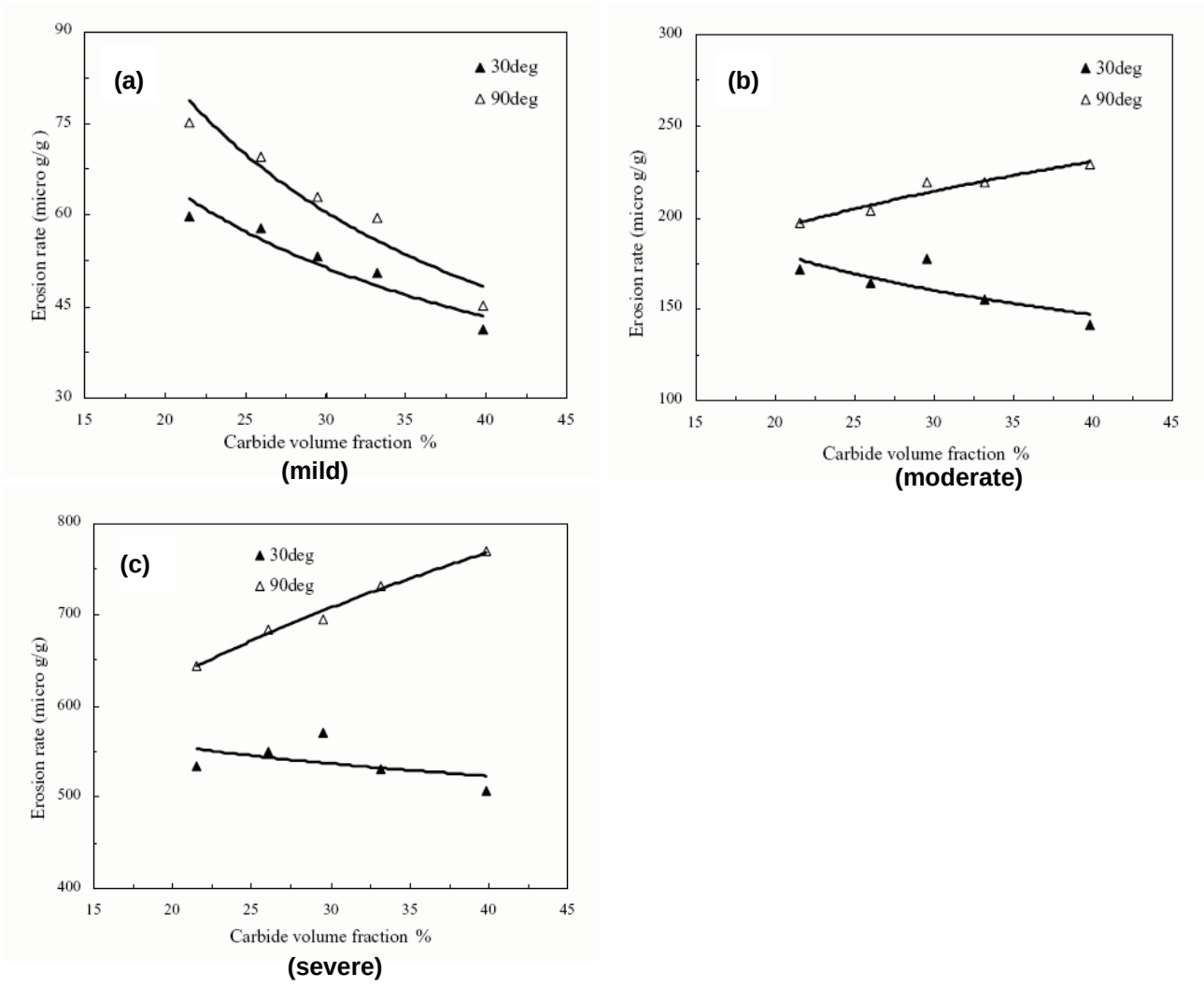

Figure 1.21: Variation in the erosion rate as a function with carbide volume fraction (CVF) under different impingement angles, abrasive particle size and impingement velocity (Sapate and Rama Rao, 2004).

Llewellyn and Dolman (2004) found using the low stress scouring Coriolis test method that the erosive wear decreased with increasing CVF from hypoeutectic compositions through to hypereutectic compositions having a CVF of about 22% and 44% respectively. Day (1982) reported that the best wear resistance for slurry pumps is achieved with a microstructure of discontinuous carbides in a matrix of 90-98% martensite with the finest possible matrix spacing and a uniform distribution of carbide displaying minimal alignment . The low stress abrasion/erosion resistance was found to improve with a high CVF and fine primary carbides in hypereutectic high chromium white irons (Llewellyn and Dolman, 2004). Coarse primary M_7C_3 carbides in a hypereutectic high chromium white iron were found to have a propensity to spall under low stress abrasion/erosion .

The erosion investigation by Chatterjee and Pal (2006) on high chromium white iron weld overlays found that the wear rate was influenced by the microstructure and the erodent used. Tests were done using quartz and iron ore particles at an impingement angle of 90^o and a

particle velocity of 30 m/s. When 210-300 μm quartz particles were used as the erodent, there was no reduction in erosion rate with increasing CVF, Figure 1.22(a). However, when softer 210-300 μm iron ore particles were used, the erosion rate decreased with increasing CVF, Figure 1.22(b). These differences in erosion wear rate were attributed to the differences in material removal mechanisms for the quartz and iron ore particles used. The harder quartz particles would cause the carbides to crack and produce large debris particles, while the iron ore particles would not cause fracture of the carbides. When the erosion rate was compared with the bulk hardness of the materials investigated, it was found that there was no relationship and wear resistance did not decrease with increasing hardness irrespective of whether quartz or iron ore particles were used.

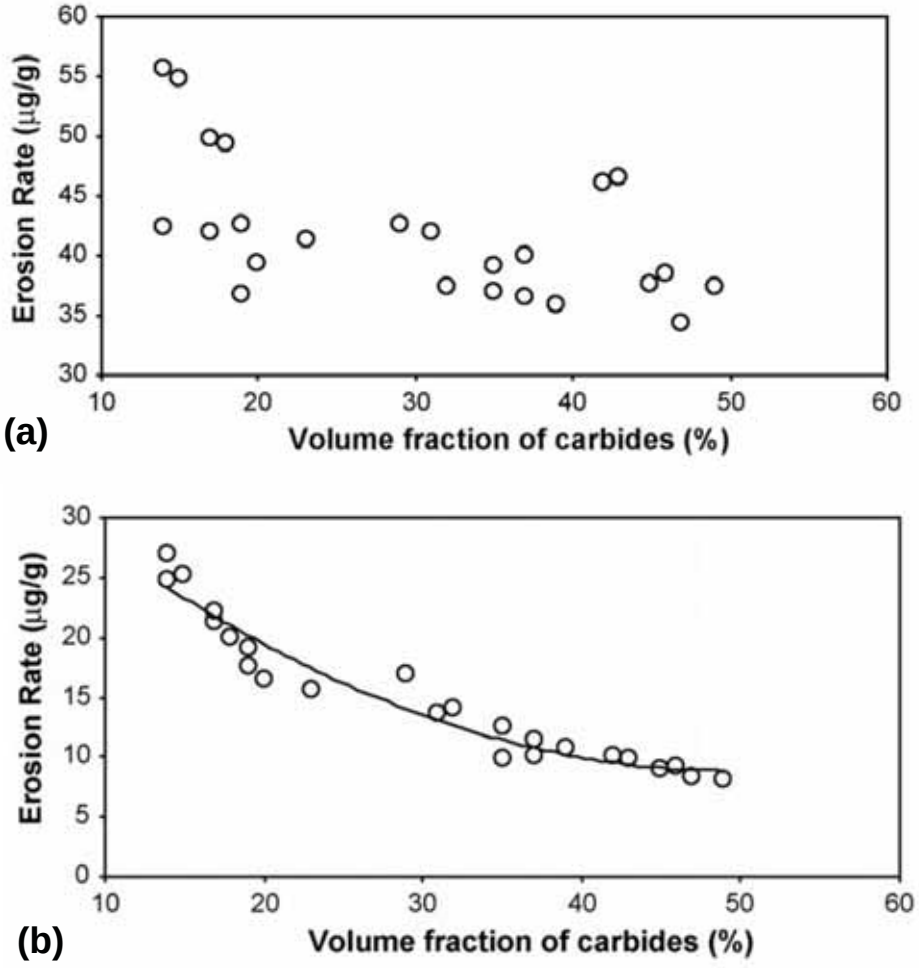

Figure 1.22: Erosion rate versus carbide volume fraction for various high chromium white iron weld overlays. (a) 210-300 μm quartz particles as the erodent. (b) 210-300 μm iron ore particles as the erodent (Chatterjee and Pal, 2006).

The erosion of high chromium white irons is found to increase with increasing particle velocity (Adler and Dogan, 1999, Sapate and Rama Rao, 2004, Stevenson, 1995). Stevenson (1995) found the rate of erosive wear increased approximately as the cube of the velocity over the 30 to 59 m/s velocity range studied. The velocity exponent was also found to be in-

dependent of particle impact angle. Therefore, large decreases in erosive wear were possible for a small reduction in particle impingement velocity.

The role of the matrix is to support the carbides and the removal of the matrix is important as once the matrix is removed, it exposes the carbides, making the carbide susceptible to fracture and chipping at the edges (Stevenson, 1995, Francis et al., 1998). Matrix removal mechanisms were found to be independent of the erodent used and occurred by ductile cutting and ploughing, leading to material removal by surface fatigue after subsequent impacts (Stevenson, 1995). Adler and Dogan (1999) found erosion occurred by a similar mechanism referred to as platelet formation. Platelets, which are thin extruded plates of the wearing material, form due to the continuous extrusion of crater lips formed by single particle impacts.

The properties of the matrix of high chromium white irons can be changed by heat treatments. The most common heat treatment being a destabilization heat treatment to transform the dominantly austenitic as-cast microstructure to martensite and secondary carbides. As a result of the heat treatment, the hardness of the matrix and the overall bulk hardness of the alloy can be increased. Even with a martensitic matrix, the maximum attainable hardness is less than the hardness of the the most common abrasive, quartz (Day, 1982).

The literature review on the erosion corrosion of high chromium white irons has highlighted the importance of understanding and characterizing the wear environment. If this is not done correctly, inappropriate materials may be selected. For example, if carbide fracture in high chromium white irons is the dominant wear mechanism, it is highly plausible that a single-phase steel having similar properties to the high chromium white iron matrix would offer superior wear performance.

1.6 Erosion-Corrosion

1.6.1 Introduction

Erosion-Corrosion is the acceleration or increase in the rate of deterioration or attack on a wear surface due to the relative movement between a corrosive fluid and the metal surface (Fontana, 1986). All types of components exposed to a moving fluid are subjected to erosion-corrosion, particularly bends, elbows, tees, valves and pumps. The wear surfaces are very similar to those produced by erosion except that rounding of holes and pits may also be seen due to corrosion. Erosive and corrosive wear mechanisms acting simultaneously can cause failure in a relatively short time and the failure is generally unexpected (Fontana, 1986).

Yue et al. (1987) presented a series of equations to describe the wear due to metal wastage in any form of erosion-corrosion environment is the sum of a corrosion rate in the presence of erosion and an erosion rate in the presence of corrosion, Equation 1.10. This method of characterizing erosion-corrosion has been widely adopted by other researchers (Zhou et al.,

1996, Stack et al., 1999, 1997, Tu et al., 2004, Barik et al., 2005).

$$K_{ec} = K_c + K_e \tag{1.10}$$

Where:
K_{ec} is the overall erosion-corrosion rate of metal wastage,
K_c is the total rate of metal wastage due to corrosion, and
K_e is the total rate of metal wastage due to erosion
Note: the terms used are in accordance with those used by Stack et al. (1997)

In the majority of cases involving erosion and corrosion, the total material wastage is greater than the sum of the separate erosion and corrosion wear contributions (Neville and Hodgkiess, 1999, Zheng et al., 2000). The additional wear loss found in erosion-corrosion environments is related to the interaction of erosion and corrosion. This can be described as the sum of the corrosion rate in the absence of erosion (pure corrosion), the erosion rate in the absence of corrosion (pure erosion) and the interaction of erosion-corrosion, Equation 1.11.

$$K_{ec} = K_{cO} + K_{eO} + \triangle K_{ec} \tag{1.11}$$

Where:
K_{cO} is the corrosion rate in the absence of erosion,
K_{eO} is the erosion rate in the absence of corrosion, and
$\triangle K_{ce}$ is the erosion-corrosion interaction

Combining Equation 1.10 and Equation 1.11 gives Equation 1.12. This describes that the erosion-corrosion interaction is the sum of the effect of corrosion on erosion and the effect of erosion on corrosion. The effect of erosion on corrosion is referred to by some authors as the additive effect (Yue et al., 1987, Stack et al., 1997) while other other authors refer to the effect of corrosion on erosion and erosion on corrosion as the synergistic effect. (Zheng et al., 1995, Li et al., 1995).

$$\triangle K_{ec} = (K_c - K_{cO}) + (K_e - K_{eO}) = \triangle K_c + \triangle K_e \tag{1.12}$$

Where:
$\triangle K_c$ is the additive effect of erosion on corrosion, and
$\triangle K_e$ is the synergistic effect of corrosion on erosion.

Combining equations Equation 1.11 and Equation 1.12, describes the total wear loss due to erosion-corrosion as the sum of a pure corrosion component, a pure erosion component, an additive effect of erosion on corrosion and a synergistic effect of corrosion on erosion, Equation 1.13.

$$K_{ec} = K_{cO} + K_{eO} + \triangle K_c + \triangle K_e \tag{1.13}$$

Collecting the corrosion related terms of Equation 1.13, gives Equation 1.14

$$K_c = K_{cO} + \triangle K_c \tag{1.14}$$

Collecting the erosion related terms of Equation 1.13, gives Equation 1.15.

$$K_e = K_{eO} + \triangle K_e \tag{1.15}$$

The pure corrosion and pure erosion terms are relatively well understood, however, the additive and synergistic terms are not well understood and sometimes difficult to quantify. The combined additive and synergistic effect is a significant factor and in some erosive-corrosive environments can account for up to 85% of the total wear (Yue et al., 1987).

1.6.2 Erosion-Corrosion of High Chromium White Irons

Investigations of the erosion-corrosion of high chromium white irons reported in the literature are limited, with the majority of the investigations concentrating on the wet grinding of ores (Sailors and Owens, 1982, Pitt and Chang, 1986, Meulendyke et al., 1987, Dodd et al., 1985) or the transfer of slurries (Ma et al., 1990, Lu et al., 2006, Watson et al., 1995, Llewellyn and Dolman, 2004, Zumelzu et al., 2002) in solutions with pH ranging from 1 to 11. Erosion-corrosion investigations relevant to the alumina processing industry, in highly alkaline pH 14 solutions, have been reported by Arnold et al. (1998) and Tu et al. (2004). Arnold et al. (1998) qualitatively examined worn hypereutectic high chromium white iron weld overlayed pipe spool components used for the transport of slurries in the alumina refining process. Tu et al. (2004) investigated the erosion-corrosion of two different hypoeutectic high chromium white iron castings in an alumyte slurry using a laboratory based electrochemical erosion-corrosion testing device.

In general, the wear of high chromium white irons in erosive-corrosive environments is significantly influenced by the matrix. The purpose of the matrix is to support the brittle carbides which impart the wear resistance (Stevenson, 1995, Arnold et al., 1998). It has previously been discussed that corrosion primarily attacks the matrix and that erosion of the matrix occurs due to a harder particle eroding away the softer matrix material, eventually causing

the carbides to fracture and spall . Arnold et al. (1998) found that the wear of weld overlayed pipe spools used in the alumina industry was found to be severely affected by corrosion as well as the expected erosive and abrasive wear mechanisms. Preferential dissolution of the austenitic matrix occurred when the chromium content of the matrix was less than 12%. This reduced the support for the wear resisting chromium carbides and resulted in fracturing of the carbides and spalling from the surface. It is therefore apparent that in erosive-corrosive environments, due to the interaction of erosion and corrosion, higher matrix and overall wear rates can be expected.

As previously discussed, in pure corrosive environments the corrosion resistance of high chromium white irons generally increases with increasing matrix chromium content and the abrasion/erosion resistance in pure abrasive/erosive environments generally increases with hardness and carbide volume fraction (Sailors and Owens, 1982, Ma et al., 1990, Llewellyn and Dolman, 2004). However, in erosive-corrosive environments, the most abrasion resistant white iron generally has the lowest corrosion resistance and the most corrosion resistance white iron generally has only average abrasion resistance. It is therefore of significant importance in erosive-corrosive environments to establish the contribution of corrosion, erosion and the interaction between erosion-corrosion on the overall wear performance to optimize material performance. For example if erosion is the dominant wear mechanism, increasing the wear resistance by increasing the carbide volume fraction or hardness will result in improved erosion-corrosion performance (Ma et al., 1990, Dodd et al., 1985, Tu et al., 2004).

Tu et al. (2004) found that the contribution of erosive wear in a highly alkaline pH environment using an alumyte slurry accounted for approximately 60% of the total weight loss, indicating that erosion was the dominant wear mechanism in this environment. Pitt and Chang (1986) found that the weight loss resulting from pure erosion in pH 5.5 to 10.5 solution was approximately constant, except for a slight decrease above a pH of 10 which was attributed to changes in surface passivating films on the materials surface. In the pH 5.5 to 7.5 solution they found the pure erosion component of the total weight loss represented approximately 25 to 55% of the total weight loss. Above a pH of 8.5, the pure erosion component represented approximately 60 to 75% of the total weight loss.

However, a number of investigators have proposed that corrosion is responsible for 50 to 80% of the total wear in erosive-corrosive environments (Dodd et al., 1985, Meulendyke et al., 1987). However, many of these investigations included the erosion-corrosion interaction ($\triangle K_{ec}$) as part of the total corrosion contribution. A likely reason for this is that the erosion-corrosion interaction generally appears to be related to the corrosion tendency of the sample (Pitt and Chang, 1986). The majority of investigations on high chromium white irons have found that the contribution of pure corrosion generally represents only a small fraction of the total material loss in erosive-corrosive environments (Dodd et al., 1985, Pitt and Chang, 1986, Ma et al., 1990). Tu et al. (2004) found that the contribution of pure corrosion in a highly alkaline pH 14 environment was less than 1% of the total weight loss for hypoeutectic

13Cr and 18Cr alloys. Pitt and Chang (1986) found that for a 3.4C, 18Cr heat treated high chromium white iron that the contribution of pure corrosion was generally less than 10% of the total weight loss for the pH 5.5 to 10.5 environments investigated. The contribution of pure corrosion was found to decrease with increasing pH values and above a pH of 9.5 the pure corrosion represented less than approximately 4% of the total weight loss.

The interaction between erosion and corrosion, $\triangle K_{ec}$ in Equation 1.11, is responsible for a considerable proportion of the total material weight loss. Tu et al. (2004) found that for two hypoeutectic high chromium white irons investigated, that the interaction of erosion-corrosion was responsible for about 36 to 39% of the total weight loss in the highly alkaline alumyte slurry solution used. Pitt and Chang (1986) found that the interaction between erosion and corrosion was influenced by pH. In low pH solutions, the erosion-corrosion interaction could represent up to 67% of the total material weight loss. However, as the pH was increased to approximately 9.5, the erosion-corrosion interaction reduced to approximately 33% and a increased in pH to 10.5 further reduced the erosion-corrosion interaction to about 22% of the total weight loss. The reduction in the erosion-corrosion interaction was attributed to the better corrosion resistance of the iron-chromium matrix due to the formation of a more protective oxide film. These findings are consistent with Ma et al. (1989) who also found that as the pH of the slurry was increased to 3, a significant reduction in the overall erosion-corrosion wear rate occurred and erosive/abrasive wear becomes the dominate wear mechanism.

It has been found that the chemistry of the erosive particles can cause a galvanic effect between the mineral in the slurry and the material that enhances the material's corrosion tendency (Pitt and Chang, 1986, Dodd et al., 1985). However, quartz, which is the major mineral found in erosive-corrosive environments (Gundlach and Parks, 1978), is an electrochemically inert mineral that generally does not affect the basic corrosion mechanism on a metal specimen (Pitt and Chang, 1986). The hard quartz particles, however, are effective in removing protective oxide layers which leads to an increase in the erosion-corrosion interaction. Quartz particles were found to be responsible for the initiation of pitting on the wear surface of high chromium white irons in alkaline pH slurries. Spalling of the metal around the pits was also observed. Meulendyke et al. (1987) found that pitting or the inter-phase corrosion that commonly occurred adjacent to the carbide-matrix interface would result in the spalling of the carbides and could represent up to 60% of the total wear.

1.7 Summary

The literature review has discussed the microstructural development, corrosion, erosion and erosion-corrosion wear of high chromium white irons. The current knowledge on the development of microstructure in high chromium white irons concentrated on heat treated hypoeutectic high chromium white irons which are the most widely used in industry. However,

hypereutectic castings and weld overlays are increasingly used to improve wear performance and the reported literature on the development of hypereutectic microstructures is increasing.

The literature on the corrosion of high chromium white irons is not extensive. The literature review did not identify any specific trends that can broadly be applied to all environments with the exception that increasing chromium content of the matrix is likely to improve corrosion performance. The test environments ranged from acidic pH 1 to alkaline, with only a couple of investigations done in highly caustic pH 14 environments. Evident from the literature review was the influence that the corrosive environment and the presence of chemical species can have on corrosion. The ranking of corrosion performance of a range of high chromium white irons in a neutral pH environment is not necessarily the same as a high pH environment.

The erosive wear of high chromium white irons has generally focused on high particle velocity tests, with limited investigation relevant to the transfer of slurries. There was general agreement that irrespective of the wear environment, the role of the matrix is to support the carbides to prevent fracture and accelerated wear. It was also agreed that erosion increases with velocity by a power law relationship and increasing angle of attack.

The literature on the erosion-corrosion behaviour of high chromium white irons is very limited. It is accepted that erosion-corrosion can be characterized in terms of the contribution of erosion alone, corrosion alone and the interaction between the erosion and corrosion mechanisms. To determine the interaction between erosion-corrosion an electrochemical test apparatus is required that has the ability to polarize a test sample to a specific potential.

1.8 Rationale for Current Work

The literature review has highlighted that the corrosion of materials is environment specific, however, little quantitative work has been done on the corrosion of high chromium white iron alloys in highly caustic pH 14 environments that are relevant to the alumina industry using the Bayer refining process. Furthermore, the presence of the aluminate ion in caustic sodium aluminate solutions has been found to influence the corrosion behaviour of low carbon steel. The influence the aluminate ion has on the corrosion of high chromium white irons has not yet been investigated.

The corrosion of high chromium white irons is reported to depend on microstructural properties such as carbide volume fraction (CVF) and composition of the phases. A number of different corrosion mechanisms for a range of high chromium white iron microstructures have been reported in the literature.

The erosion of high chromium white irons has been investigated by a number of people. However, the majority of reported erosion tests were done using test apparatus that gave impact velocities in excess of 25 m/s which is beyond that encountered in slurry transfer. Few

investigations have investigated the erosion of high chromium white irons under conditions that are analogous to slurry transfer and pumping as encountered in the alumina industry.

The wear of high chromium white irons used in the alumina industry is further complicated by the environment being erosive and corrosive which can lead to enhanced wear rates due to the synergistic effect of erosion-corrosion. However, little quantitative information has been reported in the literature on the erosion-corrosion behaviour of high chromium white irons in highly caustic environments.

The aim of this investigation is to examine the corrosion and wear behaviour of a number of high chromium white irons alloys that could be used for service in alumina refining plants. In addition by undertaking a microstructural study of a range of alloys in combination with corrosion and wear testing, it is anticipated that pertinent microstructural variables can be identified. Through an understanding of the microstructure of high chromium white irons, it should be possible to recommend alloys that will lead to reduced operating costs and downtime resulting from wear in alumina plants.

Part II

Equipment and Test Methods

Chapter 2

Equipment and Test Methods

2.1 Introduction

This chapter provides a general summary of the experimental techniques and methods used throughout this thesis. This encompasses the experimental equipment used and calibration methods where applicable.

2.2 Microstructural Characterization

The characterization of high chromium white iron alloys forms a crucial part of the investigation reported in this thesis. The sample preparation techniques and metallographic preparation techniques used for the characterization of the investigated materials are briefly summarized. Electron microscope facilities and chemical micro-analysis equipment were used at Adelaide Microscopy, which is the University of Adelaide's centre for electron beam instruments.

.

2.2.1 Sample Preparation

The samples investigated in this work were taken from large section pump castings or weld overlayed spools. Selected sections of the pump impeller castings or weld overlayed spools were plasma cut to manageable sizes for manipulation in a metallographic cut off machine. Samples for metallographic examination and experimental testing were further sectioned using an automated cut off machine (Struers Unitom-50) with a consumable carborundum cutting disk. Copious amounts of a water based cutting fluid/coolant were used during all cutting processes to ensure the cut faces of the samples did not undergo any microstructural changes due to thermal effects. All samples were sectioned a suitable distance from the

plasma cut region to negate any changes in microstructure due to thermal effects resulting from plasma cutting.

Samples from castings were sectioned approximately parallel or perpendicular to the cast surface. Weld overlay sections were taken transverse and longitudinally to the direction of the weld beads, Figure 2.1. (The viewing plane of the transverse samples is across consecutive weld beads and along the weld bead for the longitudinal sample).

Samples for metallographic examination were generally mounted in Bakelite using a hot mounting press. The mounted samples were wet ground using different grades of silicon carbide paper from 120 grit to a final 1200 grit finish. Prior to etching, the samples were polished to a 1 micron finish using polycrystalline diamond paste.

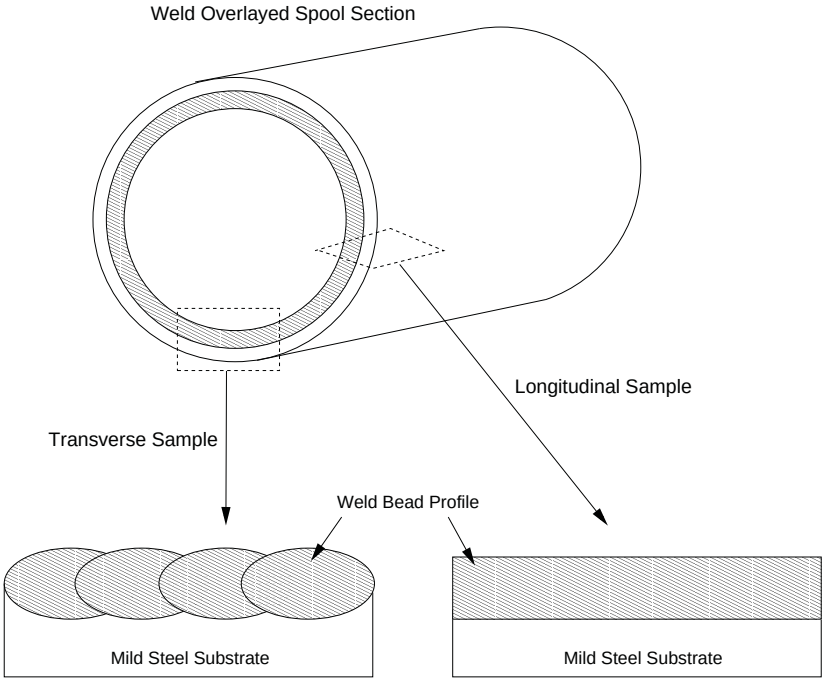

Figure 2.1: Schematic diagram showing the orientation of the weld beads in the transverse and longitudinal samples for metallographic examination.

2.2.2 Optical Light Microscopy

Optical microscopy was carried out using an Olympus BX60M optical light microscope with magnifications of 50, 100, 200 and 500 times. The microscope was equipped with a digital camera for microstructural image recording. Prior to microstructural examination in the optical light microscope, polished samples were etched. The common microstructural etchant used throughout this work was acid ferric chloride (5 g $FeCl_3$, 10 mL HCl, 100 mL H_2O).

2.2.3 Scanning Electron Microscopy and EDAX

Electron microscopy was done using a Philips XL30 Field Emission Scanning Electron Microscope (FESEM) or a Philips XL20 Scanning Electron Microscope (SEM). Both of the electron microscopes were fitted with EDAX analysis equipment that allowed the semi-quantitative chemical analysis of microstructural features to be determined in a very short time interval. Various samples were examined in the FESEM and SEM, including the samples used for optical microscopy, deep etched samples, worn plant samples, immersion test samples and erosion-corrosion test samples. These electron microscopes were found to be very useful for the examination of worn plant samples, corrosion immersion test samples and erosion-corrosion test samples due to the high spatial resolution and depth of field.

Typical operating parameters for both the FESEM and SEM were an accelerating voltage of 10-20 kV and a spot size of 3 to 4.

2.2.4 Electron Probe Microanalysis (EPMA)

Quantitative microanalysis of the high chromium white iron alloy samples was done by electron probe microanalysis (EPMA) using wavelength dispersive X-ray analysis (Cameca SX-51). The resolution of the EPMA machine is approximately 2 μm and analysis was of a volume approximately 1 to 2 μm cubed (analysis volume 6 to 8 μm^3). The beam current and accelerating voltage used were held constant at 60 nA and 20 kV, respectively. Count times were 5 seconds for each element analyzed. The elements analyzed were C, Si, Cr, Mn, Fe, Ni and Mo. Calibration of the probe was done on standards of known chemical composition for Si, Cr, Mn, Fe, Ni and Mo. Initially the carbon was calibrated on a stoichiometric M_7C_3 carbide. This gave good results for the analysis of the carbides but gave higher than expected carbon compositions for the matrix. For matrix carbon analysis, calibration was done on a standard containing 1.33 wt% carbon. To help improve carbon analysis results, an oxygen jet was used during the analysis process. However, even using a carefully controlled calibration and test procedure, carbon values were found to vary slightly more than for the other elements analyzed. This is attributed to the difficulties associated with light element analysis using a spectrometer based analysis system.

The 2μm resolution of EPMA allowed the chemical analysis of the primary M_7C_3 carbides of the weld overlays. However, the chemical analysis of the eutectic M_7C_3 carbides could not readily be determined due to the size of the carbides being less than or equal to the 2μm resolution of the machine. Both the primary and eutectic M_7C_3 carbides of the castings samples, being considerably larger than those of the weld overlay samples, could be analyzed. The chemical analysis of the matrix in weld overlayed samples was restricted to the austenitic halo regions surrounding the primary carbides as the small eutectic carbide spacing did not allow accurate chemical analysis of eutectic austenite regions.

All probe results for the carbides and matrix were based on a number of different analysis points and the results averaged. The spacing between successive analysis points of a line scan was 4 μm to ensure that there was no interference between analysed points.

2.2.5 Bulk Chemical Composition Determination

Bulk chemical compositions of the white iron alloys investigated was determined by an external company specializing in bulk chemical analysis of ferrous alloys. Bulk chemical analysis was carried out using optical emission spectroscopy for Mn, Si, S, P, Ni, Cr, Mo, Cu, V, Nb, Ti and the combustion carbon method for carbon analysis. For the weld overlay samples, the chemical composition was taken just below the wear surface. The bulk chemical analysis of casting samples was not considered sensitive to sample location.

2.2.6 Carbide Volume Fraction (CVF) Analysis

CVF analysis was done using image analysis software (analySIS). The most important aspect of using a software base CVF analysis program is the production of suitable images, being optical or electron micrographs, that will give good contrast definition between the phases. Back scattered electron (BSE) micrographs of metallographic samples polished to a 1μm finish were satisfactory for obtaining good CVF data. Figure 2.2 gives two examples of BSE micrographs. The analyzed carbide phase is highlighted in red, for a hypereutectic and hypoeutectic casting. Another advantage of using the electron microscope and BSE micrographs is the high magnifications that can be used. It was necessary to use magnifications up to 2000x in some cases to give reasonable spatial resolution between the carbide and matrix phases. The magnifications were generally 500x for hypereutectic castings (Figure 2.2(a)), 1000x for hypoeutectic and eutectic castings (Figure 2.2(c)) and 2000x for hypereutectic weld overlays. The results of the CVF analysis for any one sample represents the average of a number of micrographs taken from different sections, each analyzed over a range of several millimetres.

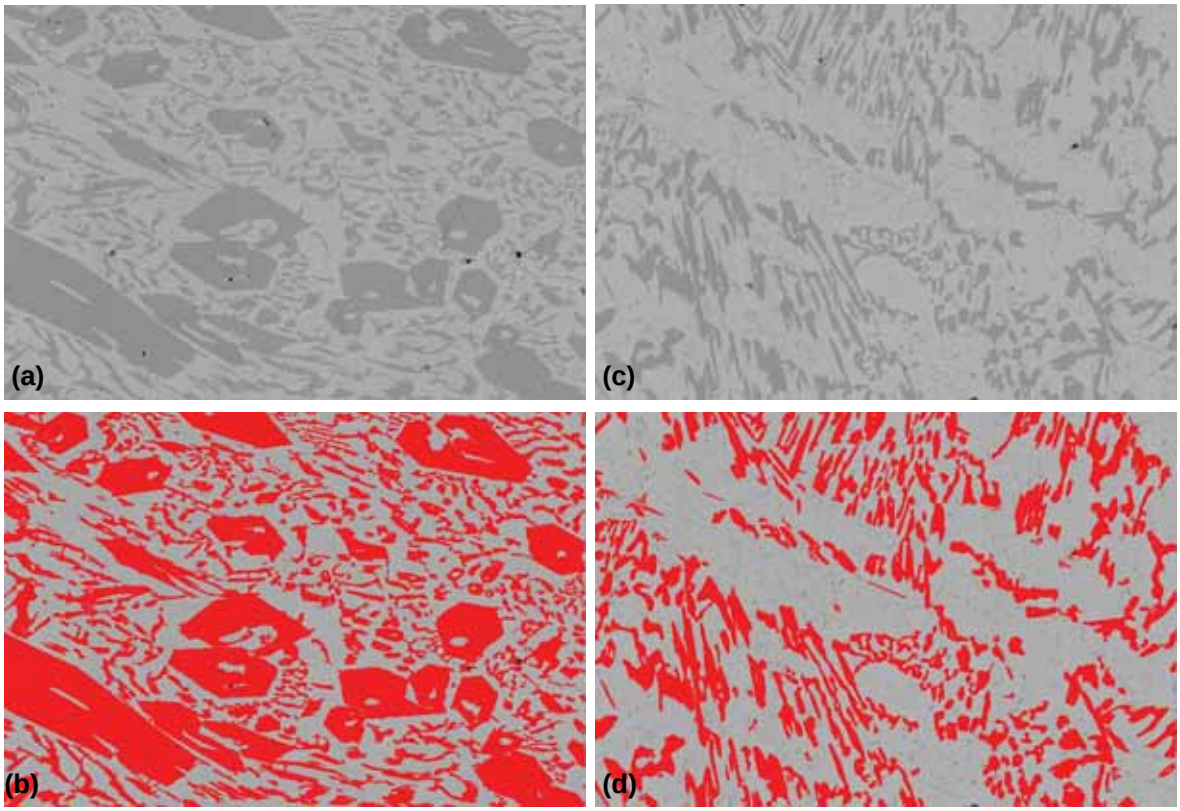

Figure 2.2: Backscattered electron micrographs of a hypereutectic and hypoeutectic casting samples, (a) and (b) respectively. The red sections in the corresponding micrographs, (b) and (d) show the carbides that were analyzed.

2.3 Heat Treatments

Heat treatments were done in air using a small laboratory bench top high temperature muffle furnace capable of temperatures up to 1400°C. The temperature of the furnace was accurately controlled via a PID controller with temperature feedback. For heat treatment temperatures above 1000°C, the temperature was increased by 50°C increments and allowed to equilibriate for approximately 10 minutes at each increment until the desired temperature was reached to prevent overloading of the elements due to the thermal lag of the thermocouples used for temperature feedback. The typical time to temperature is illustrated in Figure 2.3 and was reasonably quick due to the furnace having exposed elements located in the roof of the chamber.

To minimize oxidation of the high chromium white iron samples during heat treatment, the samples were tightly wrapped in at least two layers of austenitic stainless steel shim. This method, which is commonly practiced, minimizes the oxidation of samples being heat treated at temperatures up to 1150°C. The prepared samples were placed in the furnace on a K138 furnace brick before the furnace was switched on.

Heat treatments were undertaken at 950°C for destabilization and 1150°C for normalizing.

Specimens were held at the heat treatment temperature for 6 hours. After the required heat treatment period, the samples were removed from the furnace and cooled in still air.

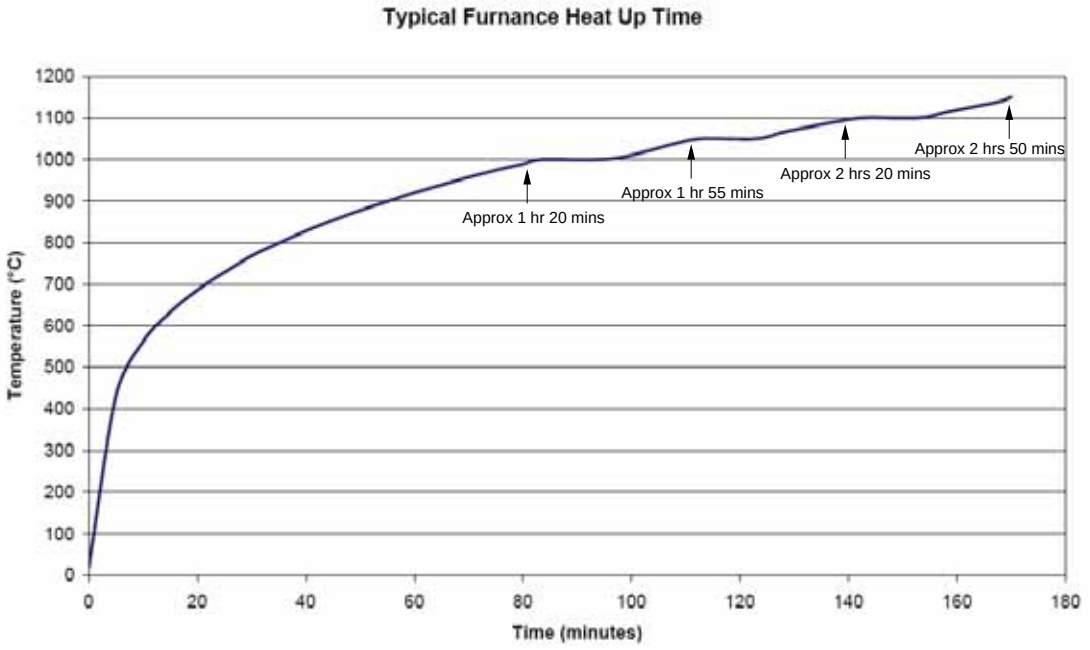

Figure 2.3: Curve illustrating the typical furnace heat up times for the furnace used in heat treatment. The set temperature was 1150°C.

2.4 Corrosion Tests

2.4.1 Potentiostat

The potentiostat used for all of the corrosion tests was a Gamry PCI4/750/Potentiostat - Galvanostat/ZRA having a maximum output current range of $\pm$750 mA and a minimum current resolution of 2.5 fA. The potentiostat was operated using the the Gamry Framework and DC105 corrosion techniques software which allowed fully automated corrosion measurements to be undertaken. The corrosion techniques included potentiodynamic polarization, corrosion potential measurements, Tafel tests to determine corrosion current and constant potential immersion tests.

Data analysis was done using the Gamry Echem Analyst software program. Echem Analyst was used for the graphical presentation of results and the determination of corrosion currents from Tafel tests.

2.4.2 Corrosion Test Cell

Corrosion tests were carried out in a purpose designed electrochemical corrosion test cell of the conventional three electrode type. The test cell allows the insertion of the test electrode, counter electrode, Luggin probe with salt bridge connection to the reference electrode, inlet and outlet for an inert gas and a thermometer. The arrangement is similar to the corrosion cell described in ASTM G5-94. The cell was constructed from glass and polymer materials that could operate continuously at 90°C in a concentrated caustic environment. A schematic diagram of the corrosion test cell, identifying the main components, is shown in Figure 2.4. The working volume of the test cell was approximately 1.5L. The counter electrode was manufactured from a 10 mm x 10 mm x 1 mm platinum sheet spot welded to a thin platinum wire housed in a glass tube. The reference electrode was positioned in an external reference compartment and connected to the Luggin probe, located in the test cell, via a salt bridge of the same composition as the test solution. The tip of the Luggin probe was positioned approximately 1.5 to 2 mm from the working electrode surface. The salt bridge was of the constant siphon type. The test cell was placed in a constant temperature water bath which maintained the temperature at 90$\pm$1°C. During testing, the elevated temperature test solution would cause the reference compartment to rise approximately 5°C above ambient temperature. The test cell could be deaerated by bubbling an inert gas through the solution, the rate of which could be controlled by an adjustable needle valve. The configuration of the test cell allowed the working electrode to be introduced into the deaerated, elevated temperature test solution without the need to disturb any of the other components.

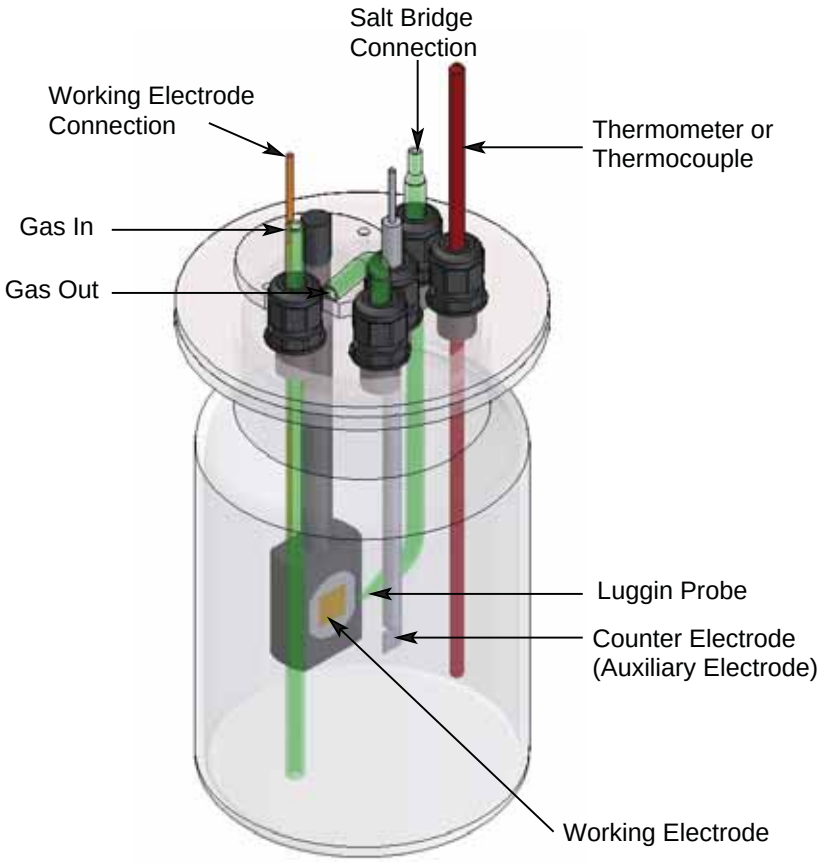

Figure 2.4: Schematic diagram of the corrosion test cell showing the main components.

2.4.2.1 Reference Electrode

The reference electrode used for all of the corrosion tests was a Red Rod reference electrode (REF 201) supplied by Radiometer Analytical. The Red Rod reference electrode is a proprietary high quality general purpose glass electrode that is suitable for testing in alkaline solutions over a temperature range of -10 to 100°C. The electrode is of the single junction type with a porous pin liquid junction and has a saturated KCl salt bridge (filling solution). The saturated KCl solution of the Red Rod reference electrode was periodically replaced and the reference potential of the electrode was periodically checked against a laboratory master Red Rod reference electrode. At no stage did the difference in potential between the electrode used for corrosion tests and the master electrode exceed 1 mV. The reference potential of the Red Rod and Calomel (SCE) electrodes compared with the standard hydrogen electrode (SHE) are given in Table 2.1.

Table 2.1: Reference potentials versus standard hydrogen electrode potentials (SHE) in mV (reproduced from the Red Rod Reference Electrodes Operating Instructions).

T°C	0	12	20	25	30	40	50	60	80	100
Red Rod	223	214	204	199	194	184	173	163	141	118
SCE (Hg_2Cl_2)	260	254	248	244	241	234	227	220	-	-

2.4.2.2 Calibration of Test Cell

To verify the performance of the test cell and potentiostat, a standard reference test was done. The standard test and experimental procedure is outlined in ASTM G5-94: Standard reference test method for making potentiostatic and potentiodynamic anodic polarization measurements. The test material specified is type AISI 430 ferritic stainless steel and the test solution specified is 1.0 N sulfuric acid. The AISI 430 ferritic stainless steel used for the standard tests was sourced locally and was in the form of 1 mm thick sheet. A 10mm x 10mm sample had a small diameter Teflon sheathed copper wire soldered to the back of the sample which was then mounted in epoxy resin (Struers EpoFix). The sample was wet ground to a 500 grit finish using silicon carbide paper, degreased in acetone, rinsed with deionized water and hot air dried immediately prior to immersion in the test solution.

After the test cell had been deaerated by bubbling nitrogen through the test solution, the open circuit potential (OCP) was recorded for 1 hour before the anodic polarization scan from the OCP to +1.6 V SCE was started at a scan rate of 0.6 V/h (0.17 mV/s). The results of a typical standard test are shown in Figure 2.5 together with plots of the minimum and maximum values provided in the standard for potentiodynamic polarization. The potential values of the Red Rod reference electrode used for the standard test was converted to the SCE scale by subtracting 0.045 V. This is the difference between the Red Rod scale and SCE scale at 25^{o}C based on the manufacturer's specification. The temperature of 25^{o}C corresponds to the temperature of the reference cell compartment that housed the reference electrode and not the test cell itself.

The results, as shown in Figure 2.5, are in good agreement with those in the ASTM standard G5-94 with only minor variations in current density and potential readings. These variations can be attributed to the variations in the AISI 430 ferritic stainless steel used for these tests and the tests reported in the standard as they are not from identical heats and may have a slightly different chemical composition and been processed in a different manner. Duplicate tests on the same batch of 430 ferritic stainless steel showed very little variation from the typical curve shown in Figure 2.5. The results of these calibration tests indicate that:

- The test cell configuration is suitable for potentiodynamic polarization tests.
- The deaearting of the test cell to reduce oxygen levels to negligible levels is adequate as the results are in good agreement with the values reported in the Standard. If there were any oxygen effects during the test, significant deviations in potential from the values in the standard and sporadic readings would have been seen.
- The potentiostat is operating correctly as current and potential readings are in close agreement with the limits stated in the Standard.
- Test results are reproducible.

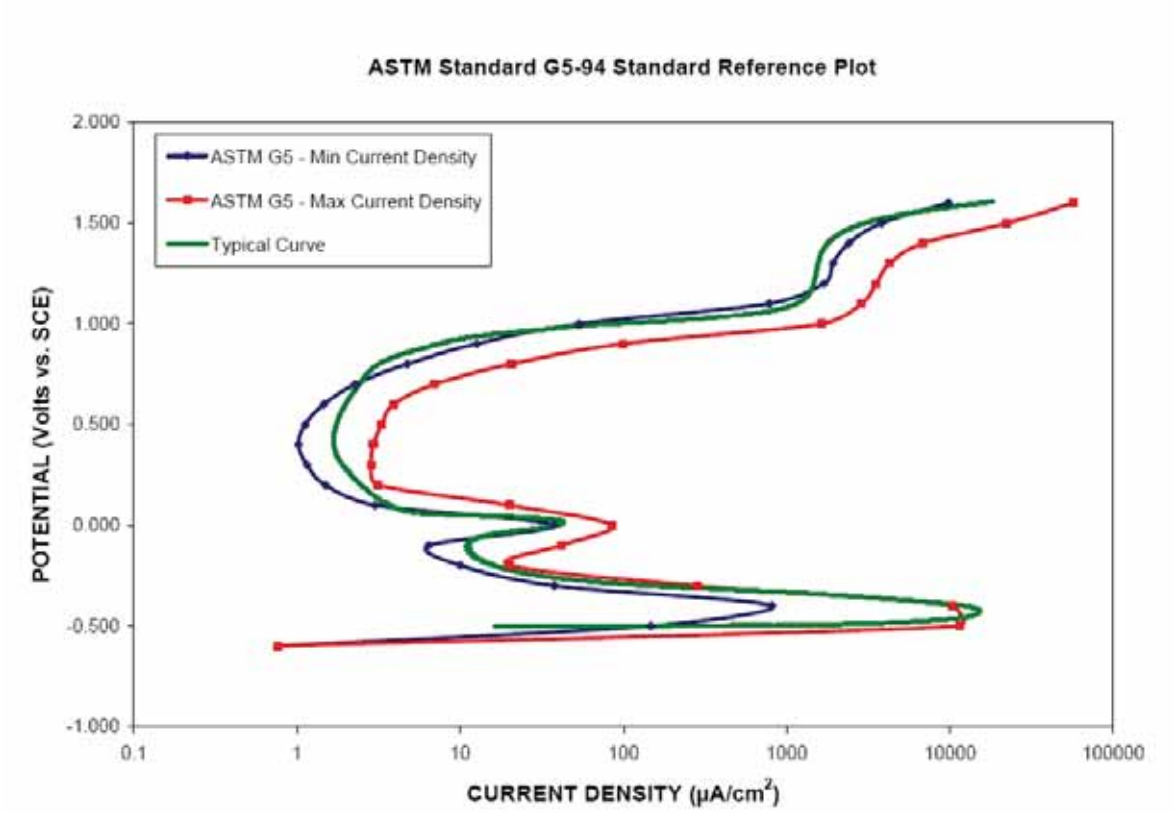

Figure 2.5: Calibration of corrosion test cell using ASTM G5-94: Standard reference test method for making potentiodynamic and potentiodynamic anodic polarization measurements.

2.4.3 Test Sample Preparation

The high chromium white iron corrosion test samples, or working electrode, consisted of samples that had an electrode surface area of approximately 15mm x 15mm. The actual dimensions of the working electrode surface were measured to $\pm$ 0.5 mm before being potted in epoxy resin. Tests samples were taken from castings, or weld overlays deposited on a steel substrate. The surfaces of the samples were initially wet ground on 220 grit silicon carbide paper. Electrical connections to the samples were made by soldering small diameter Teflon sheathed copper wires to their back face prior to potting.

Due to the high hardness and brittle nature of high chromium white irons, which does not readily facilitate machining or internal threading of the material, conventional mounting techniques using a compression gasket could not be used for mounting of the test sample. A mounting technique to expose a known surface area to the test solution had to be developed. The mounting technique had to be suitable for testing in concentrated caustic solutions at 90°C and prevent crevice corrosion effects. Initial tests on samples mounted in cold setting epoxy resin (Struers EpoFix) at 90°C found that the samples were susceptible to crevice corrosion.

The mounting technique developed consisted of first coating the test sample in a high temperature and chemically resistant adhesive (Araldite K138) and baking the adhesive coated sample at 110°C for approximately 1.5 hours. For easy manipulation during grinding, the sample was then mounted in a cold setting epoxy resin (Struers EpoFix), Figure 2.6. The working surface of the test samples was wet ground using successive grades of silicon carbide paper to a 1200 grit finish, rinsed with deionized water, degreased in acetone and finally rinsed with deionized water and hot air dried. This mounting method was found to minimize any crevice effects and was suitable for a single test at 90°C. After a test the sample was broken out of the mount and all surfaces of the test sample were wet ground to a 220 grit finish to remove all traces of the epoxy adhesive. The mounting process was repeated numerous times on the same sample to allow different tests to be done on the same sample.

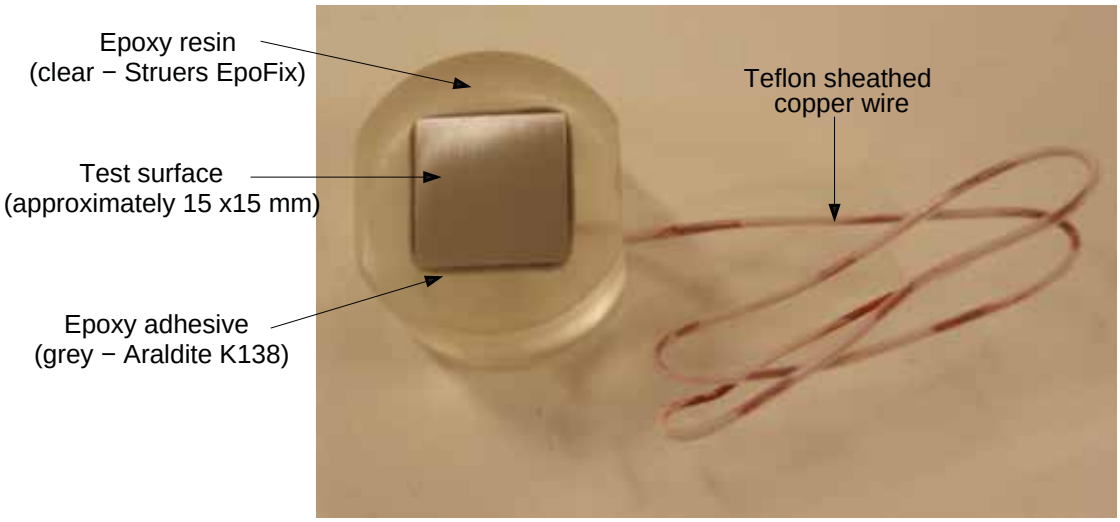

Figure 2.6: Typical corrosion test sample prior to corrosion testing illustrating the mounting configuration.

2.4.4 Test solution

All test solutions were prepared from analytical grade reagents and deionized water. The following reagents and materials were used for the preparation of sodium hydroxide and sodium alumina tests solutions:

- Sodium hydroxide, NaOH, supplied by Ajax chemicals (Assay 99.0% NaOH, 1.0% Na_2CO_3, all other impurities less than or equal to 0.02%).
- Aluminium wire 2.0mm diameter, rolled flat, thoroughly wiped with a cloth damped with acetone to remove surface contaminants and cut into pieces less than 20mm long. The wire pieces were further degreased ultrasonically in acetone, rinsed with distilled water and oven dried prior to weighing. (Typical wire analysis, 99.77% Al, 0.03% Si, 0.002% Cu, 0.013% Zn, 0.18% Fe, 0.003% Mn, 0.002% Mg).

2.4.4.1 Preparation of Sodium Aluminate Solutions (Synthetic Bayer Liquor)

Sodium aluminate solutions were prepared by dissolving high purity aluminium metal in sodium hydroxide solutions using a method adapted from the work of Counter (1997). The method used was found suitable to produce a solution that is characteristic, with respect to dissolved species and precipitation behaviour, of industrial Bayer liquors. The dissolution process was carried out in a specially constructed reaction vessel consisting of a polypropylene reaction beaker, Perspex lid and a stainless steel stirring rod, Figure 2.7. A condenser was also incorporated on the reaction vessel to vent reaction gasses to the atmosphere, whilst reducing water vapor losses. The reaction vessel was contained in a temperature controlled water bath held at 90°C to ensure the rapid and complete dissolution of the aluminium.

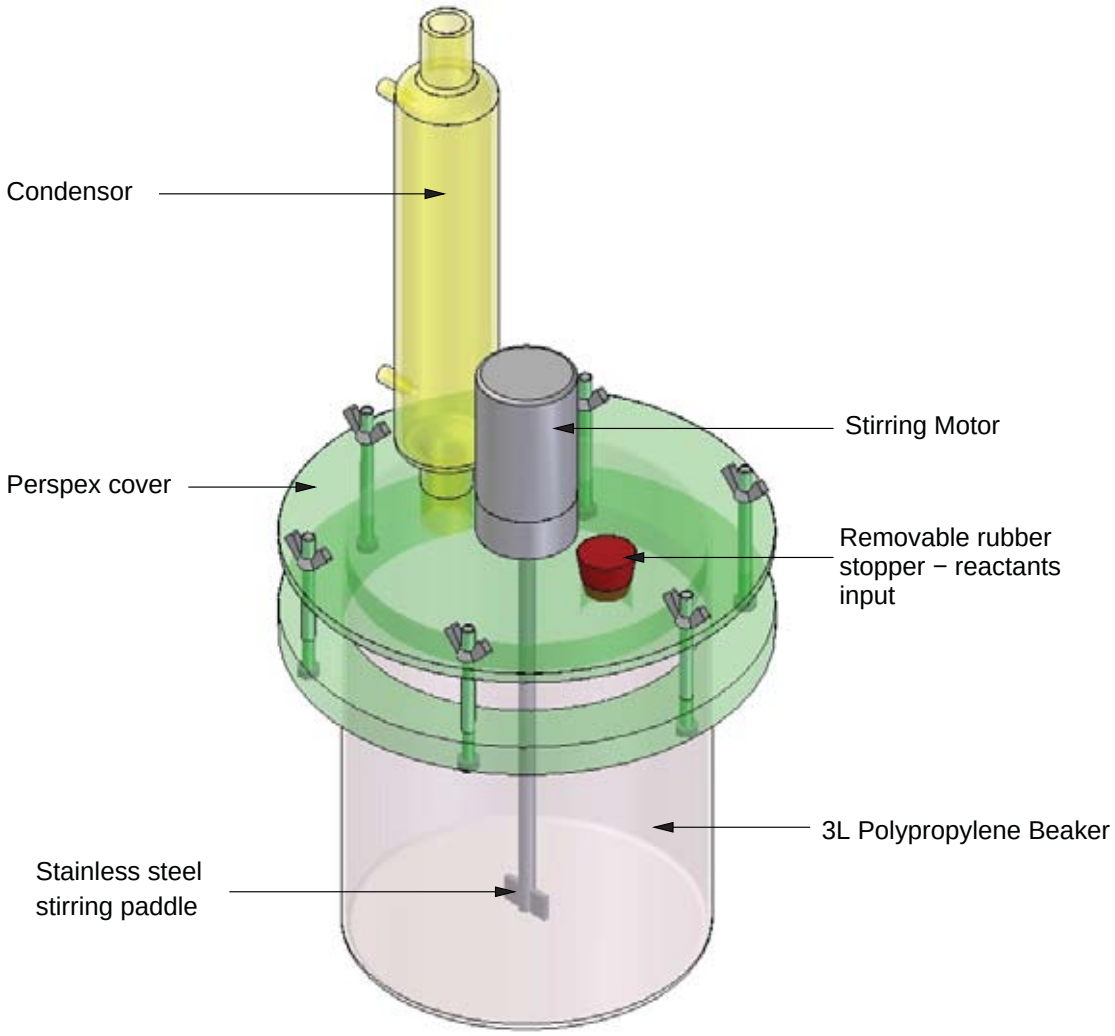

Figure 2.7: Reaction vessel used for the preparation of sodium aluminate solutions.

The target caustic concentration, which is typical of what may be found on the red side of an alumina refining process, was 256 g/L (expressed as g/L Na_2CO_3). The target alumina concentration was chosen such that the solution would contain the equilibrium amount of alumina at 90°C, which corresponded to 113.5 g/L (expressed as g/L Al_2O_3). The equilib-

rium amount of alumina in the caustic solution was used to ensure a stable sodium aluminate solution was achieved at the desired test temperature and was not susceptible to spontaneous precipitation of alumina hydrate. This alumina content is less than what could be expected on the red side of the alumina refining process.

The amount of the above mentioned reagents to prepare a 1 litre solution of sodium aluminate solution having a caustic concentration of 256 g/L and an alumina content of 113.5 g/L are 199.2 g of sodium hydroxide pellets and 60.2g of aluminium pieces.

The following procedure was used to prepare all the sodium aluminate solutions used for corrosion and erosion-corrosion testing. As previously stated the dissolution process was performed in a purpose built reaction vessel, Figure 2.7.

1. The appropriate amount of sodium hydroxide pellets were gradually added to approximately two thirds of the required amount of deionized water to form a concentrated caustic solution. The concentrated caustic solution also assists in the rapid dissolution of the aluminium.

2. The required mass of aluminium wire pieces were slowly added to the stirred caustic solution over a four to five hour period. The slow addition of aluminium to the caustic solution was to prevent the exothermic reaction causing the solution to boil. However, temperatures of the caustic aluminate solution would approach the boiling point of approximately 106°C.

3. Once all the aluminium had dissolved the vessel was cooled to approximately 80°C and the solution filtered through three layers of Whatman 540 filter paper and then through a Whatman GF/C glass microfibre filter. On both occasions a negative pressure was applied to the filtration vessel to assist in the filtration process. Small amounts of purified water were used to rinse the reaction vessel and filtration equipment to ensure all chemical species remained within the prepared solution.

4. The filtered solution was transferred to a glass volumetric flask and made up to the required volume using deionized water and well mixed.

5. The synthetic Bayer liquors were stored in airtight polypropylene containers for a short period of time and again filtered through a Whatman GF/C glass microfibre filter before use. The final solution was visually clear.

Solution analysis was done on three individually prepared batches of sodium aluminate solutions to verify concentrations. The analysis was done at the chemical testing laboratory of one of the alumina refinery project sponsors. The results of the solution analysis, Table 2.2, show that the preparation procedure gives consistent solution concentrations of 112.3$\pm$0.32 g/L (expressed as g/L Al_2O_3) alumina and 261.2$\pm$0.61 g/L (expressed as g/L Na_2CO_3) total caustic.

Table 2.2: Results of the solution analysis for three individually prepared batches of sodium aluminate solutions (synthetic Bayer liquor) and averaged results.

Sample	Alumina g/L	Caustic g/L	Alumina/Caustic
Batch 1 - sample 1	112.0	261.9	0.43
Batch 1 - sample 2	112.0	261.7	0.43
Average Batch 1	112.0	261.8	0.43
Batch 2 - sample 1	112.7	261.2	0.43
Batch 2 - sample 2	112.7	261.2	0.43
Average Batch 2	112.7	261.2	0.43
Batch 3 - sample 1	112.2	260.4	0.43
Batch 3 -sample 1	112.2	260.5	0.43
Average Batch 3	112.2	260.5	0.43
Average of all batches	**112.3**	**261.2**	**0.43**
Standard deviation	**0.32**	**0.61**	**0.00**

2.4.5 Polarization Scans Test Procedure

The following test procedure was used for potentiodynamic polarization corrosion tests. This test procedure is similar to the test procedure outlined in ASTM G5-94 which was used for the calibration of the test cell.

1. Approximately 1.5 L of freshly prepared test solution was placed in the test cell and approximately 500 mL into the reference compartment.

2. The filled corrosion test cell, with the Luggin probe, counter electrode, inlets and outlets for gas bubbling and a thermometer were inserted into the test chamber which was placed into the water bath which was preheated to approximately 60^{o}C.

3. The test solution within the test chamber was deaerated by bubbling high purity nitrogen (air Liquide Alphagaz) through the test solution for a minimum of 1 hour while the solution was heated to the test temperature of 90^{o}C.

4. The working electrode was freshly ground to a 1200 grit finish, rinsed with deionized water, degreased in acetone and finally rinsed with deionized water and hot air dried prior to immersion in the test solution.

5. The appropriate connections to the potentiostat were made and the rate of gas bubbling reduced.

6. The salt bridge was filled and allowed to equilibriate for 1 to 2 minutes.

7. The working electrode was conditioned at a cathodic potential of -1.304 V vs Red Rod for 10 minutes to reduce any oxides that may have formed on the test surface.

8. After conditioning of the electrode, the OCP was automatically measured for 10 seconds before the polarization scan was automatically started. The test parameters for potentiodynamic polarization scans were:

    - Starting potential of -0.050 V vs. Eoc
    - Final potential of 0.00 V vs Eref for high chromium white iron samples and 0.5 V vs Eref for steel and stainless steel samples
    - Scan rate of 1 mV/s

2.4.6 Tafel Technique to Determine Corrosion Rate

The Tafel test technique was used to quantify the corrosion current density at the rest potential. The test procedure was identical to the polarization scans test procedure except that the test parameters were:

- Starting potential of -0.25 V vs. Eoc
- Final potential of 0.25 V vs Eoc
- A reduced scan rate of 0.5 mV/s

The corrosion current densities were obtained from the Tafel test results using the Gamry Echem Analyst software program.

2.4.7 Immersion Test Procedure

The immersion test procedure is similar to the polarization scan test procedure with steps 1 to 7 the same. After conditioning of the electrode the open circuit potential was recorded or the potential of the working electrode was potentiostatically controlled for a period of 4 hours.

At the completion of the test, the working electrode was removed, cooled in purified water and any corrosion constituents were removed from half of the test sample by gently rubbing with a red rubber stopper (the red rubber stopper is hard enough to remove loosely adherent corrosion products but soft enough not to scratch the the sample surface). The sample was rinsed in acetone and hot air dried before examination using optical and electron microscopy.

2.5 Erosion-Corrosion Tests

Erosion-corrosion tests involved slurry pot tests using an apparatus that has previously been proven by Lathabai and Pender (1995). Tests were done at elevated temperatures in the sodium aluminate solution used for the corrosion tests.

During the project an improved erosion-corrosion test apparatus capable of recording electrochemical data under deaerated erosion conditions was designed and developed. The electrochemical erosion-corrosion test apparatus has provided some positive initial results.

2.5.1 Slurry Pot Tests

2.5.1.1 Slurry Pot Test Equipment

The slurry pot testing device used in this work, Figure 2.8, was similar to that used by Lathabai and Pender (1995). Six test samples in the form of square bars (9.8$\pm$0.1 mm $\times$ 9.8$\pm$0.1 mm $\times$ 40.0$\pm$0.1 mm) were mounted radially in a circular spindle and securely clamped in the device using nylon screws. The spindle and associated components were constructed from an acetal based engineering polymer that can withstand temperatures up to approximately 100°C. The spindle was coupled to a 0.75 kW variable speed motor and immersed in a 2 litre polypropylene beaker containing the test slurry. To prevent vortex formation and induce turbulent flow the beaker had four vertical polypropylene baffles located at 90° to each other. The rotational speed of the motor was set using a digital frequency controller to ensure the rotational speed was the same for all tests. The rotational speed was set at 1000 rpm, which corresponds to a wear velocity at the tip of the sample of approximately 5.6 m/s.

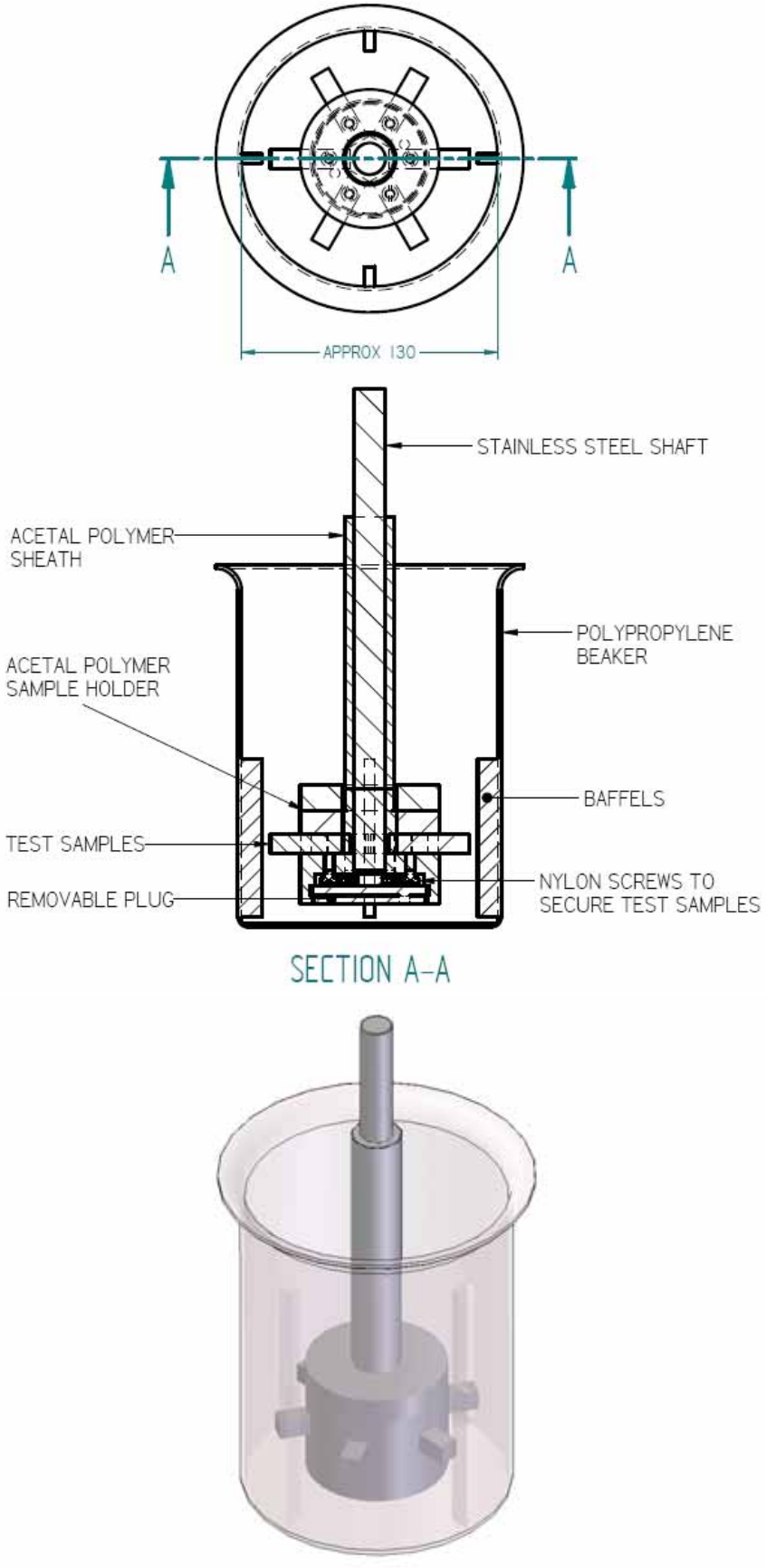

Figure 2.8: Schematic of the slurry pot test apparatus.

2.5.1.2 Slurry Pot Test Method

The test samples were surface ground to the desired size. For the hypereutectic weld overlay sample it was necessary to fill the check cracks with an epoxy resin to ensure that the cracks did not fill with quartz particles during testing as this would lead to errors and inconsistencies in results. This was done using standard vacuum impregnation techniques. Prior to being tested the sample's test face was wet ground to a 1200 grit finish using silicon carbide paper. This wet grinding was done so that the scratch marks were parallel with the long axis of the sample. The samples were then degreased in acetone and hot air dried prior to weighing to an accuracy of 0.1 mg. The test samples were tested in pairs and two mild steel reference samples were included in all tests to confirm the reproducibility of the tests. The test samples were placed in the sample holder such that the protrusion of the test samples was maintained at 19.0$\pm$0.1 mm. The assembly was placed in the preheated slurry and coupled to the motor. The temperature of the slurry was maintained by immersion of the slurry pot in a constant temperature water bath set to 90$\pm$1°C. The duration of the slurry pot test was 5 hours. At the completion of the test, the assembly was removed and cooled in purified water. The test samples were removed, any residual slurry constituents removed by gentle rubbing with a red rubber stopper, degreased in acetone and hot air dried prior to weighing. The weight loss of the sample was calculated and the test repeated to ensure reproducibility. The weight loss was calculated as the average of two tests and reported relative to the weight loss of the the mild steel samples.

2.5.1.3 Slurry Pot Abrasive

The erodent consisted of various sized quartz particles with the proportion of each sieve range given in Table 2.3. The particle size ranges and concentrations were based on average data from alumina refining operations using slurries as the transfer mechanism between stages. The quartz particles were sourced from a local sand supplier (Sloan's Sands Pty Ltd) and consisted of a mixture of angular and rounded particles, Figure 2.9. The test slurry contained 480g of abrasive particles in 720 mL of liquor, which is equivalent to approximately 40 wt% of solid to liquid.

Table 2.3: Particle size range of quartz particles used for slurry pot testing.

Sieve Range (μm)	Wt%
0-53	72.8
53-106	5.0
106-150	5.9
150-250	5.7
250-425	5.0
425-850	4.1
850-1000	2.4
1000-1400	4.8

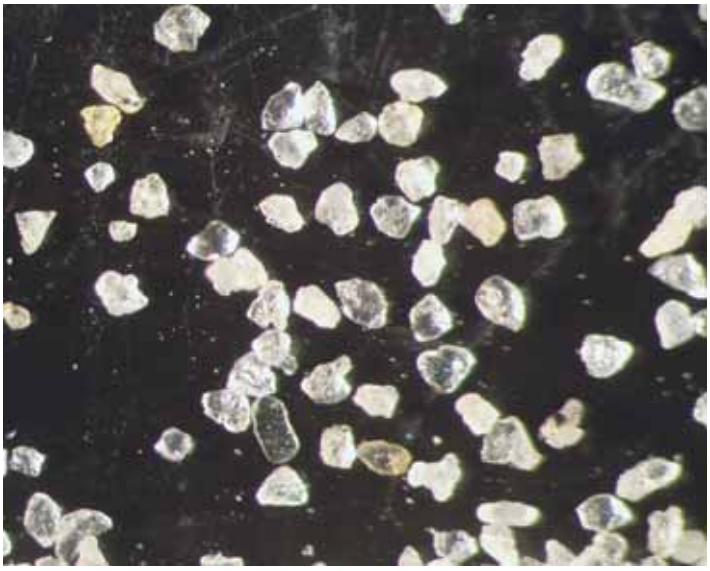

Figure 2.9: Image of the 106 - 150 μm quartz particles used for slurry pot testing.

2.5.2 Electrochemical Erosion-Corrosion Tests

2.5.2.1 Electrochemical Erosion-Corrosion Test Equipment

There is no standard erosion-corrosion test apparatus to undertake electrochemical erosion-corrosion testing. A purpose built erosion-corrosion test apparatus was designed and built, Figure 2.10, as part of this project to investigate the electrochemical corrosion behaviour of high chromium white irons in erosive environments.

The test apparatus is based on the slurry pot design, where a slurry is stirred within a circular pot, containing baffles, that create a turbulent environment Figure 2.11. The turbulent environment ensures the abrasive particles are suspended within the solution and impinge on the test sample surface to cause erosive damage. The slurry is capable of being stirred at different speeds to create turbulent environments of varying severity. In this particular

erosion-corrosion test apparatus the front surface of the sample has been positioned flush with the inside wall of the pot. The test sample has a test sample area of 20 x 20mm, Figure 2.13. The erosion-corrosion test apparatus is capable of performing tests over a range of temperatures up to 90°C by the use of a heated water jacket. Tests can also be done under deaerated conditions by maintaining an oxygen free atmosphere immediately above the solution in the test apparatus.

Electrochemical corrosion measurements with the erosion-corrosion test apparatus are measured using the conventional three-electrode technique as previously discussed (refer Section 2.4.5). The reference electrode is housed in an external reference compartment and connected to the test cell via a salt bridge of the test electrolyte Figure 2.12. The counter electrode is a 316L stainless steel sheet which is positioned on the inside of the lid of the test apparatus Figure 2.12.

Figure 2.10: General overview of the assembled electrochemical erosion-corrosion test apparatus showing enclosed test section, rotational speed controller and water bath.

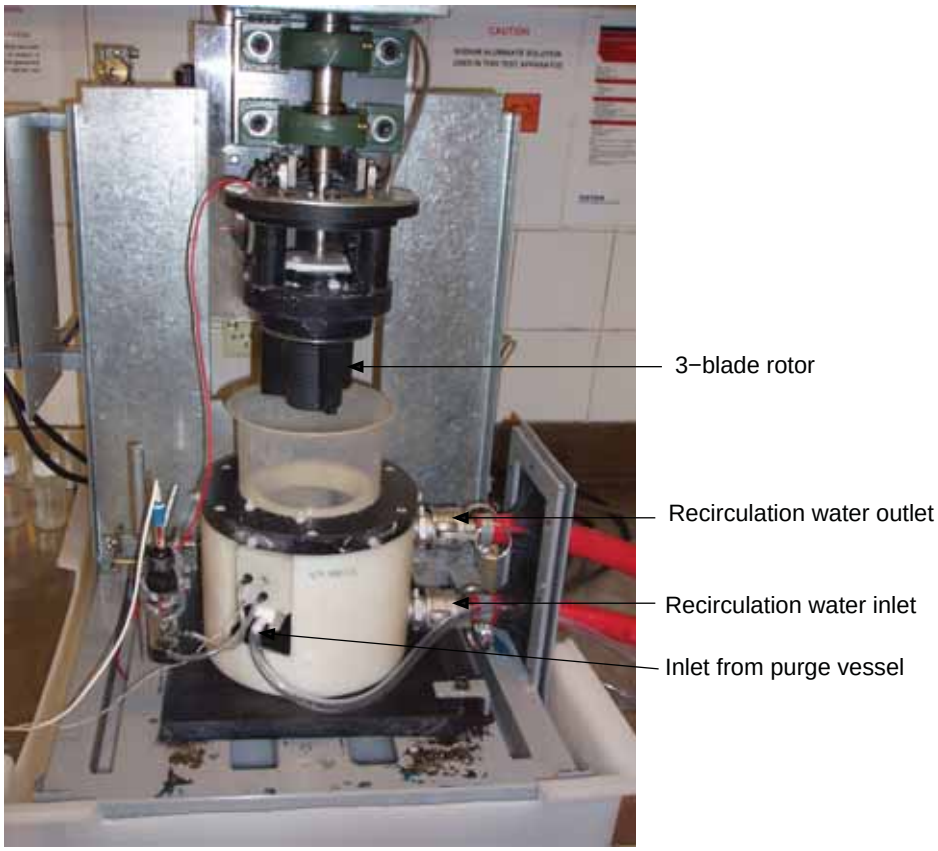

Figure 2.11: Overview of electrochemical erosion-corrosion test apparatus showing rotor section raised out of the test vessel, water recirculation connections and solution inlet from purge vessel.

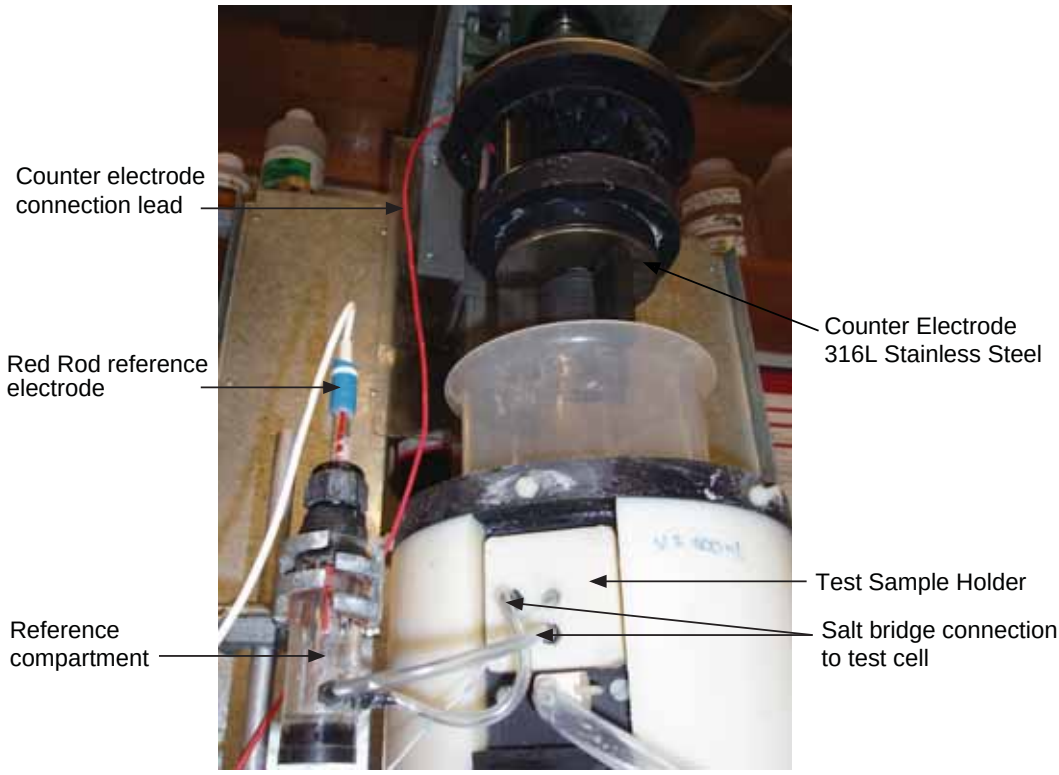

Figure 2.12: Overview of electrochemical erosion-corrosion test apparatus showing counter electrode, sample location, external reference compartment and connections.

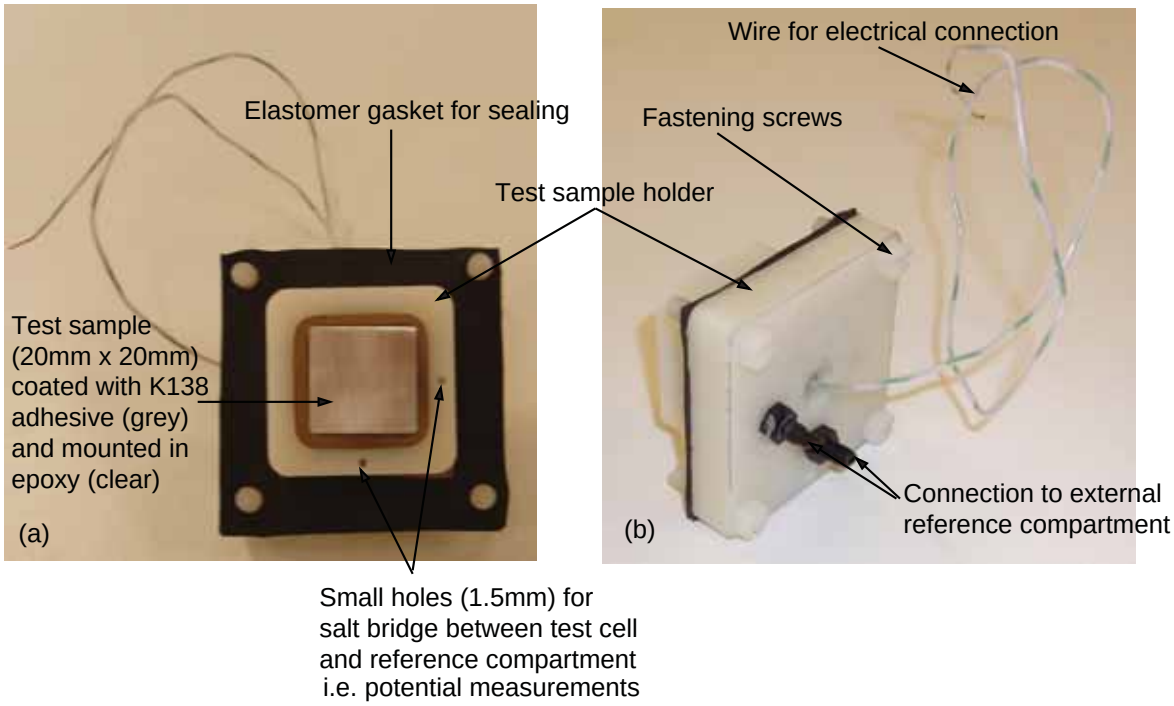

Figure 2.13: Overview of electrochemical erosion-corrosion test sample holder showing position of holes for connection to reference compartment.

2.5.2.2 Electrochemical Erosion-Corrosion Test Method

The erosion-corrosion test slurry consisted of a liquor phase and an abrasive phase. The liquor phase was the synthetic Bayer liquor used in the corrosion tests. The concentration of the abrasive particles was chosen to be 100g/L which is similar to what can be found in an alumina refining plant.

A typical experimental procedure consisted of heating the sodium aluminate solution, described previously to 90°C whilst deaerating by bubbling high purity nitrogen through the solution for a minimum of one hour. Whilst the solution was heating, the test sample was prepared by freshly grinding the test face of the sample to a 1200 grit finish, rinsing in deionized water, degreasing in acetone and finally rinsing with deionized water and drying in hot air. The sample was then placed in the erosion corrosion test cell. The abrasive particles were placed in the test cell, the stirrer and top lid were lowered into position and the test cell was purged with high purity nitrogen. The abrasive particles were the same type used for slurry pot testing described previously but at a concentration of 100 g/L. The test apparatus was heated to the test temperature by the circulation of hot water within the water jacket. After the erosion-corrosion apparatus had reached the equilibrium temperature, the hot, deaerated sodium aluminate solution was purged into the test cell to form the slurry. The apparatus was allowed to equilibriate for a further 10 minutes before the start of a test.

Polarization scans were done using a similar test method and test parameters as described by steps 5 to 8 in section 2.4.5, with the exception that during the final minutes of the sample conditioning, the stirring motor was switched on and set to the desired rotational speed before the polarization scan started.

2.5.2.3 Experimental Verification of Electrochemical Erosion-Corrosion Test Apparatus

In order to assess if the designed test apparatus could accurately measure the corrosion response of an alloy in an erosive-corrosive environment, a series of three trial test conditions was devised. The trial test conditions consisted of testing AISI 316L stainless steel in a static 1.0M sulfuric acid solution, a solution stirred at 600rpm and a solution containing 100 g/L of 150-250 μm quartz particles stirred at 600rpm. The sulfuric acid solution was deaerated and the test temperature was 30°C. The results of the trial are shown in Figure 2.14. It is known that 316L will form a passive Cr_2O_3 film over the exposed surface to significantly reduce the corrosion rate. Stirring the solution at 600 rpm, without particles, is expected to slightly alter the corrosion response of the stainless steel, but the stainless steel should still be capable of passivating. This is the case shown in Figure 2.14 where the rest potential has increased slightly and the current density for the majority of the potentials has increased slightly. When the abrasive quartz particles are added, the stainless steel can no longer passivate due to the

removal of the Cr_2O_3 oxide layer. This is represented by an increase in corrosion current density and non-steady current density reading in what was originally the passive region.

From these sets of tests it can be concluded that the test apparatus set up and procedure can satisfactorily measure the corrosion response of material under erosive-corrosive conditions.

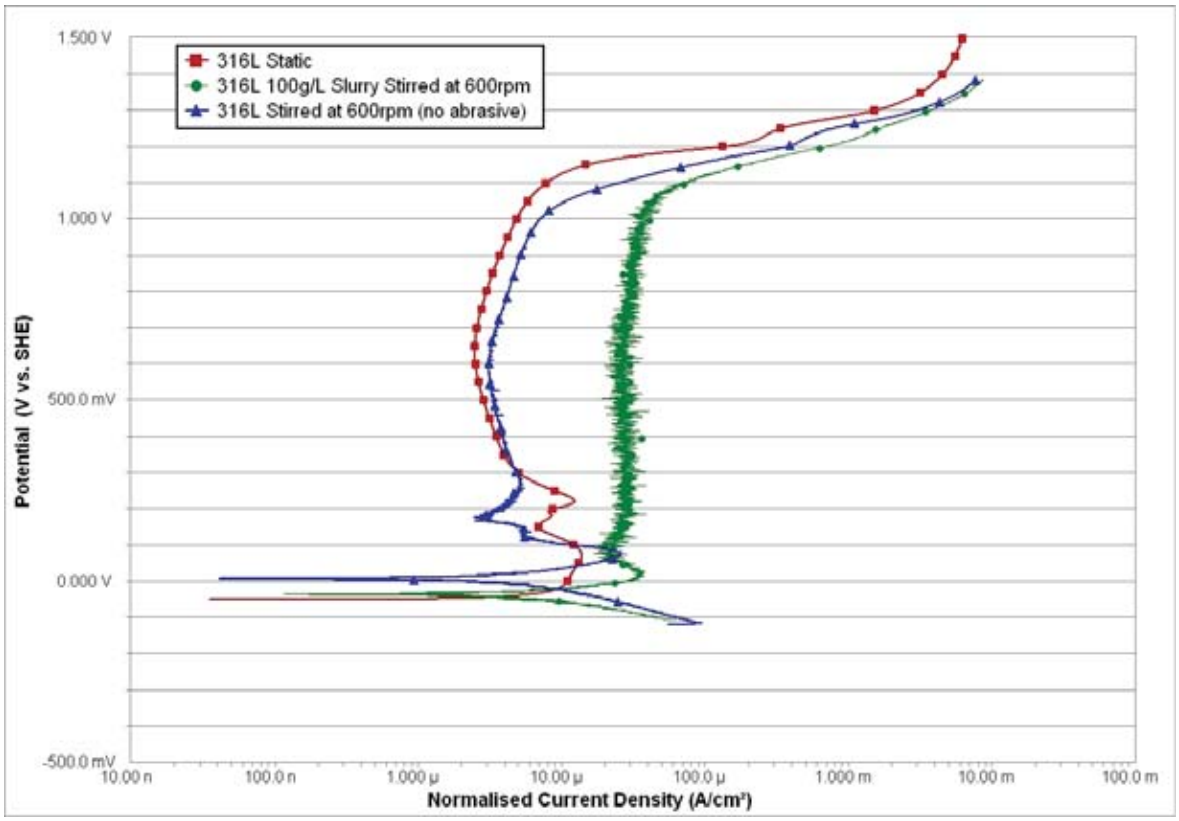

Figure 2.14: Polarization curves for AISI 316L stainless steel in deaerated 1.0M sulfuric acid under static, stirred and with 100 g/L of abrasive particles. Test temperature was 30°C.

Part III

Experimental Testing Philosophy

Chapter 3

Experimental Testing Philosophy

3.1 Introduction

The focus of this work is to develop an understanding of microstructure in high chromium white irons and the influence it has on the corrosion and wear behaviour in environments relevant to the Australian alumina industry utilizing the Bayer refining process. This has not been extensively reported in the literature. A better understanding of the corrosion and wear performance of high chromium white iron alloys will allow the selection of the most appropriate alloy to improve plant longevity and minimize operational costs.

3.2 Influence of Microstructure on Corrosion and Wear Performance

The literature review has highlighted that different microstructural features such as carbide morphology and the chemical composition of microstructural phases can have a significant influence on the corrosion performance of high chromium white iron alloys. The bulk hardness and carbide volume fraction have also been found to have an influence on the erosion wear performance of high chromium white iron alloys. The relationships between corrosion and erosion and the likely microstructural characteristics that influence their behaviour are illustrated in the block diagram, Figure 3.1. The overall erosion-corrosion wear performance of a material can also be considered the combined contribution of corrosion alone, erosion alone and a wear factor that takes into consideration the influence erosion has on corrosion or vice versa.

The development of microstructure in high chromium white irons is explained in terms of the bulk chemical composition and cooling rate during solidification, Figure 3.1. The cooling rate during solidification has been found to have a significant effect on the carbide morphology in weld overlays or at the chill surface in castings. The heat treatment after solidification

refers to destabilization or high temperature heat treatments, in the solid state, that alter the matrix phase. The chemical composition of the microstructural phases can be considered to be the chemical composition of the matrix and the chemical compositions of the carbides. The carbide morphology can be considered in terms of the carbide volume fraction, the inter-carbide spacing and the carbide size. The hardness can be considered the bulk hardness or the microhardness of the carbides and matrix phase constituents. Many of the microstructural characteristics such as chemical compositions of the carbides and matrix phases, bulk hardness and microhardness of the carbides and matrix, and carbide morphology can be quantified allowing their influence on corrosion, erosion and erosion-corrosion to be investigated and quantified.

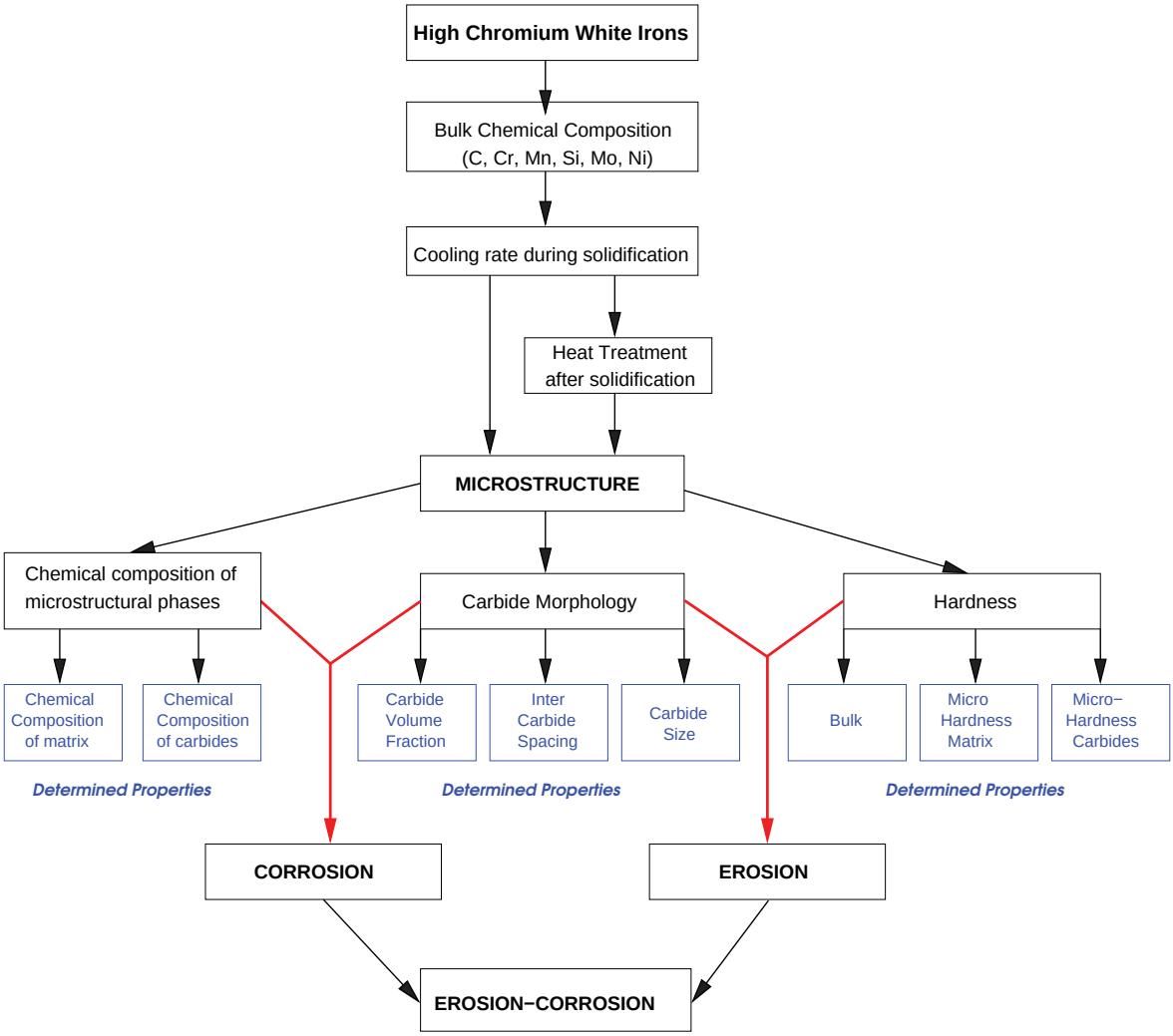

Figure 3.1: Factors influencing microstructure and hardness of high chromium white irons and their influence on corrosion and wear.

3.3 Materials Investigated

The previous section on the influence of microstructure on corrosion and wear performance, summarized in Figure 3.1, has shown that there are a number of microstructural charac-

teristics that are likely to influence corrosion and erosion performance. To investigate the influence of microstructure on the corrosion and wear performance, a range of materials varying in chemical composition, carbide morphology and hardness were tested. The materials investigated in this work consisted of high chromium white iron castings and high chromium white iron weld overlays. A low carbon (mild) steel (AS1163: C350LO) and an AISI 420 martensitic stainless steel were also included for comparative purposes. Table 3.1 summarizes the materials investigated, including the name adopted throughout this thesis, the form of the alloy and the source of the alloy.

Table 3.1: Samples investigated in this work

Name	Form	Source
HypoA	Casting	Commercially produced ex-service alumina plant pump impeller casting
HyperA	Casting	Commercially produced ex-service alumina plant pump impeller casting
EutecticA	Casting	Commercial produced locally sourced
HyperEXP	Casting	Experimental casting
WeldoverlayA	Weld overlay	Commercially deposited ex-service alumina plant pipe spool
WeldoverlayB	Weld overlay	Commercially deposited ex-service alumina plant pipe spool
AS1163: C350LO low carbon steel	Plate	Local supplier
AISI 420 martensitic stainless steel	Rod	Local supplier

Two of the high chromium white iron castings, HypoA and HyperA, and the two weld overlays investigated in this work were in the form of worn ex-service plant samples from different Australian alumina plants using the Bayer refining process. The worn ex-service plant samples provided materials that are currently used in alumina plants and examination of the wear surfaces gave an insight into the wear phenomenon in an alumina processing plant. Examination of the wear surface also enabled a comparison with wear surfaces from controlled laboratory tests which can be used to verify the suitability of laboratory tests to reproduce the wear surfaces found in alumina processing plants.

In addition to the two castings and two weld overlays sourced from ex-service plant components, other high chromium white irons were included in the test regime. This was done to increase the spread in chemical composition and carbide morphology. A commercially produced casting, EutecticA, having a lower bulk chromium content was locally sourced. Experimental casting, HyperEXP, having improved toughness compared with other hypereutectic castings and a high carbide volume fraction was also included. To illustrate the range in chemical compositions investigated, the bulk chemical compositions of all the high

chromium white iron castings and weld overlays are plotted on the metastable Fe-Cr-C liquidus surface, Figure 3.2. Figure 3.2 shows that the compositions range from hypoeutectic through to eutectic and hypereutectic.

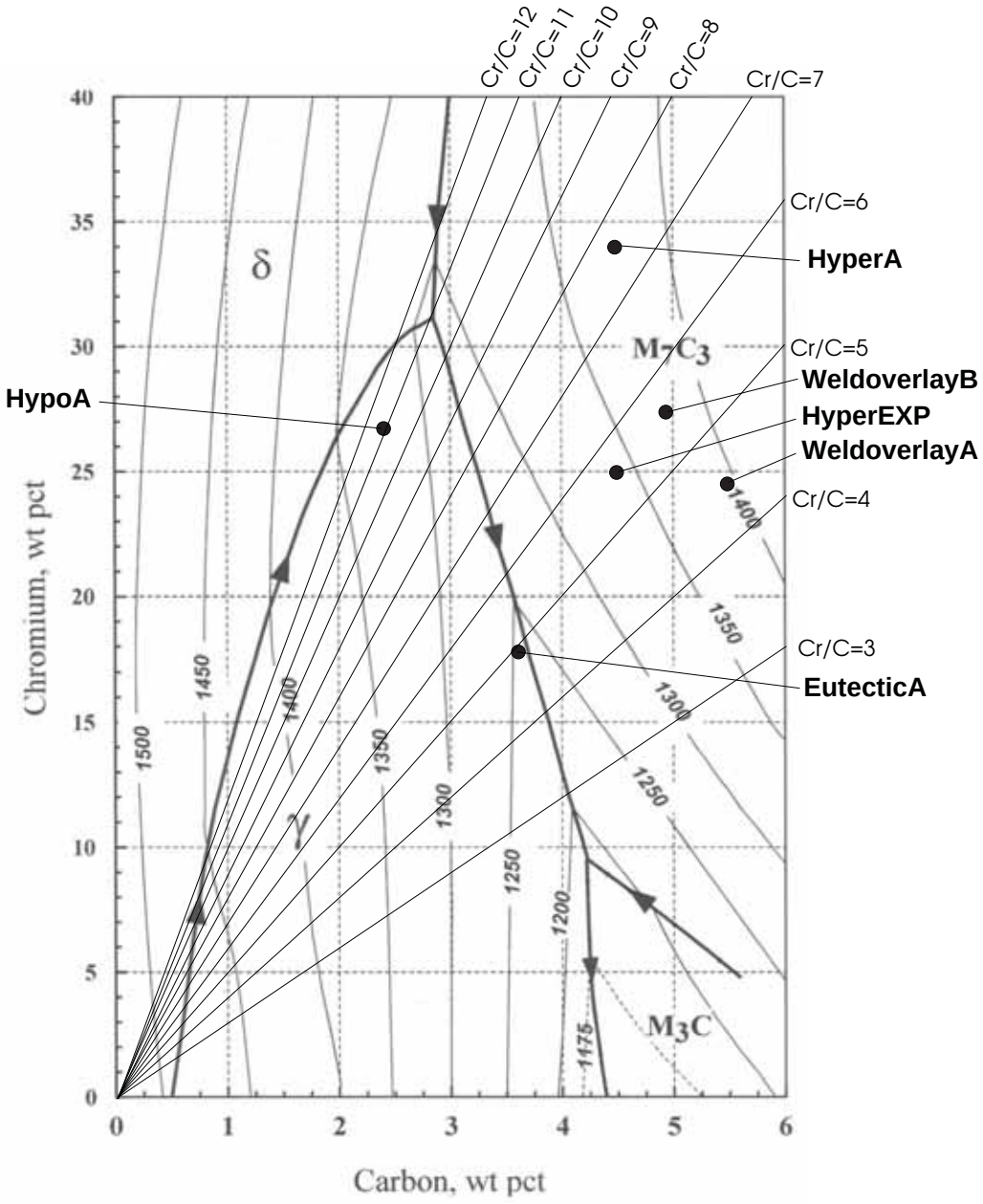

Figure 3.2: Location of the high chromium white iron castings and weld overlays investigated on the metastable Fe-Cr-C liquidus surface (after Thorpe and Chicco (1985)) with plotted lines of constant chromium to carbon ratio (Cr/C).

3.3.1 Heat Treatments to Investigate Microstructural Characteristics

To better understand the role that matrix microstructure has on the corrosion and wear performance of high chromium white irons, two different heat treatments were done on selected casting samples to vary the matrix microstructure. One of the heat treatments was used to

give a microstructure that consisted of secondary carbides and a martensitic matrix. Another heat treatment was used to give a homogeneous matrix of austenite with no secondary carbides. Comparing the test results for the two heat treated conditions allows the influence of matrix microstructure on the corrosion and wear performance to be determined.

3.4 Methodology

Ex-Service Alumina Plant Samples

The wear surface and microstructure of the ex-service alumina plant samples were examined. This involved macroscopic and microscopic wear surface examinations. The purpose of these examinations was to help in the understanding of the wear mechanism in an alumina processing plant environment. Two pump impeller castings and two weld overlayed spool sections were examined. The results of the wear surface examination were compared with laboratory corrosion and erosion-corrosion tests to verify laboratory testing regimes.

Microstructure Characterization

The microstructures of all the high chromium white iron alloys investigated were examined. This involved quantifying the microstructural characteristics outlined in Figure 3.1. The bulk chemical composition, the chemical composition of the carbides and the matrix were determined using appropriate chemical analysis techniques. The carbide morphology, including carbide volume fraction, was determined. The bulk hardness and microhardness of phase constituents were determined. The detailed microstructural examination helped in the understanding of the development of microstructure in high chromium white irons.

Heat Treatments

Heat treatments were done on selected casting samples to alter the matrix phase and create model materials for further corrosion testing. Appropriate heat treatment temperatures were established by a small scale study investigating the response of a selected high chromium white iron casting to a range of heat treatment temperatures (refer Appendix A). Based on this study, two heat treatment temperatures were selected for the heat treatment of all high chromium white irons castings. The first heat treatment temperature (950°C) was used to provide a matrix microstructure of secondary carbides and martensite (destabilization heat treatment). The second heat treatment temperature (1150°C) was used to produce an austenitic matrix with minimal secondary carbides (normalizing heat treatment).

Corrosion Testing

Corrosion testing involved anodic potentiodynamic polarization tests in sodium hydroxide and sodium aluminate solutions. The polarization tests gave an indication of the materials'

performance over a broad range of potentials and identify potentials of significant corrosion phenomena. Tafel corrosion tests were used to more accurately quantify the corrosion current density at the open circuit potential. Constant potential immersion tests, at potentials of significant corrosion phenomena identified from the polarization tests, were done for extended periods of time to better illustrate the effect of corrosion at a particular potential.

The sodium hydroxide solutions, that have a concentration approximately corresponding to the free and total caustic of the sodium aluminate solutions, allowed the effect of aluminate ions in sodium aluminate solutions to be investigated. The tests in sodium hydroxide solution and sodium aluminate solution were done on the HypoA, HyperA and HyperEXP castings. The AS1163: C350LO steel and AISI 420 martensitic stainless steel were also included in this test regime for comparative purposes.

Potentiodynamic polarization tests in sodium aluminate solution for the heat treated high chromium white iron casting samples were done. This allowed the effect of matrix microstructure on corrosion behaviour to be determined.

Erosion-Corrosion Testing

Erosion-corrosion testing involved slurry pot testing in sodium aluminate solution with quartz as the erodent. The proportion and size of the quartz particles was based on average alumina plant data. The weight loss of different high chromium white irons was determined and the wear surfaces compared with the wear surface of the ex-service plant samples. Further erosion-corrosion testing was done in a purpose built electrochemical erosion-corrosion test apparatus that is capable of recording electrochemical corrosion data in erosive environments. This gave an indication of the influence erosion has on corrosion and vice versa.

Part IV

Results

Chapter 4

Investigation of Ex-Service Plant Sample Wear Surfaces

4.1 Samples and Sample Preparation

The industry sourced samples that were provided for examination in this work were in the form of worn alumina plant processing equipment. The samples consisted of high chromium white iron centrifugal slurry pump impeller castings and pipe spools that had been weld overlayed with high chromium white iron onto a low carbon steel substrate. The samples showed varying amounts of wear and had been removed from the alumina processing plant due to premature failure or due to being replaced during regular maintenance intervals. Details of the service environment and location within the alumina process were not necessarily provided.

The ex-service samples were large (castings exceeding 100 kg, spool sections exceeding 40 kg), and therefore required sectioning to a more manageable size for further detailed microscopic examination. Details of the preparation methods and techniques are described in Section 2.2. The investigation of the ex-service plant samples discussed in this section involved a macroscopic wear surface examination and a detailed microscopic examination of the wear surface using scanning electron microscopy. The microstructure of the materials will be discussed in the following section.

4.2 Examination of Castings

4.2.1 Ex-Service Plant Samples

The ex-service high chromium white iron casting samples were in the form of centrifugal pump impellers. The two impellers provided for examination were from different Australian

alumina refineries, Figures 4.1 and 4.2. The impeller casting shown in Figure 4.1 was reported to be of the 27 chromium class (i.e. AS 2027 -2002: Cr 27 LC or Cr 27 HC) and in this thesis is designated HypoA. The second impeller casting, Figure 4.2, was reported to have a hypereutectic microstructure and in this thesis is designated HyperA.

Samples from the impeller castings were plasma cut from vane sections having a thickness varying from approximately 40 mm up to 80 mm. A typical sample location is shown in Figure 4.1.

Figure 4.1: (a) Overview of the ex-service alumina plant slurry pump impeller designated as HypoA. The wedge removed from the casting indicates the sample location. (b) The wear surface of the HypoA impeller casting showing the scalloped wear surface appearance over the entire wear surface.

Figure 4.2: (a) Overview of ex-service alumina plant slurry pump impeller designated as HyperA. (b) The wear surface of the HyperA impeller casting showing the accelerated wear at the periphery of the impeller.

4.2.2 Wear Surface Examination

4.2.2.1 Macroscopic Examination

The wear surface of the impeller castings showed different wear patterns. Most noticeable was the different wear surface appearance of the HypoA casting, Figure 4.1 to the HyperA castings, Figure 4.2. The wear surface of HypoA had a polished shallow scalloped appearance. The degree of wear was more significant towards the periphery of the impeller, characterized by the significant removal of material and deep wear gouges.

The wear surface of HyperA were generally quite smooth, Figure 4.2, free of the scalloped wear surface appearance. However, there were locations of localized wear where significant material had been removed. The wear was more significant towards the periphery of the impeller and on the leading edges of the impeller vanes.

4.2.2.2 Microscopic Examination

Small sections of the ex-service plant samples were examined using a field emission scanning electron microscope (FESEM). The samples were ultrasonically cleaned in acetone for 10 minutes to remove any contaminants and rinsed in ethanol prior to examination in the electron microscope. The wear surface of the HypoA and HyperA impeller castings are shown in Figure 4.3 and 4.4 respectively.

The wear surface of the HypoA sample showed both the eutectic and secondary carbides to be slightly proud of the matrix, Figure 4.3(b). No fracturing of the eutectic carbides was noticed, however, some carbides did show slight rounding at the edges. High magnification examination of the matrix found evidence of gouges and wear tracks that would have been created by particle impingement, Figure 4.3(c).

The wear surface of HyperA showed a greater proportion of carbides than HypoA, Figure 4.4. The carbides were found to be proud of the matrix and had undergone wear, Figure 4.4(b). The wear of the carbides is shown by rounding at the periphery of the carbides. The matrix was found to have significant gouges and wear tracks of varying depths and lengths. It was common to find embedded particles which were found by EDAX to be composed of silicon and oxygen, and likely to be embedded quartz particles, Figure 4.4(c). The apparent carbide size and CVF in the HyperA impeller casting is greater than the HypoA casting. Note the images shown in Figure 4.4 are at 50% higher magnification than those in Figure 4.3.

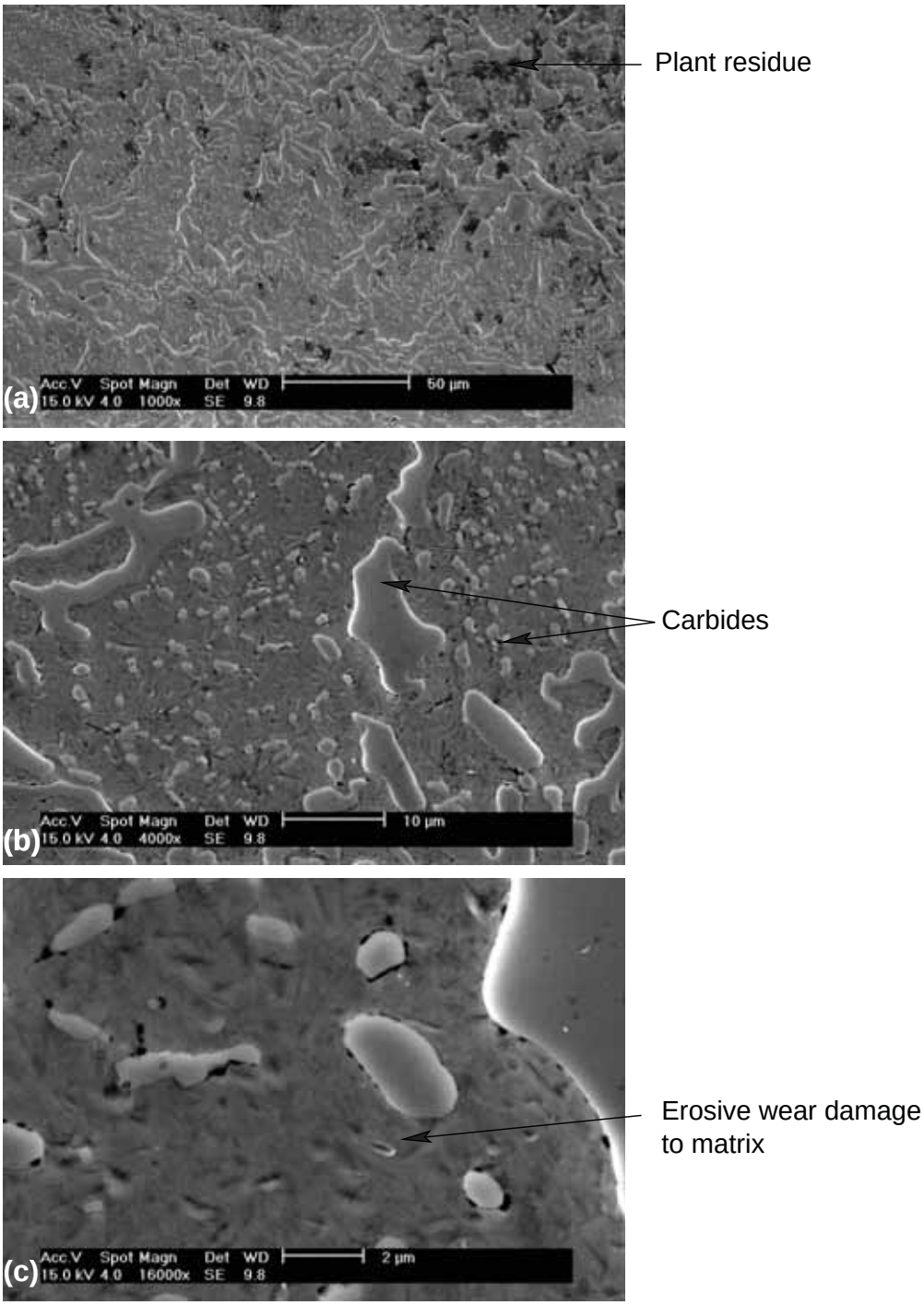

Figure 4.3: Scanning electron micrographs of the wear surface of the HypoA impeller casting. (a) General overview of wear surface. (b) Higher magnification micrograph showing the carbides standing proud above the matrix. (c) Higher magnification micrograph of the matrix showing evidence of gouging and wear tracks due to particle impingement.

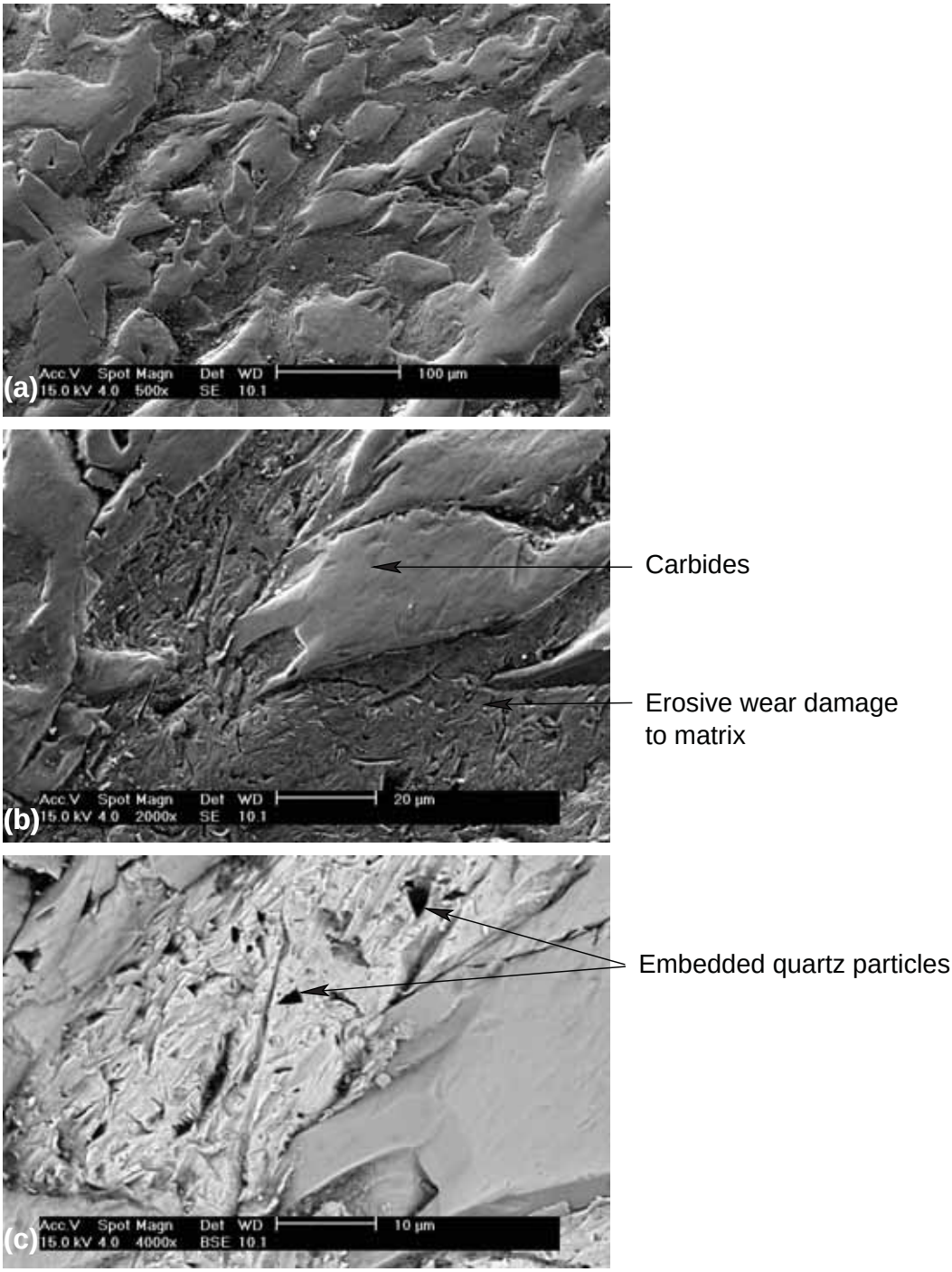

Figure 4.4: Scanning electron micrographs of the wear surface of HyperA impeller casting. (a) General overview of wear surface. (b) Higher magnification image showing the damage to the carbides that are standing proud of the matrix and the significant wear of the matrix. (c) Back scattered electron micrograph also showing the wear damage to the matrix and embedded quartz particles. Note: Images are 50% lower in magnification than the images shown in Figure 4.3.

4.3 Examination of Weld Overlayed Spools

4.3.1 Ex-Service Plant Samples

The two ex-service high chromium white iron weld overlayed spools provided for examination, from different Australian alumina refineries, are shown in Figures 4.5 and 4.6. For the purposes of this thesis, the two weld overlay spools, shown in Figures 4.5 and 4.6 are designated WeldoverlayA and WeldoverlayB respectively. It was reported that both spools had been exposed to an environment ranging in temperature from 75 to 110°C and slurry velocities ranging from 2.5 to 5.0 m/s. The WeldoverlayA spool section, Figure 4.5, was removed from the red-side of the alumina refining process, hence the red appearance of the wear surface. The WeldoverlayB spool section is referred to as a trumpet spool and is used to increase the pipe diameter. The trumpet spool was located down stream of a control valve on the white side of the alumina refining process. The trumpet spool had been in service for approximately 6 months.

Samples from the weld overlays were plasma cut from the sections in Figure 4.5 and 4.6.

Figure 4.5: Overview of the ex-service alumina plant spool section designated as WeldoverlayA. Inside diameter of spool is approximately 725 mm. The rectangular cut out is the sample location.

Figure 4.6: Overview of the ex-service alumina plant trumpet spool designated as WeldoverlayB.

4.3.2 Wear Surface Examination

4.3.2.1 Macroscopic Examination

The ex-service alumina plant samples had severe localized wear damage, which resulted in the gross loss of hardfacing overlay material and, in places, severe erosion of the steel substrate, Figure 4.7. The damage was found to occur adjacent to the flanged connections where the spools were joined to the outlet of pump housing or control valves. It is reported that the flow immediately downstream of pump and control valves is turbulent.

Figure 4.7: Photo of the entry section adjacent the flange of the WeldoverlayB trumpet spool. The image shows the loss of hardfacing material and the wear of the steel substrate.

On a smaller scale, preferential wear of the hardfacing gave the appearance of grooves running along the length of the weld overlayed spool. The grooves ran parallel to the direction of the weld beads (longitudinally along the spool) and are shown in cross section in Figure 4.8, and corresponded to sections of the weld beads having a lighter appearance. The adjacent dark regions, correspond to the overlapping of the deposited weld bead with the previously deposited weld bead, appear to have a lower wear rate than the lighter sections of the weld beads.

Figure 4.8: Cross-section of WeldoverlayA spool showing the preferential wear of the weld beads at specific locations having a lighter appearance. The sample has been etched in acid ferric chloride.

Both of the examined ex-service alumina plant samples contained check cracks over the entire weld overlayed surface, Figures 4.9 and 4.10. The check cracks formed a 5 to 10 mm mesh over the entire overlayed surface and generally extended radially to the substrate-hardfacing interface and often contained slurry constituents within the cracks, Figures 4.11

and 4.12. Preferential wear was often seen at the edges of the check cracks adjacent the wear surface, Figure 4.11.

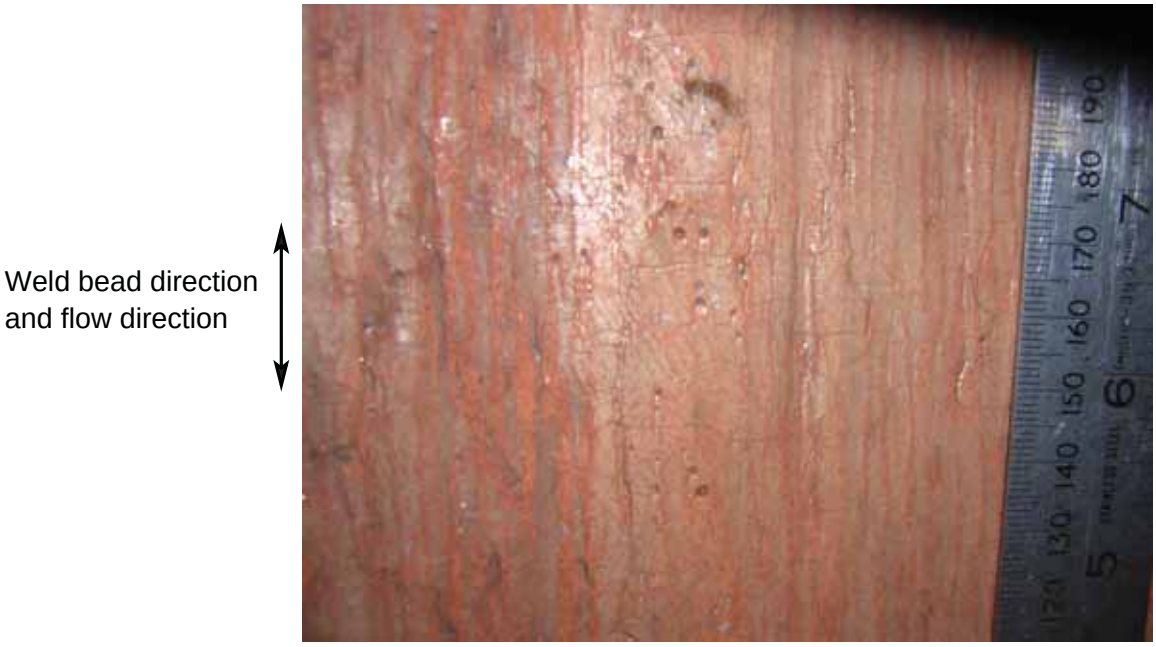

Figure 4.9: Wear surface of WeldoverlayA spool showing the check crack pattern and other wear surface features.

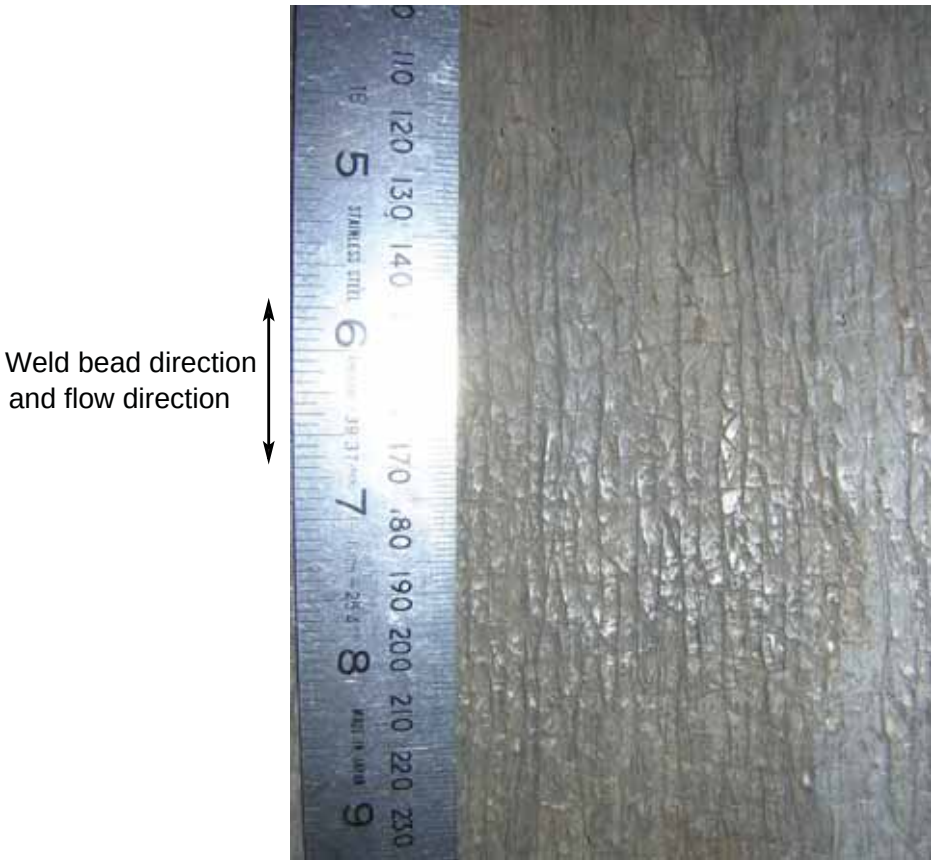

Figure 4.10: Wear surface of WeldoverlayB showing the check crack pattern.

Figure 4.11: Cross section and wear surface of WeldoverlayB showing the check cracks extending to the substrate. Traces of slurry constituents can be seen in the check cracks and preferential wear adjacent the check cracks on the wear surface.

It was common for the radially extending check cracks to branch and crack along the interface between the hardfacing and substrate, Figure 4.12. The majority of weld overlayed samples also contained subsurface pores that were often linked with the check cracks, Figure 4.12. These pores are most likely hydrogen pores due to their smooth, non-oxidized surface, and spherical nature. If the pores were due to particle inclusions it is unlikely that the pores would be spherical and if the pores were due to a readily available gas during welding other than hydrogen, it is likely the surface of the pores would be oxidized.

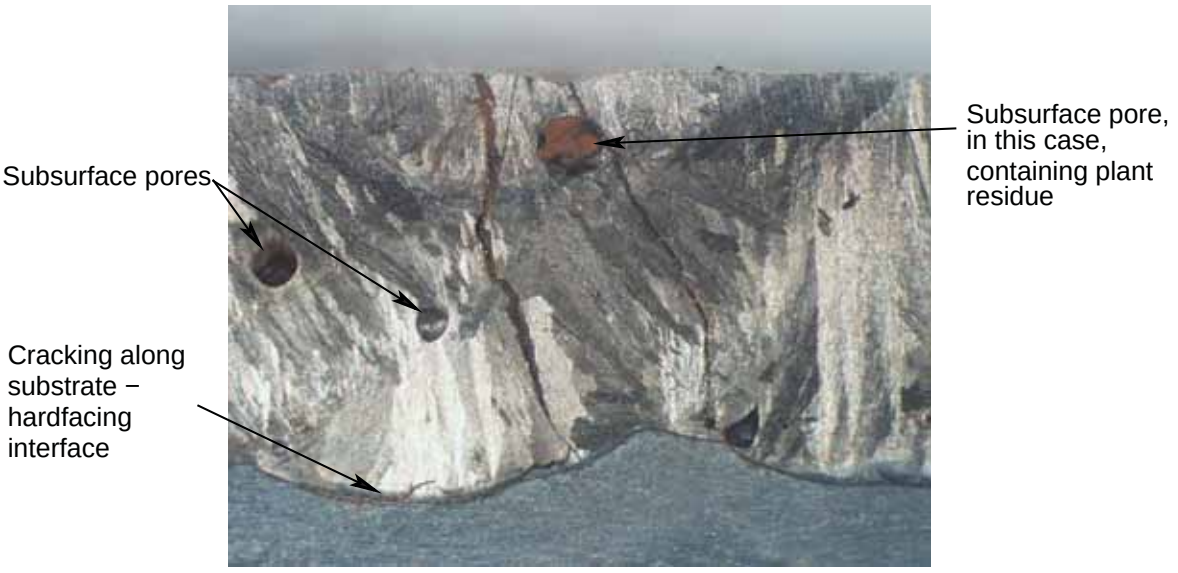

Figure 4.12: Check cracks in a transverse sample that extend to the substrate-hardfacing interface and continues to extend along the substrate-hardfacing interface. Subsurface pores were often found to contain plant residue because they had been intersected by a check crack. The appearance of the overlay is due to the sample being lightly etched acid ferric chloride.

4.3.2.2 Microscopic Examination

Small block samples for examination of the wear surface in a Field Emission Scanning Electron Microscope (FESEM) were sectioned adjacent the samples used for microstructural examination. Initially the plant samples were ultrasonically cleaned in acetone for 20 minutes and the wear surface examined in the scanning electron microscope. The wear surface of the WeldoverlayA was covered with a tightly adherent layer of red plant residue. However, in a few isolated areas the microstructure beneath the layer of plant residue was visible, Figure 4.13. The carbides were found to be standing in relief and the matrix that should be surrounding the carbides was not visible as it was either covered by plant residue or significantly recessed with respect to the carbides. The carbides showed slight rounding at the exposed periphery of the carbides but did not show signs of any significant fracturing or cracking.

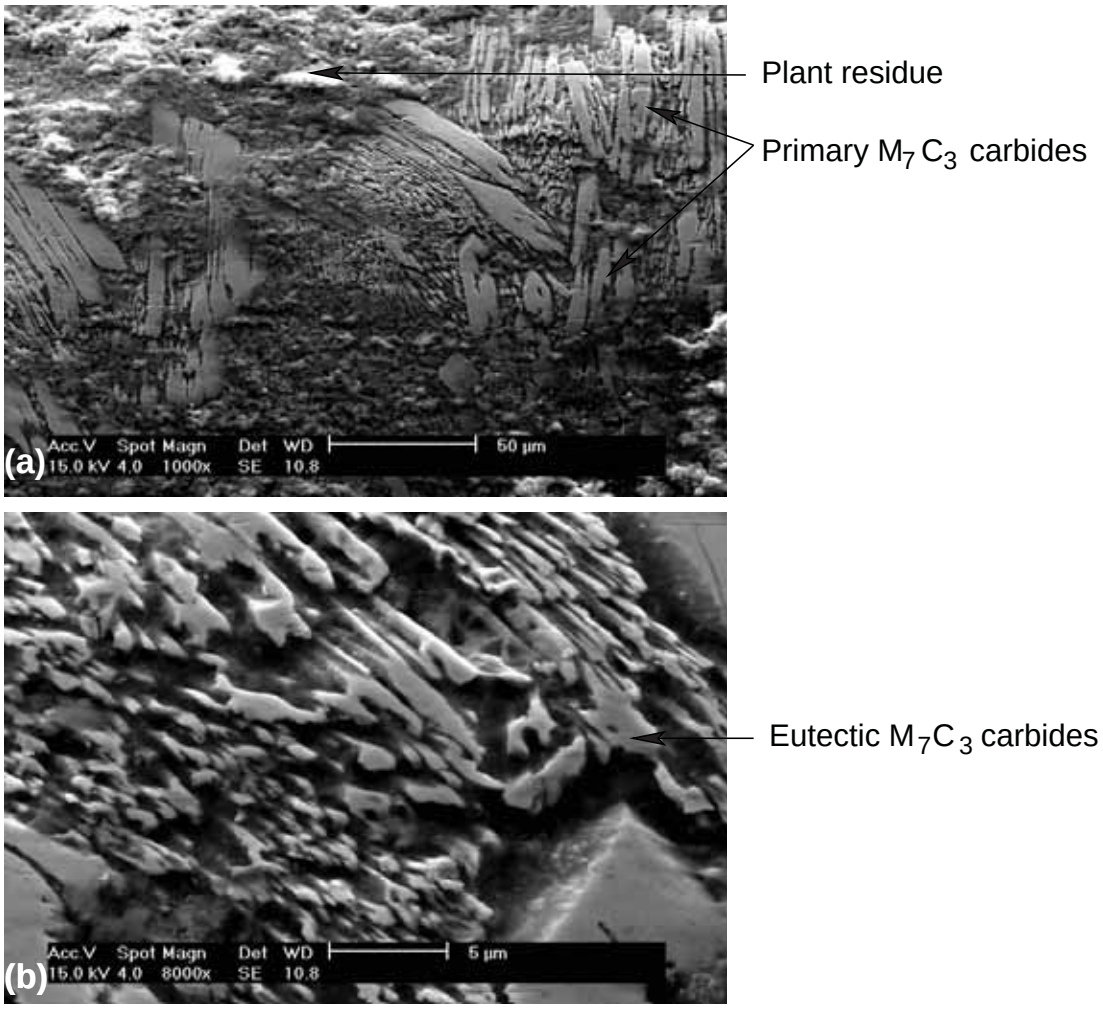

Figure 4.13: Wear surface of WeldoverlayA after being ultrasonically cleaned in acetone for 20 minutes. The carbides are shown to be standing in relief and the matrix could not be detected.

The examination of the wear surface of WeldoverlayB after ultrasonically cleaning in acetone for 20 minutes found that the microstructure was clearly visible and there was only

limited traces of plant residue, Figure 4.14. The larger carbides were found to protrude above the smaller carbides, Figure 4.14(b). The carbides were found to be standing in relief and the matrix could not be seen, Figure 4.14(c). Rounding at the edges of the larger primary carbides could be seen but any significant fracturing or cracking of the carbides was not seen.

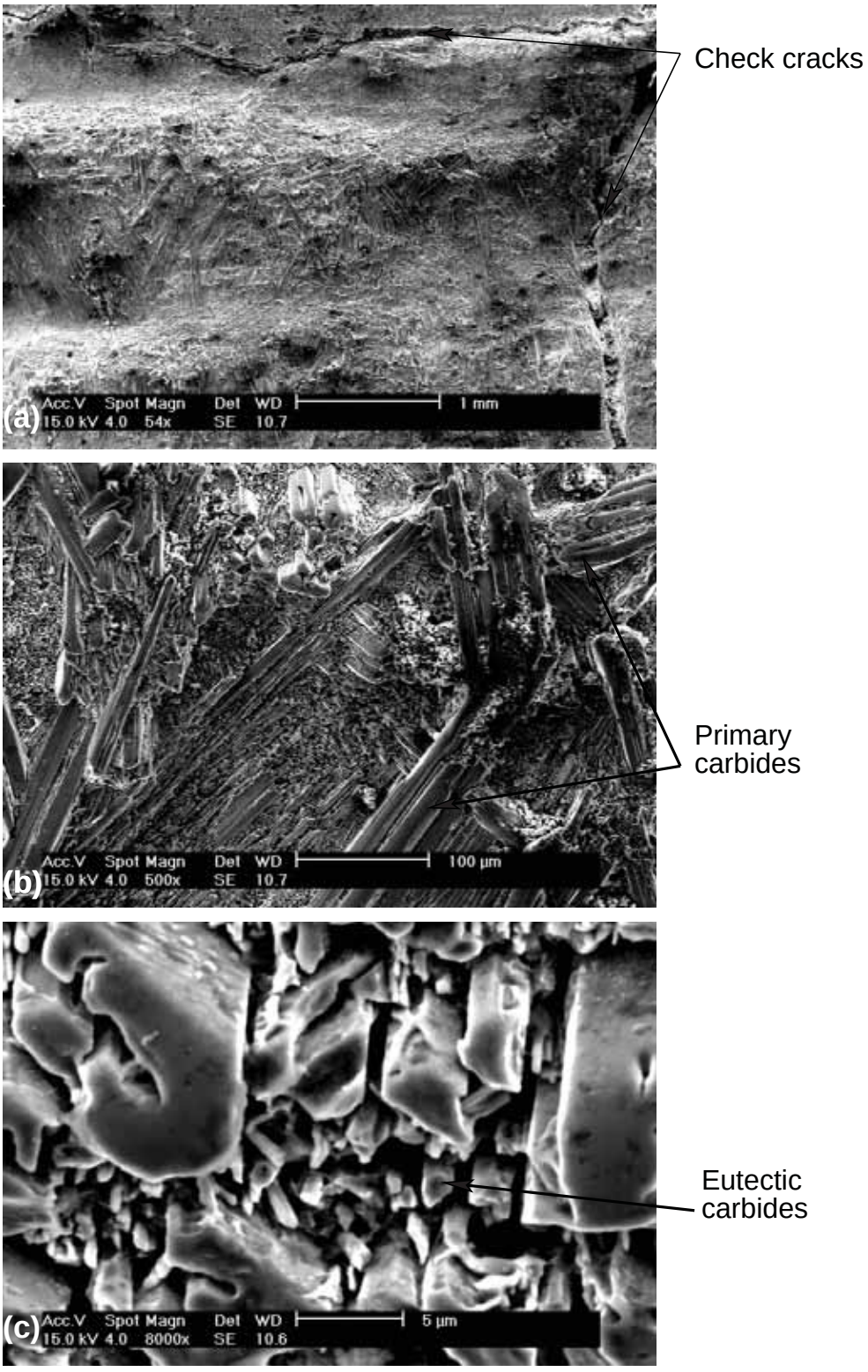

Figure 4.14: Wear surface of WeldoverlayB after being ultrasonically cleaned in acetone for 20 minutes. The carbides are standing in relief and the matrix could not be seen.

In order to better examine the wear surface of the weld overlayed samples, the samples were ultrasonically cleaned in a dilute 2.5% solution of acetic acid for 5 minutes to remove plant residue. To assess the effect ultrasonic cleaning in 2.5% acetic acid solution has on the resulting wear surface appearance, a weld overlay sample (WeldoverlayB) was polished to a 1 micron finish and was ultrasonically immersed in the solution. The before and after surface examination is shown in Figure 4.15. After ultrasonic immersion in the solution, the carbides were not chemically attacked and the matrix had undergone minimal corrosive attack, very similar to the samples being lightly etched.

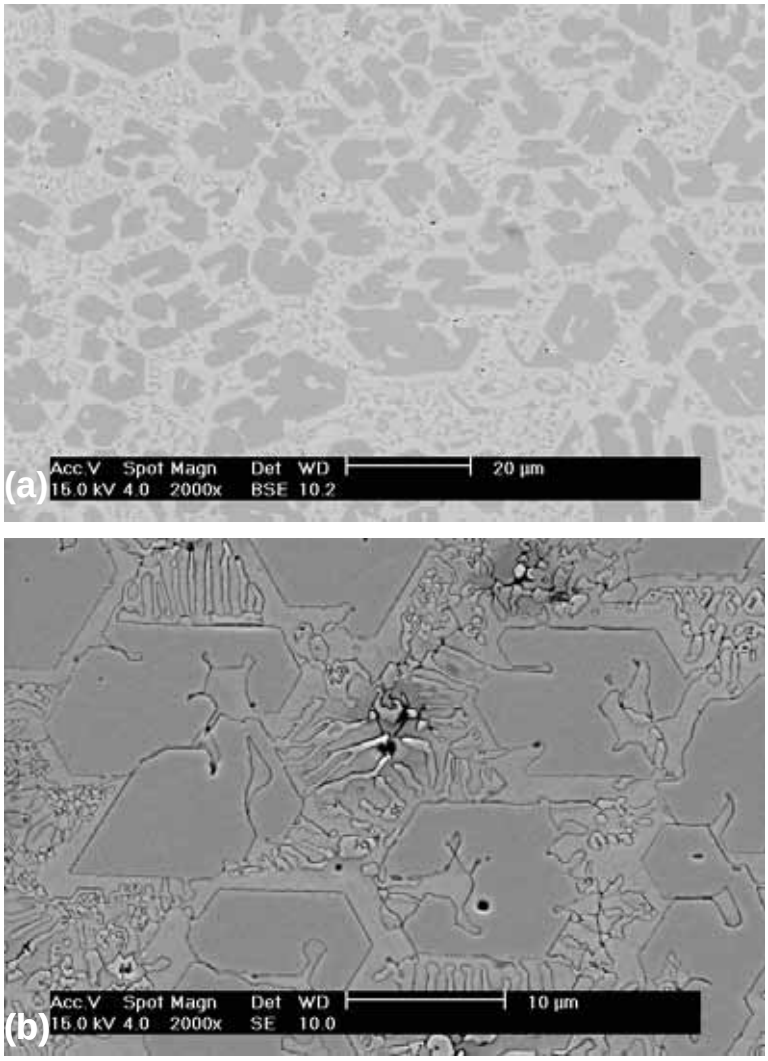

Figure 4.15: (a) Back scattered electron micrograph of the weld overlay sample polished to a 1 micron finish. The surface is flat and the carbides and matrix are planar. (b) Secondary electron micrograph after ultrasonic immersion in 2.5% acetic acid solution for 5 minutes. There is minimal corrosive attack of the matrix.

The wear surface examination of WeldoverlayB after 5 minutes of ultrasonically cleaning in 2.5% acetic acid solution is shown in Figure 4.16. The cleaning process was successful in removing the majority of the plant residue. It can now been seen more clearly that the large carbides protrude above the smaller carbides and the carbides are standing in relief.

The matrix still could not be detected which would indicate that it is significantly below the plane of the carbides.

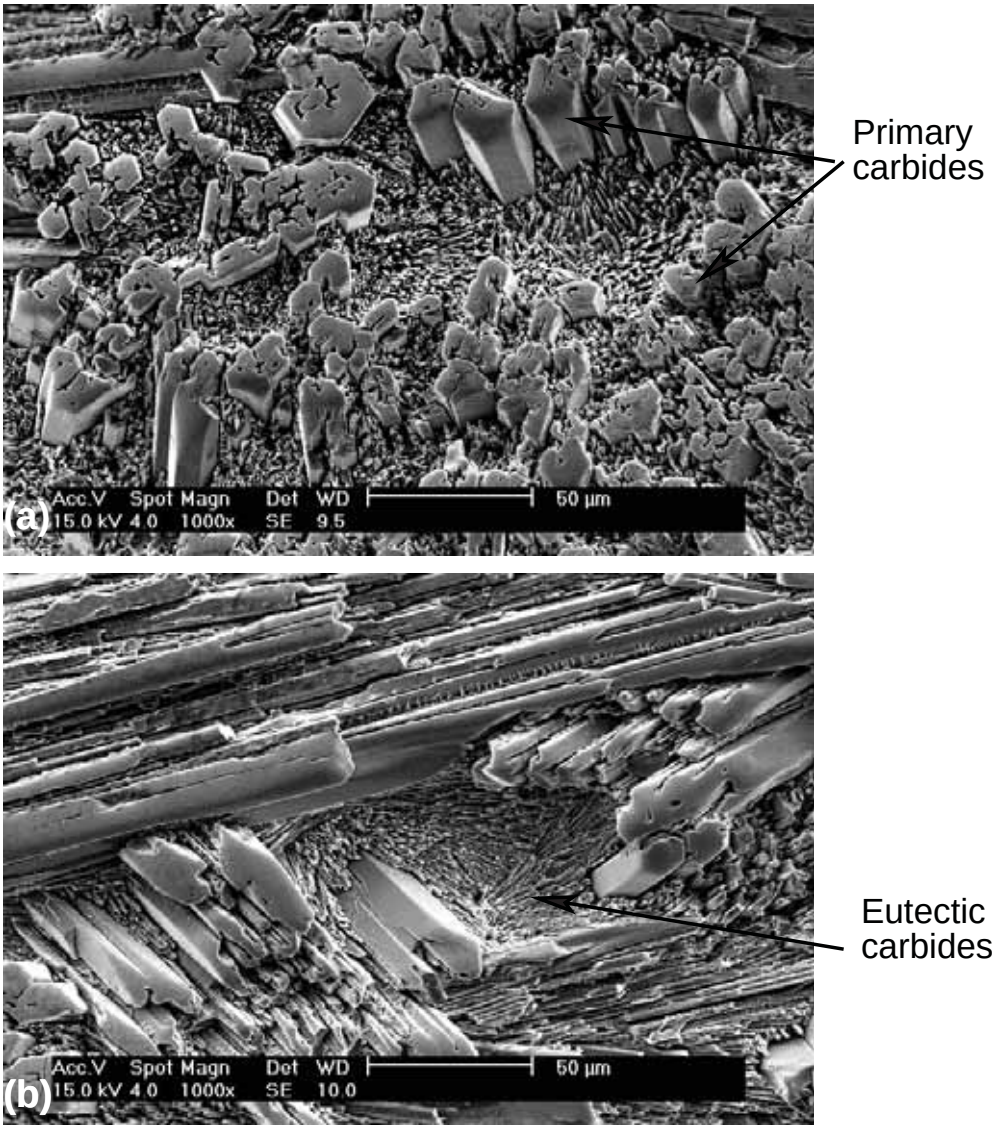

Figure 4.16: Microscopic wear surface examination of WeldoverlayB after being ultrasonically cleaned in acetic acid for 5 minutes.

The wear surface of the WeldoverlayA sample after 5 minutes of ultrasonically cleaning in 2.5% acetic acid solution still had significant amounts of plant residue covering the surface. It was found that 40 minutes of ultrasonic cleaning in the acetic acid solution was required to remove a reasonable portion of the plant residue to allow the examination of the wear surface microstructure, Figure 4.17. Figures 4.17(a) and (b) show that the large carbides are only slightly proud or on the same plane as the smaller carbides. In the majority of places the matrix was not visible, however, in one isolated region traces of the matrix were found, Figure 4.17(c). The matrix has clearly undergone some corrosion or wear and it is unlikely that the cleaning process in dilute acetic acid caused this amount of corrosion.

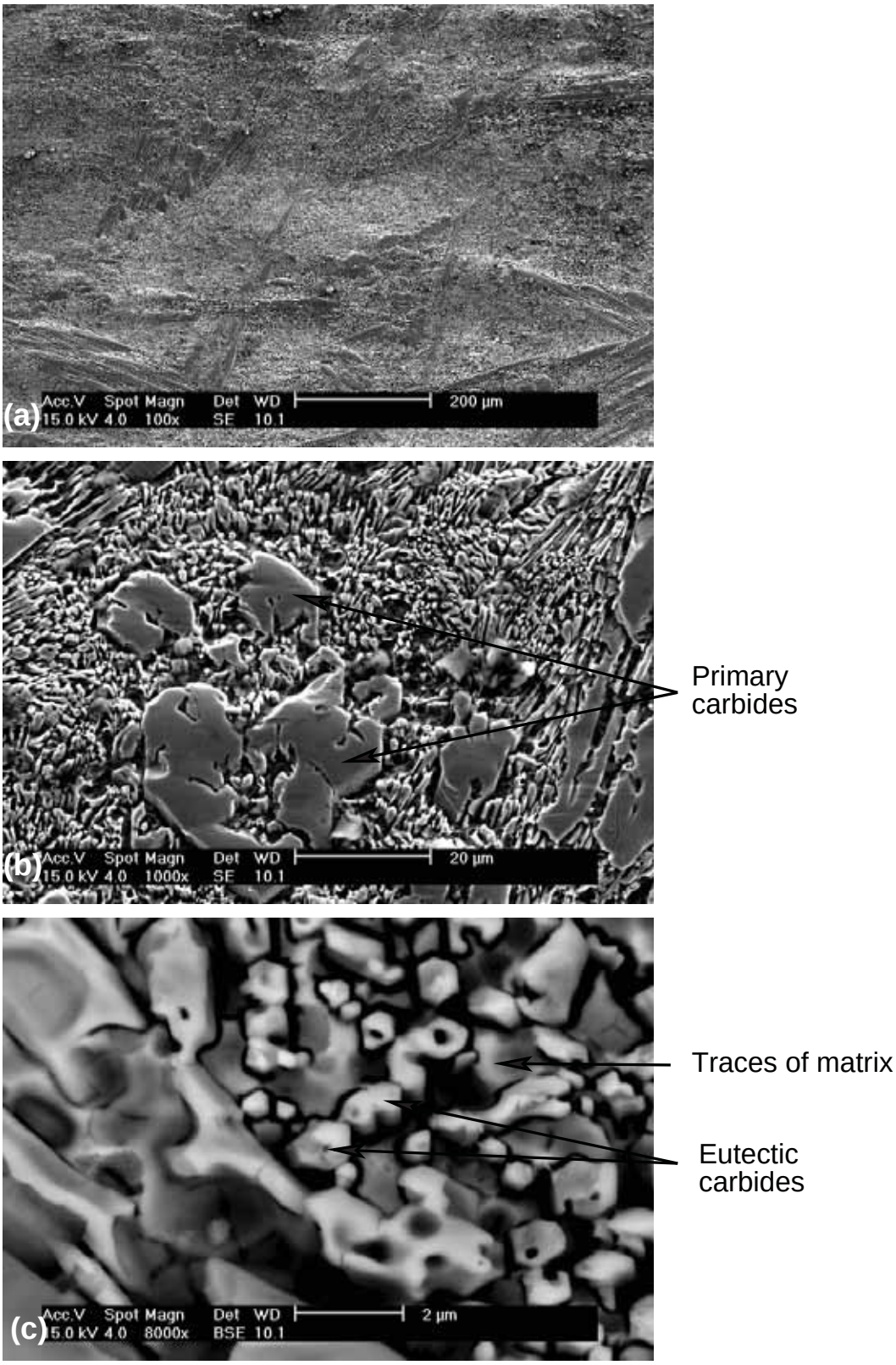

Figure 4.17: Microscopic wear surface examination of WeldoverlayA after being ultrasonically cleaned in 2.5% acetic acid solution for a total of 40 minutes.

4.4 Summary

Two high chromium white iron ex-service alumina plant pump impeller castings and two weld overlayed spools were examined. The pump impellers were of the hypoeutectic heat treated and hypereutectic composition and both the weld overlays were of the hypereutectic composition.

The wear surface of the castings showed varying degrees of erosive wear characterized by the scalloped wear surface appearance. In both cases wear was more significant adjacent trailing edges and towards the periphery of the impeller. The wear surface of the weld overlay spools generally had a grooved wear surface appearance running parallel with the direction of the weld bead that corresponded with overlapping weld beads. One of the weld overlayed spools (WeldoverlayB) had severe localized wear adjacent the flange connection attributed to the flow environment. Both the weld overlays had check cracks in a 5 to 10 mm mesh over the entire surface that would generally extend to the substrate and sometimes continue along the substrate-overlay interface. Plant residue was generally found in the check cracks. Subsurface pores were also found in the weld overlays, the majority of them typical of hydrogen pores, and were often intersected by a check crack.

Microscopic examination of the wear surface of the casting plant samples found that the carbides were proud of the matrix indicating that the matrix wore at a greater rate than the carbides. However, the carbides were found to have worn due to a rounding of the edges. The matrix contained clearly visible gouges and wear tracks characteristic of erosive wear damage, being more significantly pronounced on the HyperA than the HypoA casting. Embedded quartz particles were also found in the matrix of the HyperA sample. The microscopic wear surface of the weld overlay samples was different to the castings. The carbides were standing in relief and the matrix was not readily seen as it was significantly recessed with respect to the carbides. The carbides did not show as much rounding as the casting samples.

Chapter 5

Microstructure

5.1 Introduction

This chapter covers the metallographic examination of the high chromium white iron samples that were used for corrosion and erosion-corrosion testing. These include four different castings and two weld overlay samples. Three of the castings are commercially produced, two of which were sectioned from ex-service alumina plant slurry pump impellers (HypoA and HyperA) and the third from an as-cast wear block (EutecticA). The fourth casting is an experimental hypereutectic composition having improved fracture toughness which was developed at the University of Adelaide (HyperEXP). The two weld overlay samples were sectioned from ex-service alumina plant pipe spools (WeldoverlayA and WeldoverlayB). For the weld overlay sample, it was found necessary to examine a number of different orientations to capture the vast variations in microstructure that these alloys exhibit.

This chapter also covers the metallographic examination of two different heat treatments done on the four different casting samples. The purpose of undertaking the heat treatments was to alter the matrix microstructure to enable the influence of microstructural variables, such as the presence of secondary carbides and different phases, on the corrosion and erosion-corrosion behaviour to be more precisely determined..

5.2 Metallographic Examination

5.2.1 Samples As-Received

The samples in the as-received condition include the ex-service alumina plant pump impeller castings, HypoA and HyperA, and the weld overlayed spool samples, WeldoverlayA and WeldoverlayB. Also included is this section are the EutecticA and HyperEXP castings which are both in the as-cast condition.

5.2.1.1 HypoA

HypoA is a commercially produced casting that was in the form of a slurry pump impeller which had previously been used for the transfer of slurries in an alumina processing plant.

The microstructure of the HypoA impeller casting is shown in Figure 5.1. The microstructure shows that the casting is of the hypoeutectic composition due to the small amount of eutectic M_7C_3 carbides and the presence of primary austenite dendrites. The casting has been heat treated prior to service as the primary austenite dendrites and the eutectic austenite in the matrix have been destabilized during a processing heat treatment to form secondary carbides and martensite. The specific destabilization heat treatment conditions, temperature and time, are not known for this sample.

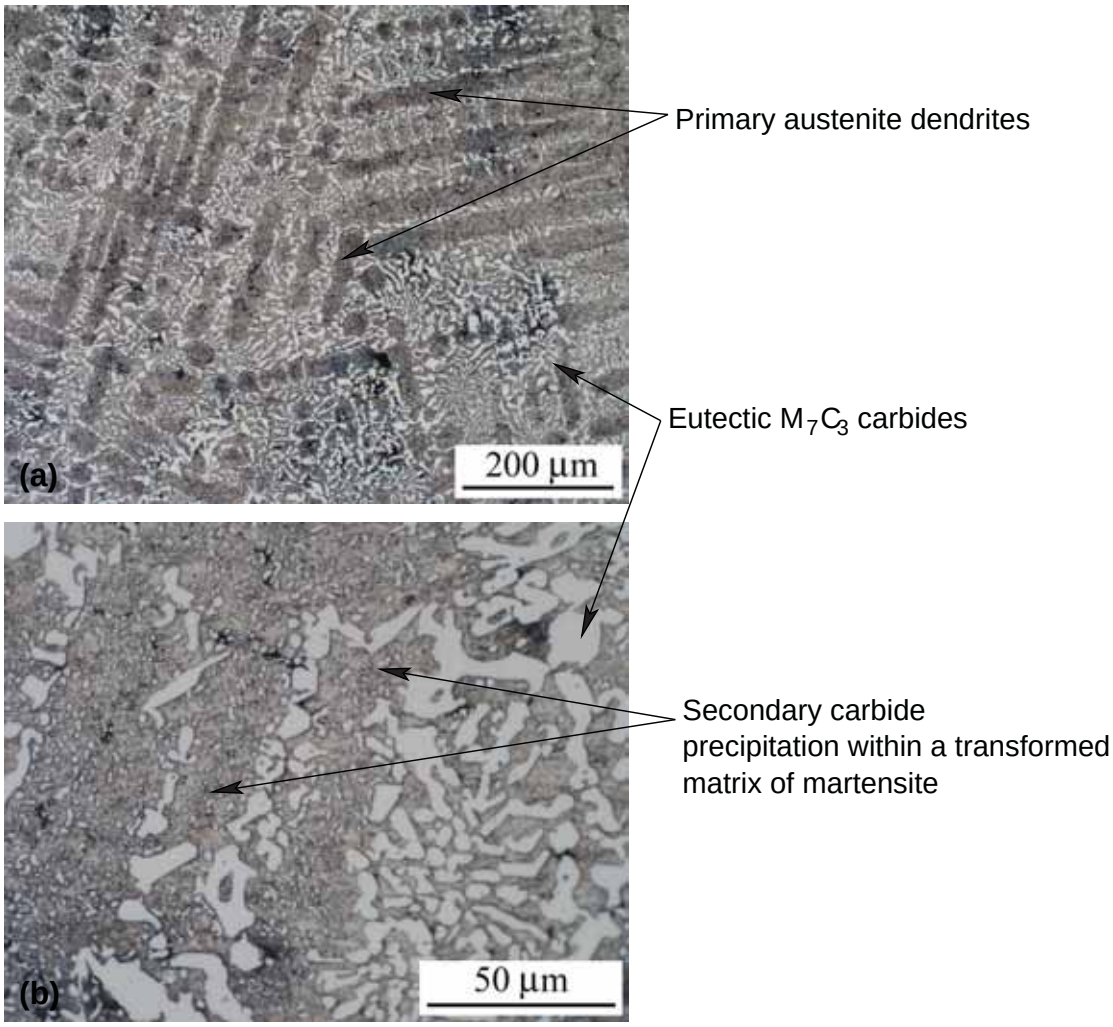

Figure 5.1: Optical micrographs of the HypoA casting in the as-received condition. (a) General low magnification micrograph showing the austenite dendrites and eutectic carbides. (b) Higher magnification micrograph showing the secondary carbides within the transformed austenite dendrites.

Examination of the etched sample in an electron microscope gives a more detailed view of the secondary carbides and matrix microstructure, Figure 5.2. The back scattered electron

micrograph, Figure 5.2(b) shows that the eutectic M_7C_3 carbides do not have a shell or duplex carbide morphology and are of the M_7C_3 carbide type only. The eutectic M_7C_3 carbides are more blade like in shape and can be up to approximately 10μm in length. Figure 5.2(c) show a high magnification secondary electron image of the transformed matrix. The secondary carbides, which are likely to be precipitated $M_{23}C_6$ carbides or M_7C_3 carbides range in size from approximately 0.5 to 1.5μm. The uneven appearance of the etched matrix can be attributed to the presence of a large proportion of martensite and possibly some retained austenite.

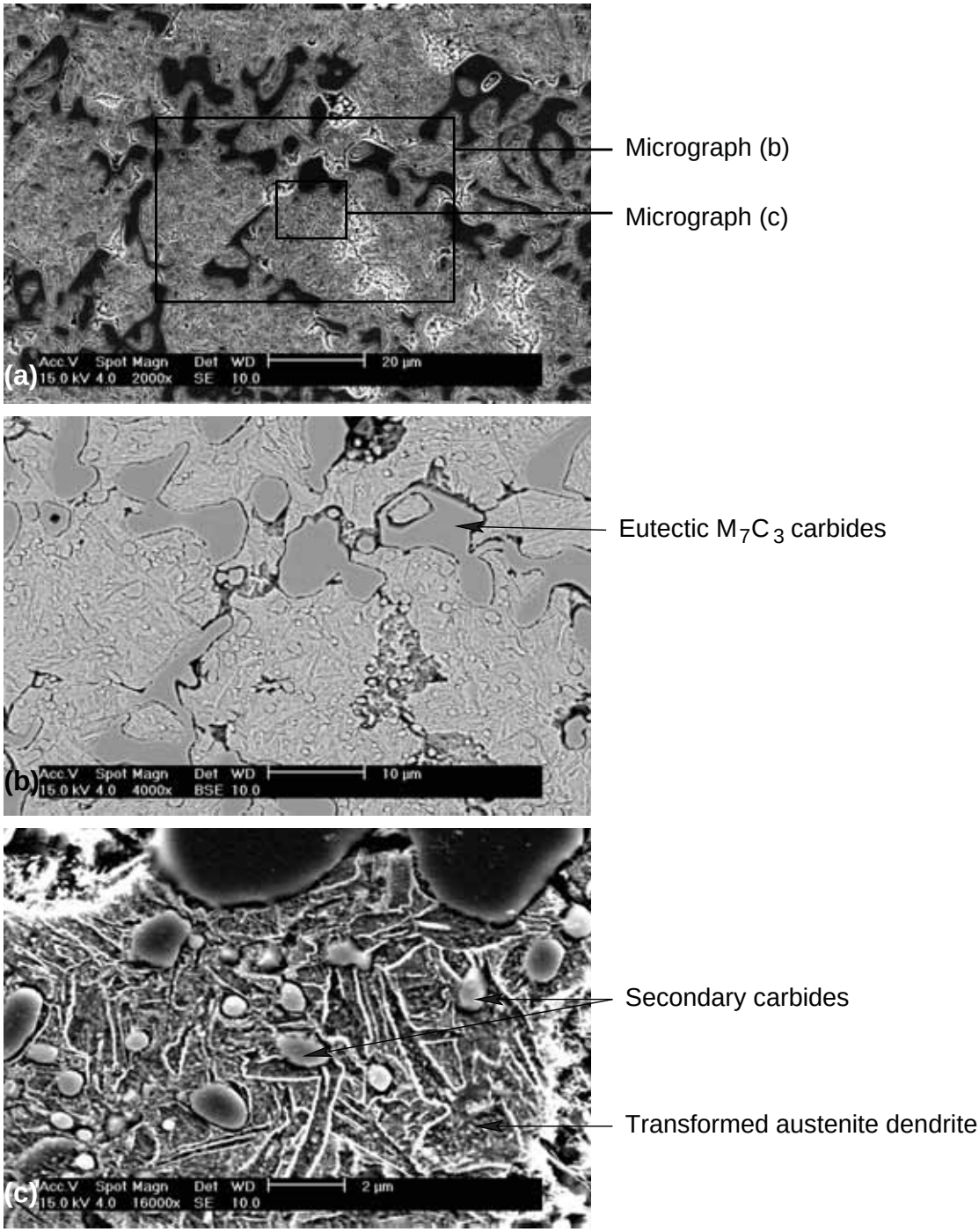

Figure 5.2: Electron micrographs of the HypoA casting in the as-received condition. (a) Secondary electron micrograph showing higher magnification analysis location. (b) Backscattered electron micrograph showing the eutectic M_7C_3 carbides do not have a duplex morphology. (c) High magnification secondary electron micrograph of a transformed austenite dendrite showing the morphology of the secondary carbides.

The bulk chemical composition and the chemical microanalysis results of the eutectic M_7C_3 carbides and matrix are given in Table 5.1. The bulk chemical composition of this alloy having 27% chromium and 2.4% carbon, chromium to carbon ratio of 11.1, fall within the AS2027/Cr 27 LC classification.

Table 5.1: Bulk chemical composition, chemical composition of the eutectic carbides, matrix and CVF for the HypoA casting in the as-received condition.

HypoA	Chemical Composition wt%							CVF*
	C	Si	Cr	Mn	Fe	Ni	Mo	
Bulk	2.40	0.97	26.60	0.69	69.20	0.06	0.02	
Eutectic M_7C_3 carbides	8.88 ± 0.50	0.00 ± 0.00	62.49 ± 0.35	0.49 ± 0.03	27.65 ± 0.25	0.01 ± 0.01	0.01 ± 0.03	25.8 ± 1.1
Matrix	0.40 ± 0.10	1.26 ± 0.02	12.57 ± 0.81	0.71 ± 0.01	85.59 ± 1.15	0.19 ± 0.02	0.05 ± 0.04	
* Carbide volume fraction of eutectic M_7C_3 carbides								

The bulk hardness of the alloy and microhardness of the carbide and matrix phase is given in Table 5.2. The bulk hardness was found to be about 623 HV. Typical microhardness indents in the matrix, using 100 and 300g loads, and in the carbides, using 50g loads, are shown in Figure 5.3. The matrix microhardness of 537 HV represent the combined hardness of the transformed austenite and secondary carbides. The hardness of the eutectic M_7C_3 carbides was found to be 1688 HV.

Table 5.2: Bulk hardness and microhardness test results for the HypoA casting in the as-received (destabilized) condition.

HypoA		
Bulk hardness (HV_{30})	Microhardness Matrix ($HV_{0.3\ \&\ 0.1}$)	Microhardness Carbides ($HV_{0.05}$)
623±4	537±19	1688±149

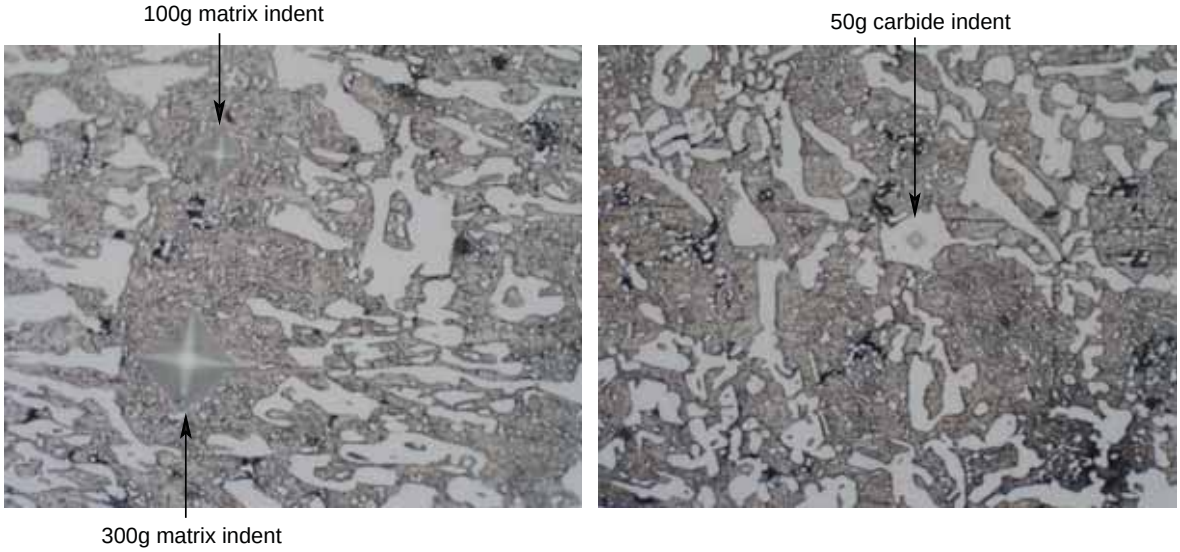

Figure 5.3: Optical micrographs of the microhardness indents in the matrix and eutectic M_7C_3 carbide for the HypoA casting in the as-received (destabilized) condition.

5.2.1.2 EutecticA

The EutecticA alloy is a commercially produced casting sourced from a local manufacturer. The casting was supplied in the as-cast condition and in the form of a small wear block.

The as-cast microstructure of the EutecticA casting is shown in Figure 5.4. There is no evidence of primary M_7C_3 carbides which would be in the form of large hexagonal rods, and there is no evidence of primary austenite dendrites as seen in the HypoA sample (Figure 5.1(a)). Therefore the alloy is of the eutectic composition and the carbides are of the eutectic M_7C_3 type. The eutectic M_7C_3 carbides are generally of a blade like morphology. From the optical micrograph, Figure 5.4(b), the matrix is found to contain regions of pearlite in a predominantly austenitic matrix. The optical micrograph also shows evidence of another phase surrounding the carbides and is likely to be martensite. The electron micrographs of the etched sample, Figure 5.5, better illustrate the variations in matrix microstructure. In the back scattered electron micrograph, Figure 5.5(a), a region of pearlite is clearly visible as well as the variations in matrix phases. Figure 5.5(b) shows that the matrix contains some secondary carbides and that one of the matrix phases, likely to be martensite, is more likely to surround the carbides.

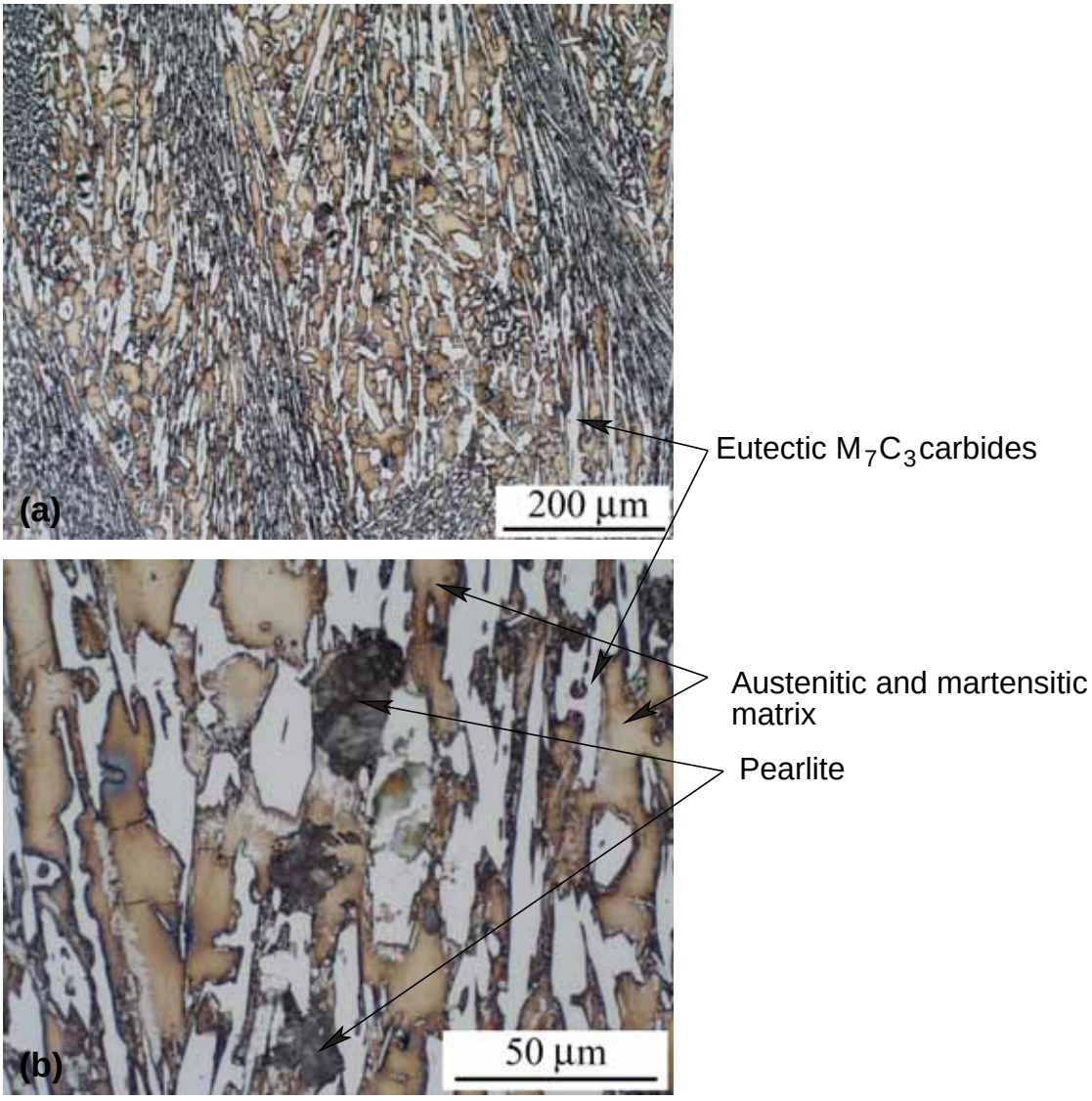

Figure 5.4: Optical micrographs of the EutecticA casting in the as-cast condition. (a) Micrograph showing the high proportion of eutectic M_7C_3 carbides. (b) Higher magnification micrograph showing the matrix microstructure is composed of austenite, martensite and pearlite.

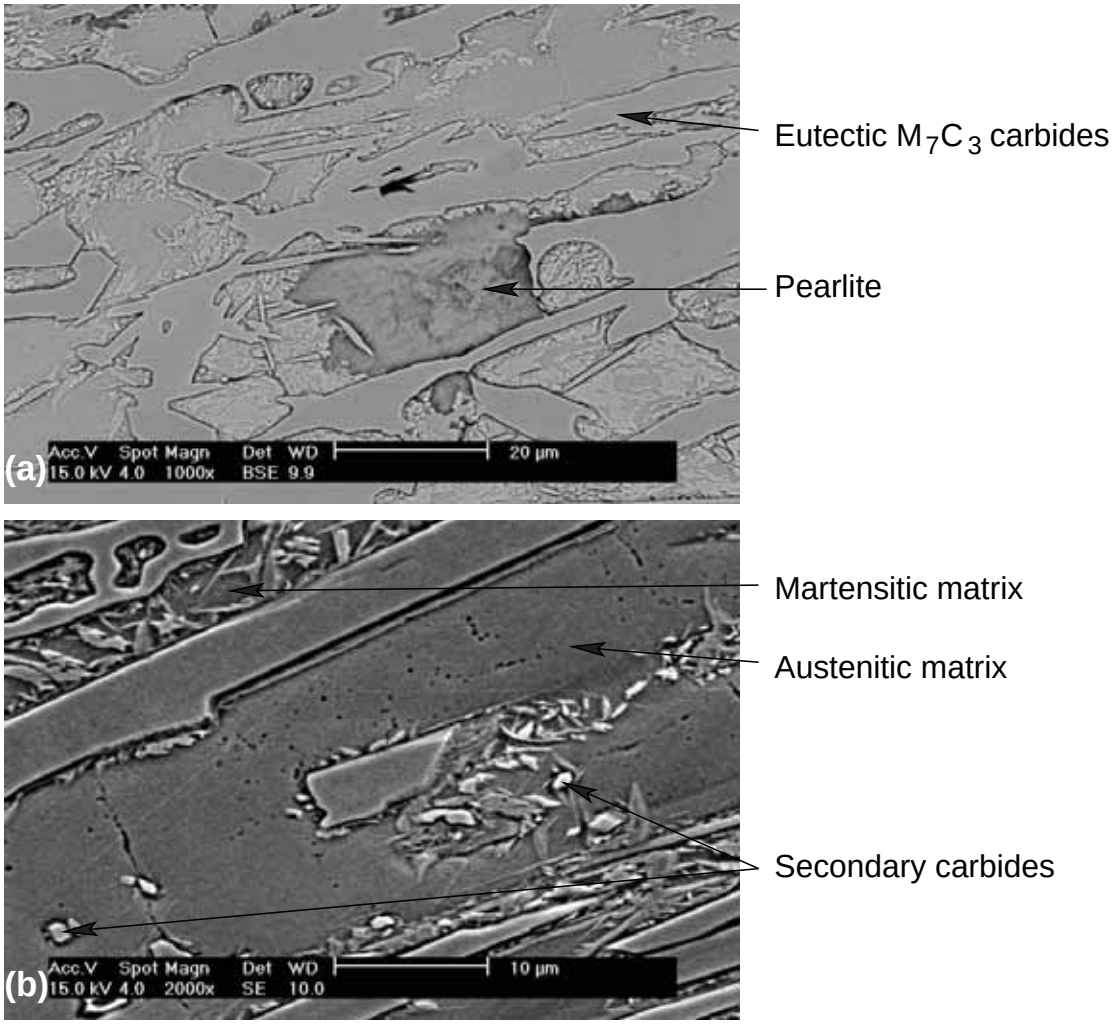

Figure 5.5: Electron micrographs of the EutecticA casting in the as-cast condition. (a) Back scattered electron micrograph showing areas of pearlite amongst other matrix phases. (b) Secondary electron micrograph showing the presence of what is likely to be martensite adjacent the carbides, austenite and secondary carbides.

The bulk chemical composition and the CVF of the EutecticA alloy is reported in Table 5.3. The chemical composition of the carbides and matrix were not measured for this sample in the as-cast condition as the casting contained pearlite and therefore would not be used in service. The alloy has a carbon content of 3.6% carbon, 18% chromium (chromium to carbon ratio of 4.7) and 1.4% molybdenum. The chemical composition of this alloy most closely corresponds to an AS2027/CrMo 15 3 (ASTM 15%Cr-Mo) high chromium white iron. The manufacturer has deliberately targeted the upper composition limits of the ASTM 15% Cr-Mo designation. The CVF fraction of the eutectic carbides was found to be approximately 39% and the bulk hardness was measured to be 694 ± 32 HV_{30}.

Table 5.3: Bulk chemical composition and CVF for the EutecticA casting in the as-cast condition.

EutecticA	Chemical Composition wt%							CVF*
	C	Si	Cr	Mn	Fe	Ni	Mo	
Bulk	3.60	0.53	17.80	0.65	75.90	0.10	1.35	38.6 ± 3.1
* Carbide volume fraction of eutectic M_7C_3 carbides								

5.2.1.3 HyperA

HyperA is a commercially produced casting that was in the form of a slurry pump impeller which had previously been used for the transfer of slurries in an alumina processing plant. The casting was reported to be in the as-cast condition.

The as-cast microstructure of HyperA casting is shown in Figure 5.6. The microstructure consists of large proportion of large carbides, some of which are over 50μm in cross section. Depending on the plane of polish, many of the large carbides have a hexagonal morphology and are characteristic of primary M_7C_3 carbides. The presence of the primary carbides indicates the alloy is of the hypereutectic composition. However, this alloy does not have the typical eutectic microstructure of hypereutectic castings expected from equilibrium cooling conditions (see Figure 1.5(b)) of smaller and numerous eutectic M_7C_3 carbides . There are a very limited number of what could typically be classified as eutectic M_7C_3 carbides. It is suspected that the HyperA casting may have undergone a non conventional processing route, such as inoculation, to give this microstructure. Unfortunately the processing route of this castings is not known.

The matrix of the HyperA casting is mainly austenite but also contains a band of martensite surrounding the carbides with martensite laths extending into the austenitic matrix, Figure 5.6(b). The matrix also contains dark clusters centrally located within the austenite matrix that are separated from the primary and eutectic M_7C_3 carbides which are small precipitated carbides.

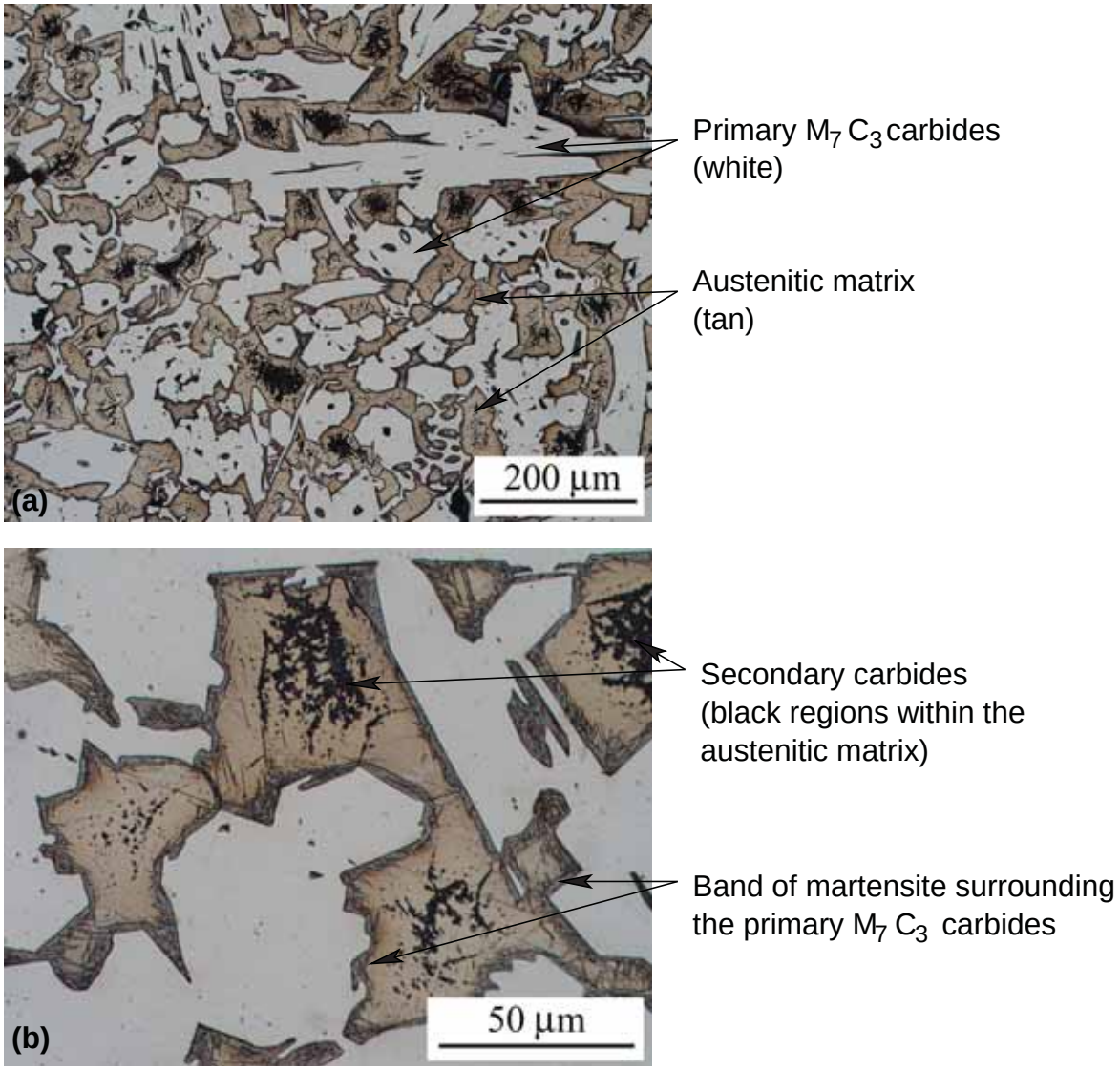

Figure 5.6: Optical micrographs of the HyperA casting in the as-cast condition. (a) Low magnification micrograph showing the high volume fraction of carbides. (b) Higher magnification micrograph showing the band of martensite surrounding the carbides and the dark clusters of secondary carbides in an austenitic matrix.

Examination of the etched sample in an electron microscope showed that the primary and eutectic M_7C_3 carbides do not have a shell or duplex morphology, Figure 5.7(a). The secondary electron image, Figure 5.7(b) further illustrated the fine nature of the dark clusters seen in the optical micrographs, centrally located within the the austenitic matrix and separated from the primary and eutectic M_7C_3 carbides. At higher magnification of 16,000 times that the dark clusters can be resolved, Figure 5.7(c). It is found that the dark clusters are carbides, less than 1μm in size, and have a fibrous like morphology. Based on the fine nature of the carbides and the high chromium composition of this alloy, it is likely that the small carbides are of the $M_{23}C_6$ type and would have precipitated during the cooling after solidification of the austenite.

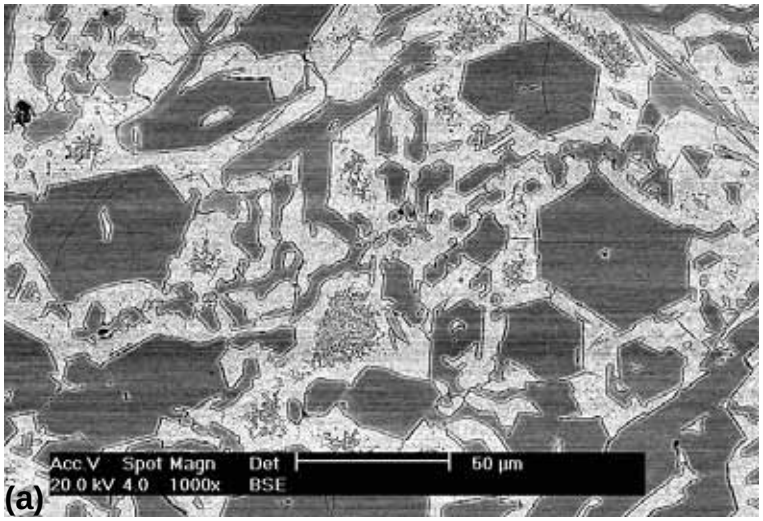

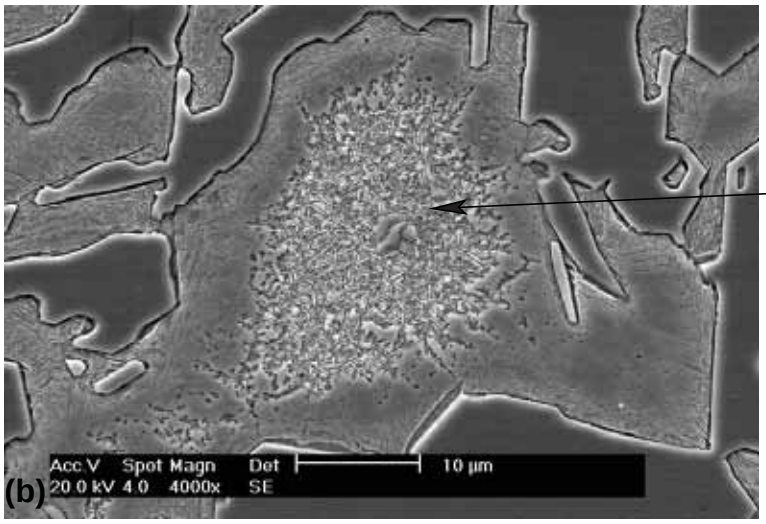

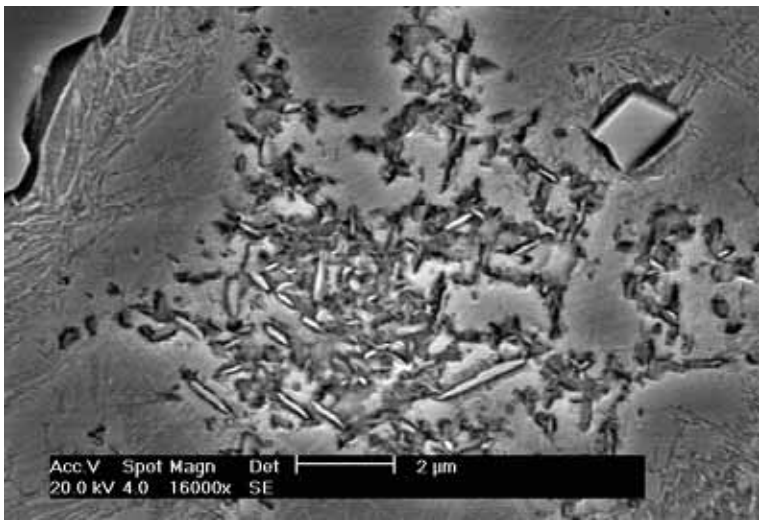

Figure 5.7: Electron micrographs of the HyperA casting in the as-cast condition. (a) Back scattered electron micrograph showing that the carbides do not have a duplex morphology. (b) Secondary electron micrograph showing the secondary carbides precipitates within the matrix. (c) Higher magnification secondary electron micrograph showing the morphology of the secondary carbides.

The bulk chemical composition and the chemical microanalysis of the primary and eutectic

M_7C_3 carbides and the matrix are given in Table 5.4. The bulk composition of this alloy having 34% chromium and 4.5% carbon, chromium to carbon ratio of 7.6, falls within the AS2027/Cr 35 classification. The primary M_7C_3 carbides contained approximately 57% chromium, 1.6% manganese, 0.6% molybdenum and negligible nickel and silicon. The eutectic M_7C_3 carbides contained approximately 4.4% less chromium and slightly more manganese and molybdenum. The matrix contained approximately 0.75% carbon, 10.6% chromium, 1.4% molybdenum and the manganese composition was similar to the eutectic carbides at 2.2%. The elements that were not contained within the carbides, namely silicon and nickel, were found in increased concentration within the matrix of approximately 0.9% and 0.6% respectively. The carbide volume fraction of the primary and eutectic carbides for the hypereutectic alloy was measured to be about 52%.

Table 5.4: Bulk chemical composition, chemical composition of the carbides, matrix and CVF for the HyperA casting in the as-cast condition.

HyperA	Chemical Composition wt%							CVF*
	C	Si	Cr	Mn	Fe	Ni	Mo	
Bulk	4.50	0.49	34.00	1.90	57.70	0.12	0.95	51.9 ± 2.5
Primary M_7C_3 carbides	8.83 ± 0.27	0.00 ± 0.00	57.36 ± 0.79	1.59 ± 0.06	31.46 ± 0.69	0.05 ± 0.02	0.61 ± 0.04	
Eutectic M_7C_3 carbides	8.69 ± 0.20	0.01 ± 0.01	52.94 ± 1.76	2.31 ± 0.15	33.80 ± 0.97	0.05 ± 0.03	1.14 ± 0.30	
Matrix	0.78 ± 0.08	0.90 ± 0.02	10.62 ± 0.62	2.23 ± 0.10	83.79 ± 1.08	0.60 ± 0.03	1.37 ± 0.37	
* Carbide volume fraction of primary and eutectic M_7C_3 carbides								

The bulk hardness of the alloy and microhardness of the carbides and matrix phases are given in Table 5.5. The bulk hardness of the alloy was measured to be about 680 HV. The matrix microhardness of about 511 HV represents the combined hardness of the austenite, martensite and secondary carbide matrix phases. The hardness of the primary M_7C_3 carbides was found to be about 1765 HV.

Table 5.5: Bulk hardness and microhardness test results for the HyperA casting in the as-cast condition.

HyperA		
Bulk hardness (HV_{30})	Microhardness Matrix ($HV_{0.3\ \&\ 0.1}$)	Microhardness Carbides ($HV_{0.05}$)
681±20	511±33	1765±104

5.2.1.4 HyperEXP

HyperEXP is an experimental casting composition that has improved toughness. The alloy was cast as a block having dimension of approximately 90x90x50 mm.

The microstructure of the alloy in the as-cast condition is shown in Figure 5.8. The microstructure consists of large primary M_7C_3 carbides and smaller eutectic M_7C_3 carbides and is of the hypereutectic composition. The matrix of this alloy is entirely composed of

eutectic austenite as it shows no attraction to a strong magnet. There is some evidence of secondary carbide precipitation within the eutectic austenite, Figure 5.8(b).

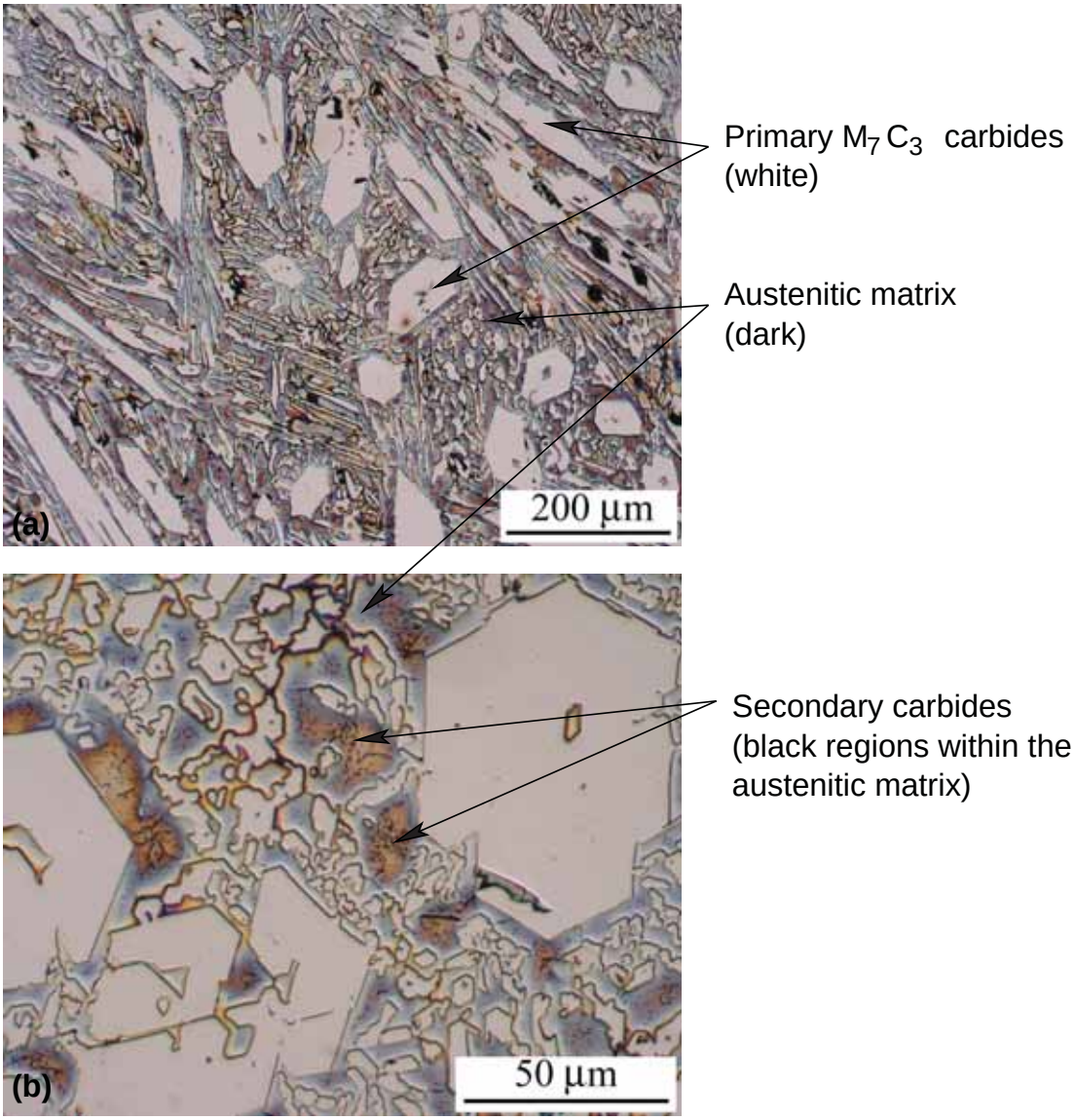

Figure 5.8: Optical micrographs of the HyperEXP casting in the as-cast condition. (a) Low magnification micrograph showing the distribution of the large primary and smaller eutectic M_7C_3 carbides. (b) Higher magnification micrograph better showing the eutectic M_7C_3 carbides and secondary carbides.

Examination of the etched sample in a electron microscope shows that the primary and eutectic M_7C_3 carbides do not have a shell or duplex morphology, Figure 5.9(a). It should be noted that the plane of polish of the large primary M_7C_3 carbides in this figure is parallel with the long axis of the carbide rod, compared to the hexagonal shape when the carbides are polished perpendicular to the long axis of the carbide shown in Figure 5.8(b). The higher magnification secondary electron image, Figure 5.9(b), shows the distribution of the secondary carbides within the austenitic matrix, the morphology of which could not be resolved. It is likely that the small carbides are of the $M_{23}C_6$ type and would have precipitated during the

cooling after solidification of the austenite.

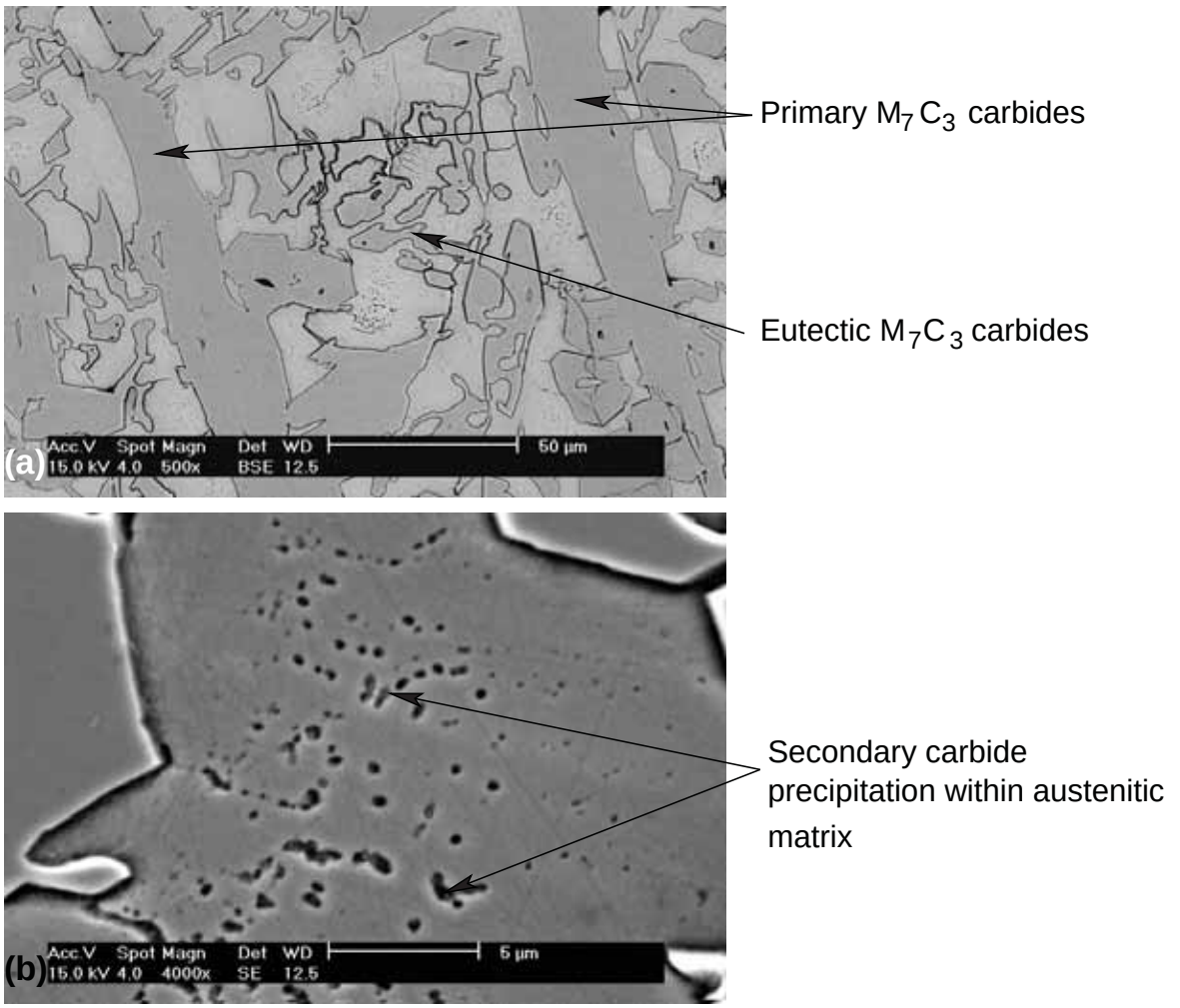

Figure 5.9: Electron micrographs of the HyperEXP casting in the as-cast condition. (a) Back scattered electron micrograph showing the distribution of the primary and eutectic M_7C_3 carbides and that the carbides do not have a duplex morphology. (b) Secondary electron micrograph showing the very fine morphology of the secondary carbides.

The bulk chemical composition and the chemical microanalysis results of the primary and eutectic M_7C_3 carbides and the matrix are given in Table 5.6. The bulk composition contains 4.5% carbon, 25% chromium giving a chromium to carbon ratio of about 5.6. What makes this alloy unique is the additions of 4.5% manganese and 4.8% nickel which are not considered in standards for high chromium white iron alloys. The primary M_7C_3 carbides were composed of approximately 54% chromium, 4.3% manganese, 0.2% molybdenum and 0.6% nickel with the silicon content of the carbides being negligible. The eutectic M_7C_3 carbides contained approximately 9% less chromium but increased concentrations of manganese, molybdenum and nickel. The matrix contained approximately 1.2% carbon, 8.7% chromium, 0.8% silicon, 5.8% manganese, 0.3% molybdenum and 8.4% nickel. The combined carbide volume fraction of the primary and eutectic carbides for the HyperEXP alloy was measured to be 50%.

Table 5.6: Bulk chemical composition, chemical composition of the carbides, matrix and CVF for the HyperEXP casting in the as-cast condition.

HyperEXP	Chemical Composition wt%							CVF*
	C	Si	Cr	Mn	Fe	Ni	Mo	
Bulk	4.50	0.45	25.00	4.50	60.30	4.80	0.33	49.9 ± 4.3
Primary M_7C_3 carbides	8.76 ± 0.13	0.01 ± 0.01	54.46 ± 0.83	4.31 ± 0.16	32.77 ± 0.47	0.56 ± 0.07	0.22 ± 0.04	
Eutectic M_7C_3 carbides	8.61 ± 0.09	0.01 ± 0.01	45.13 ± 2.15	6.32 ± 0.56	40.09 ± 1.35	0.67 ± 0.08	0.50 ± 0.10	
Matrix	1.20 ± 0.10	0.82 ± 0.04	8.66 ± 0.68	5.85 ± 0.56	76.54 ± 0.56	8.41 ± 0.30	0.26 ± 0.12	
* Carbide volume fraction of primary and eutectic M_7C_3 carbides								

The bulk hardness of the alloy and microhardness of the primary carbides and matrix phase are given in Table 5.7. The bulk hardness was measured to be 495 HV even though the CVF was around 50%. The microhardness of the matrix, which was austenite with limited very fine secondary carbides, was measured to be 390 HV. The hardness of the primary M_7C_3 carbides was measured to be 1590 HV.

Table 5.7: Bulk hardness and microhardness test results for the HyperEXP casting in the as-cast condition.

HyperEXP		
Bulk hardness (HV_{30})	Microhardness Matrix ($HV_{0.3\ \&\ 0.1}$)	Microhardness Carbides ($HV_{0.05}$)
496±5	391±33	1590±1040

5.2.1.5 WeldoverlayA

WeldoverlayA is a commercially deposited high chromium white iron weld overlay deposited on a steel substrate. The sample was taken from an ex-service alumina plant spool. The microstructure of a transverse section taken across consecutive weld beads for WeldoverlayA in the as-deposited condition is shown in Figure 5.10. The hypereutectic microstructure consists of primary M_7C_3 carbides of different orientations and a eutectic of M_7C_3 carbides and austenite.

Close to the wear surface, Area 1 in Figure 5.10(a) the primary carbides, which are rods of hexagonal cross section, were found in clusters of different orientations. Figure 5.10(b) highlights an area where the primary carbides have formed one such cluster. These clusters of primary carbides are referred to as the branched primary carbide morphology. The higher magnification image, Figure 5.10(c), shows that immediately surrounding the primary carbides is a region of austenite. These austenite regions are referred to as halos and in some regions the formation of austenite dendrites can be seen protruding from the corners of the primary carbides.

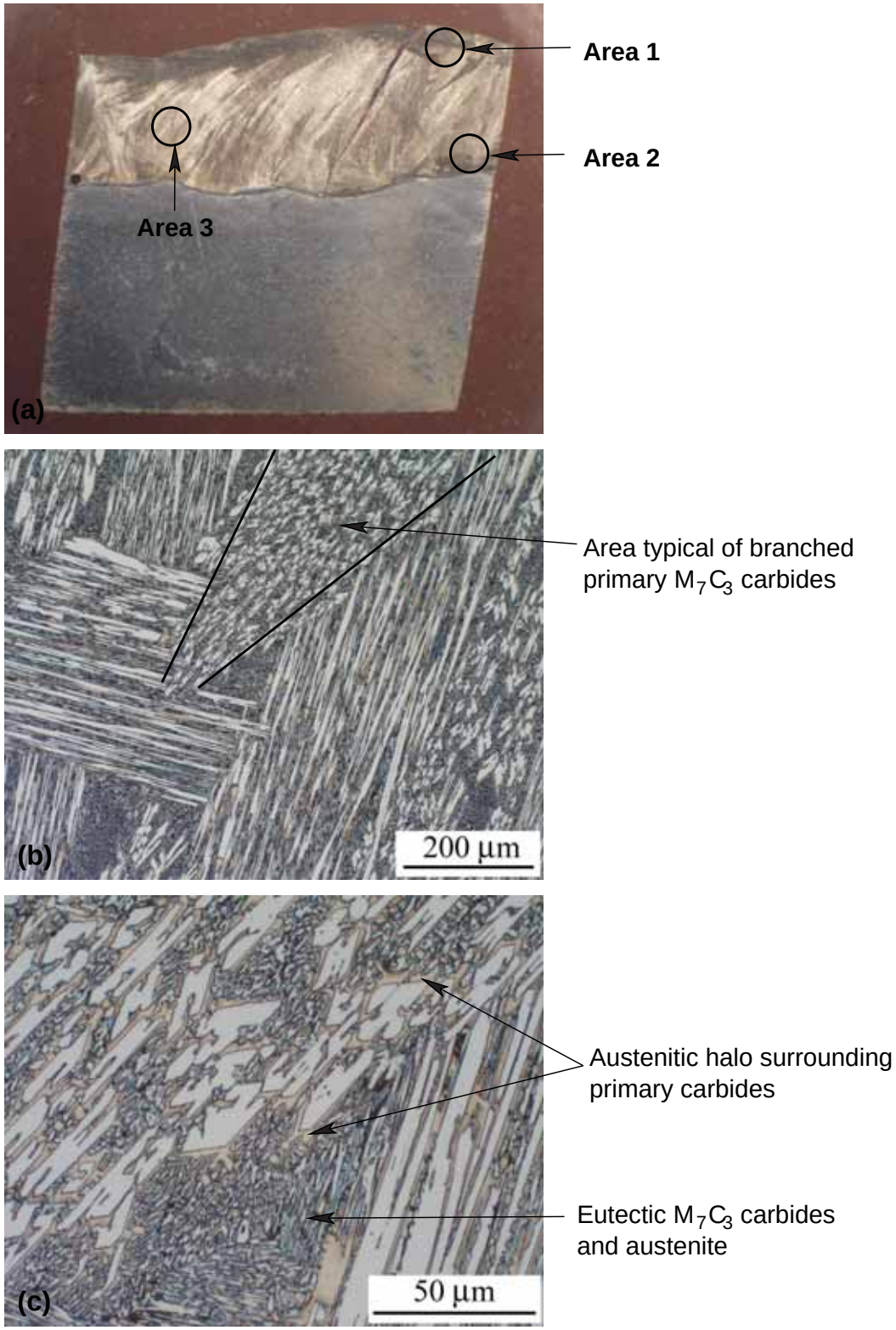

Figure 5.10: Metallographic examination of transverse section of WeldoverlayA. (a) general overview of metallographic sample showing the locations where micrographs were taken. (b) Micrograph of Area 1 adjacent to the surface showing the branched primary M_7C_3 carbide morphology, 100x magnification. (c) Higher magnification micrograph of (b) showing halos around the branched primary carbides and the eutectic of M_7C_3 carbides and austenite, 500x magnification.

Examination of the area adjacent to the weld overlay substrate interface, Area 2 in Figure 5.10(a), revealed a different microstructure to that found adjacent the surface shown in Figure 5.11(a). The microstructure shows regions of carbides arranged in the form of equilateral triangles. The distinct equilateral triangle carbide microstructure is referred to as the complex regular carbide morphology. Examination of other sample sections has also found the presence of the complex regular microstructure adjacent the weld overlay substrate interface.

The microstructure in the middle of the weld bead, Area 3 Figure 5.10(a), shows a different carbide morphology again, Figure 5.11(b). The microstructure also consists of primary M_7C_3 carbide rods and a eutectic of M_7C_3 carbides and austenite but the long axes of the carbide rods are aligned approximately perpendicular to the substrate.

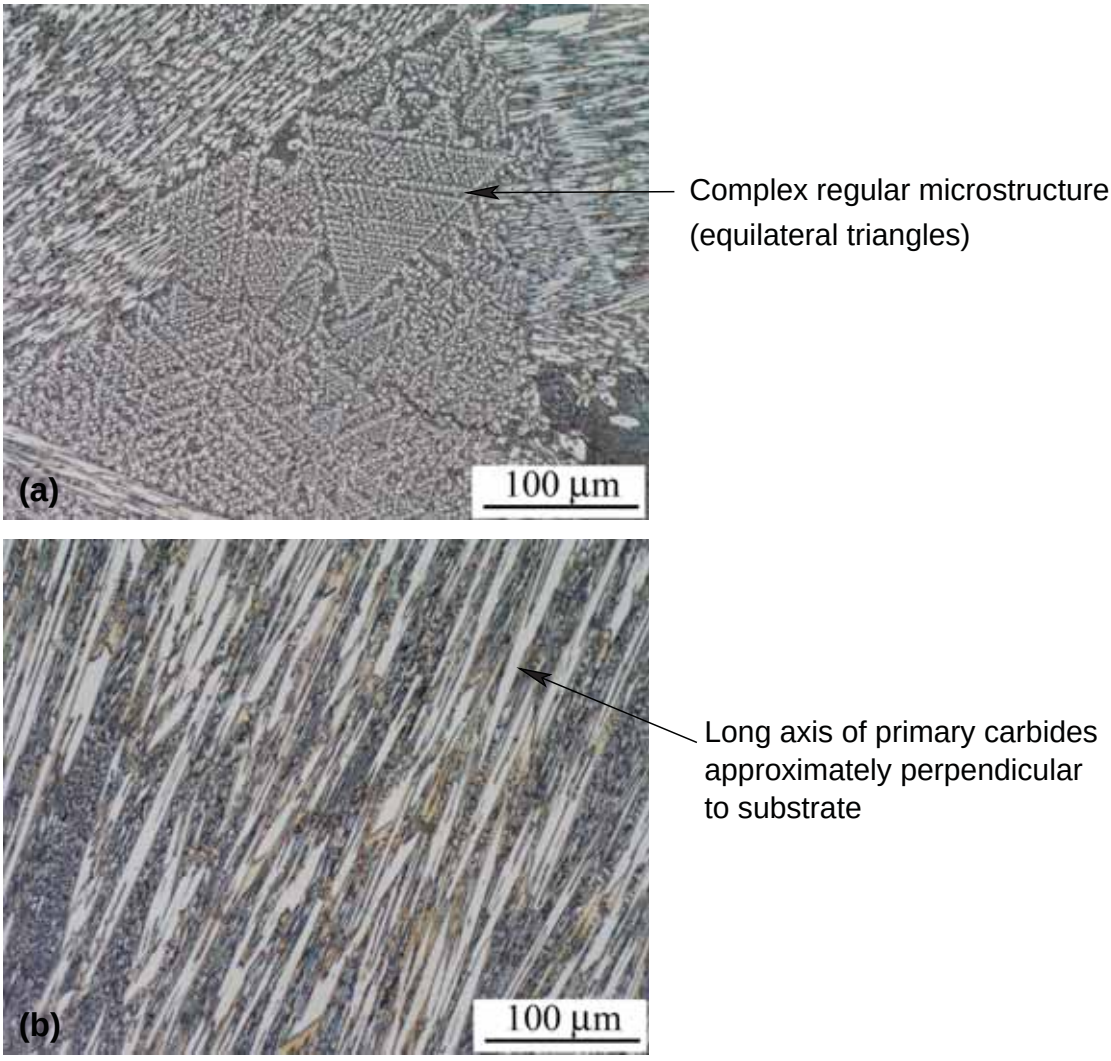

Figure 5.11: Light micrographs of transverse section of WeldoverlayA shown in Figure 5.10(a). (a) Micrograph of Area 2 adjacent to the steel substrate showing the complex regular carbide morphology as equilateral triangles, 200x magnification. (b) Micrograph of Area 3 showing the long axis of the primary M_7C_3 carbides is approximately perpendicular to the substrate, 200x magnification (Note: substrate is approximately parallel with bottom of figure).

When the surface parallel with the wear surface was examined, similar microstructural variations were found, Figure 5.12. Figures 5.12(b) and (c) show the respective microstructures of Area 1 and Area 2. The microstructure of Area 1 consists of primary M_7C_3 carbides surrounded by an austenite halo and a eutectic of M_7C_3 carbides and austenite. In the micrograph the primary carbide rods are nearly perpendicular to the plane of polish. The microstructure in Area 2, Figure 5.12(c) consists of the complex regular carbide morphology.

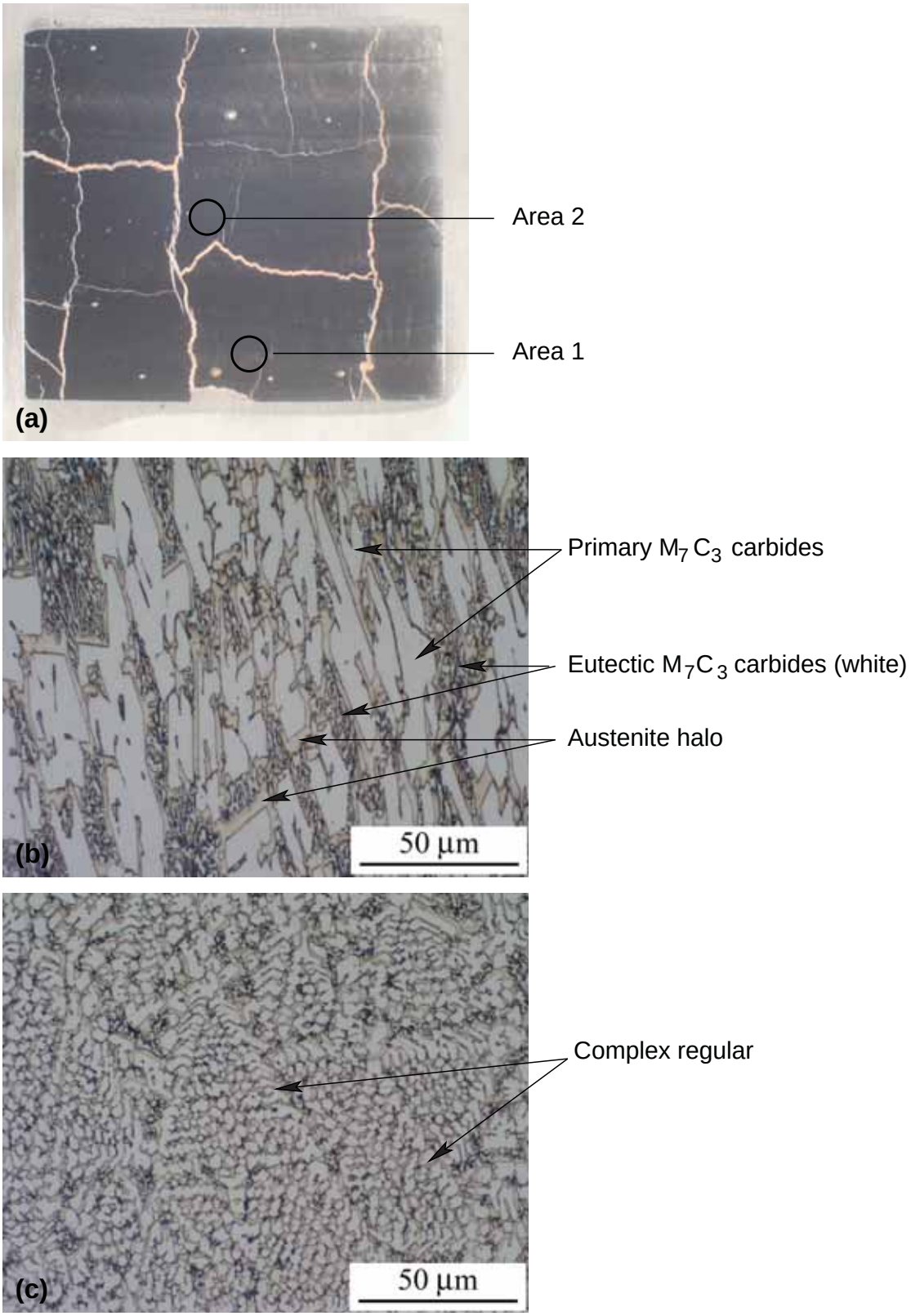

Figure 5.12: Metallographic examination of the surface of WeldoverlayA. (a) General overview of the metallographic sample showing the extent of check cracking and the location where micrographs were taken. (a) Micrograph of Area 1 showing primary M_7C_3 carbide, eutectic M_7C_3 carbides and austenite. A halo can be seen surrounding the primary M_7C_3 carbides, 500x magnification. (b) Micrograph of Area 2 showing the complex regular carbide microstructure, 500x magnification.

Further microstructural examination was done on lightly etched sample in an electron microscope, 5.13. The high magnification secondary electron images more clearly illustrate the eutectic M_7C_3 carbides and the precipitate free austenite halo regions surrounding the primary carbides. Typically the primary carbides are greater than 10μm in diameter and the eutectic carbides are much smaller being less than 2μm in diameter. The spacing between the eutectic carbides is also small, being less than 2μm. What is also evident from the high magnification micrograph shown in Figure 5.13(b) is the presence of martensite that surrounds the eutectic carbides and martensite laths extending into the eutectic austenite.

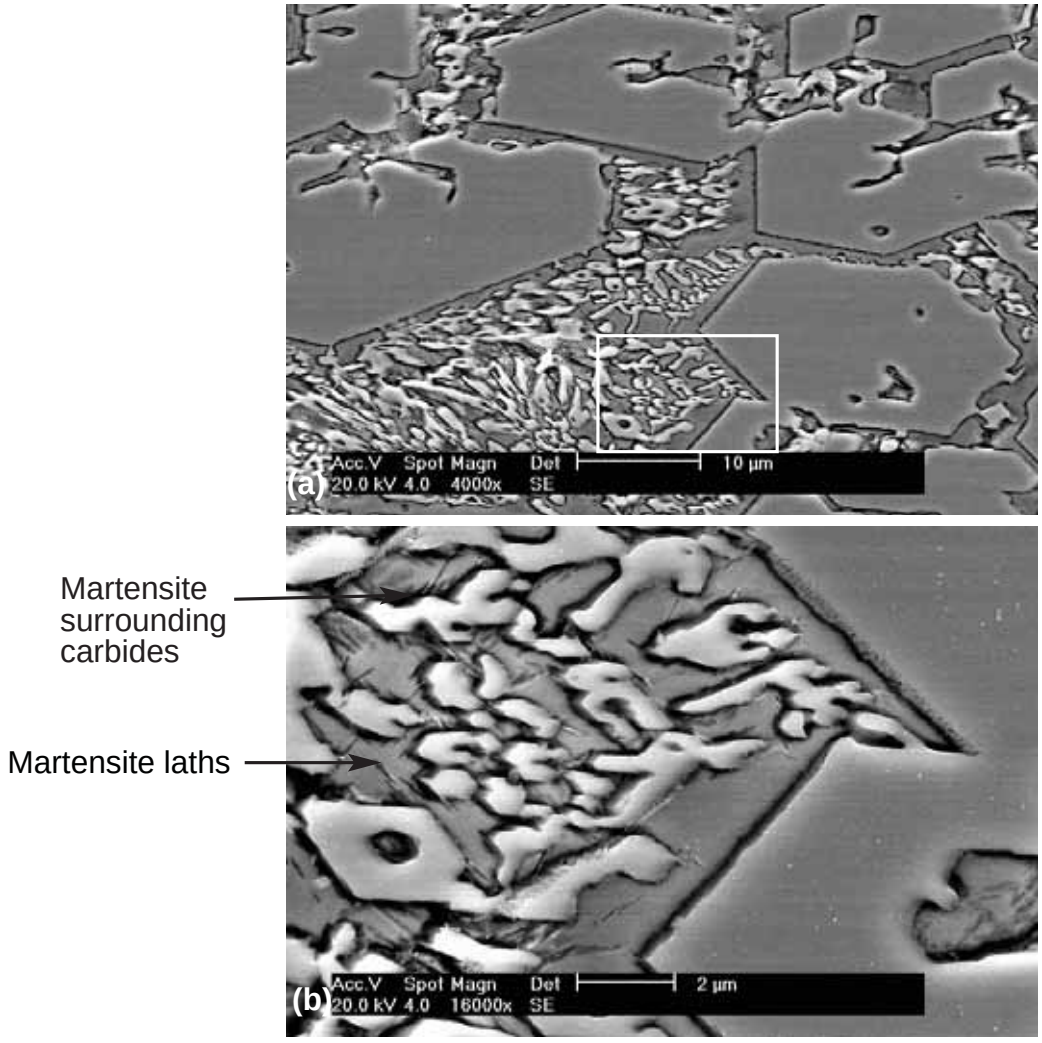

Figure 5.13: Secondary electron micrographs of WeldoverlayA. The examination surface is parallel with the wear surface. (a) Micrograph showing the primary and eutectic M_7C_3 carbides in an austenitic matrix. (b) Higher magnification micrograph of the boxed region in (a) showing martensite laths extending from regions surrounding the eutectic carbides into the matrix.

The bulk chemical composition and the chemical microanalysis results of the primary carbides and matrix for WeldoverlayA are given in Table 5.8. The carbon composition being 5.5% and chromium composition of approximately 25%, giving a chromium to carbon ratio of 4.5. With no significant addition of hardenability alloying elements this alloy is classi-

fied as a AS2576 23XX austenitic chromium carbide iron hardfacing. The primary M_7C_3 carbides were found to contain 42% chromium, 1.2% manganese and negligible traces of silicon, nickel and molybdenum. The eutectic M_7C_3 carbides were not analyzed due to the small eutectic carbide size being less than the machine resolution. The matrix chemical composition represents the composition of the halo regions, as the close spacing of the eutectic carbides did not allow the analysis of the eutectic austenite. The halo regions contained 1.3% carbon, 8% chromium 3% silicon and 1.2% manganese. The manganese of the matrix was found to be similar to the primary carbides. The carbide volume fraction of the primary and eutectic carbides was measured to be 59%.

Table 5.8: Bulk chemical composition, chemical composition of the primary carbides and austenitic matrix for WeldoverlayA.

WeldoverlayA	Chemical Composition wt%							CVF*
	C	Si	Cr	Mn	Fe	Ni	Mo	
Bulk	5.50	1.60	24.50	1.10	67.00	0.11	0.03	
Primary M_7C_3 carbides	9.06 ± 0.14	0.05 ± 0.02	42.19 ± 1.40	1.16 ± 0.05	47.82 ± 1.15	0.03 ± 0.02	0.00 ± 0.01	58.8 ± 2.4
Matrix	1.32 ± 0.20	2.94 ± 0.15	8.07 ± 0.76	1.23 ± 0.10	87.56 ± 0.78	0.29 ± 0.02	0.01 ± 0.01	
* Carbide volume fraction of primary and eutectic M_7C_3 carbides								

The bulk hardness of WeldoverlayA and the microhardness of the primary carbides are given in Table 5.9. The hardness of the matrix could not be measured due to the small inter-carbide spacings. The bulk hardness, measured on a plane parallel and adjacent to the wear surface was 850 HV. The hardness of the primary M_7C_3 carbides was measured to be 1485 HV.

Table 5.9: Bulk hardness and microhardness of the primary carbides for WeldoverlayA in the as-deposited condition.

WeldoverlayA		
Bulk hardness (HV_{30})	Microhardness Matrix ($HV_{0.3\ \&\ 0.1}$)	Microhardness Carbides ($HV_{0.05}$)
850±30	-	1484±116

5.2.1.6 WeldoverlayB

WeldoverlayB is a commercially deposited high chromium white iron weld overlay deposited on a steel substrate and the sample was removed from an ex-service alumina plant spool. The micrographs shown in Figure 5.14 are of a transverse cross section of consecutive weld beads. The microstructure, Figure 5.14(b), consists of primary M_7C_3 carbides and a eutectic of M_7C_3 carbides indicating a hypereutectic composition. The primary carbide rods have a number of different orientations with the long axis approximately aligned with the plane of polish in some locations and nearly perpendicular in other locations.

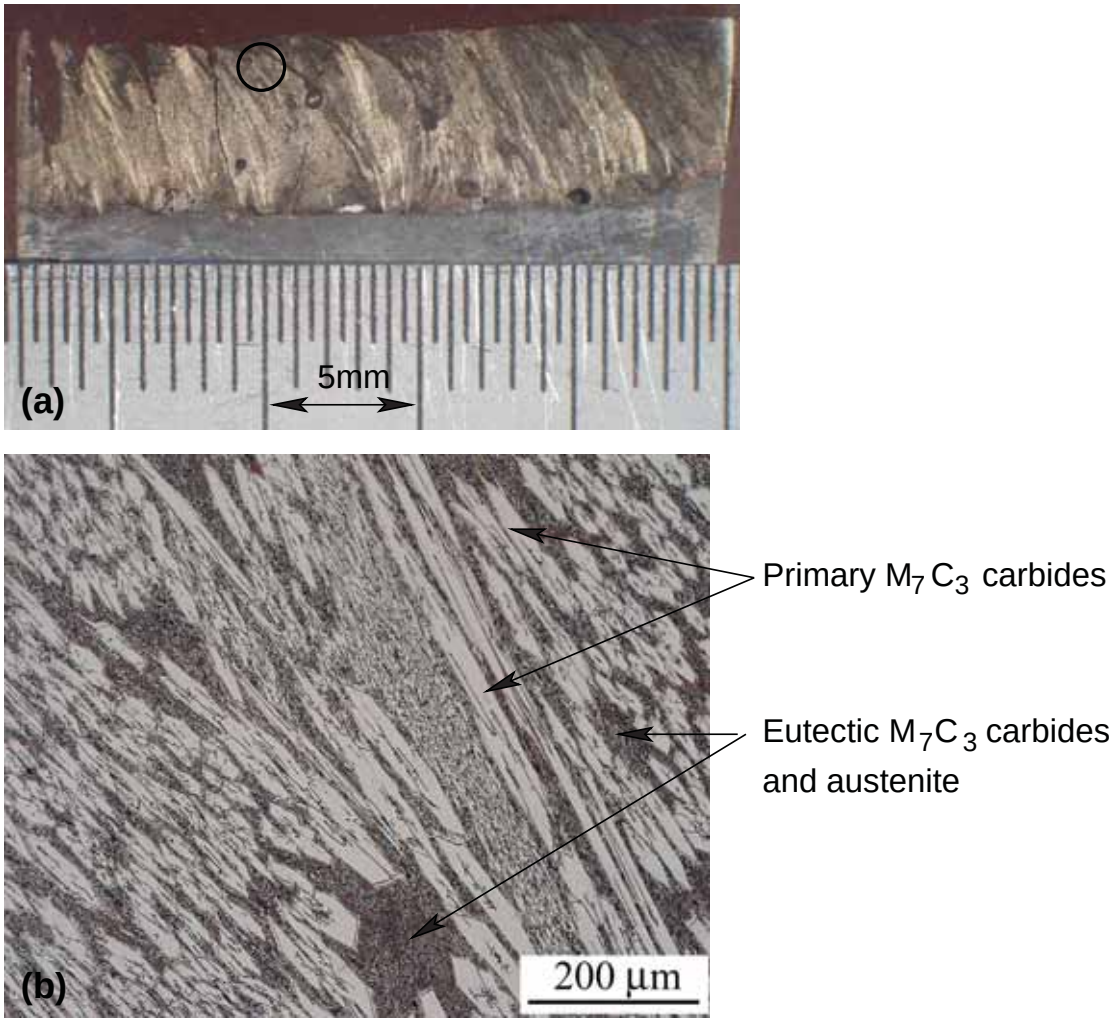

Figure 5.14: Metallographic examination of a transverse section of WeldoverlayB. (a) Transverse sample overview. (b) Optical micrograph showing the microstructure in the region circled in (a), 100x magnification.

When a longitudinal cross section relative to the weld beads is examined, Figure 5.15, the microstructure has a different appearance to that seen in the transverse cross section, Figure 5.14. The microstructure in Figure 5.15(b) shows that the primary carbide rods are approximately perpendicular to the plane of polish. It is also found that there is generally a band of the complex regular microstructure ranging in width up to about 2 mm adjacent to the weld overlay substrate interface, Figure 5.15(c). It was common to find cracking through the complex regular microstructure and sub surface gas pores.

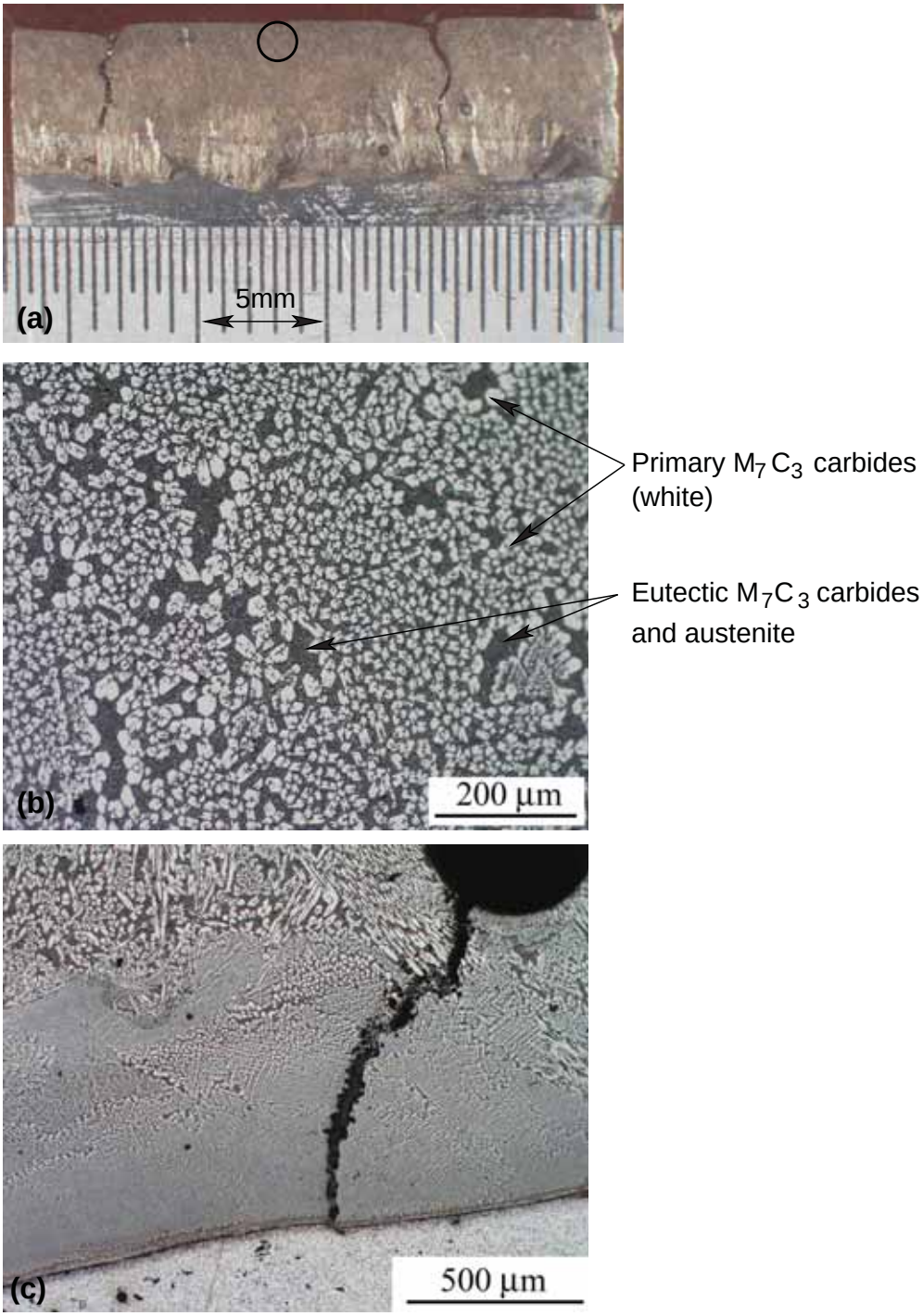

Figure 5.15: Metallographic examination of a longitudinal sample section of WeldoverlayB. (a) Longitudinal sample overview. Light micrograph showing the microstructure of the circled region adjacent the wear surface in (a), 100x magnification. (c) Light micrograph showing a gas pore and cracking through the complex regular microstructure to the weld overlay substrate interface, 50x magnification.

When the surface parallel to the wear surface is examined different microstructural variations are found, Figure 5.16. Figures 5.16(b) and (c) show the respective microstructures of Area 1 and Area 2 respectively. The microstructure in Area 1 consists of singular primary M_7C_3 carbides surrounded by a halo of austenite and a eutectic of fine M_7C_3 carbides and austenite.

The microstructure of Area 2 consists of the complex regular carbide morphology.

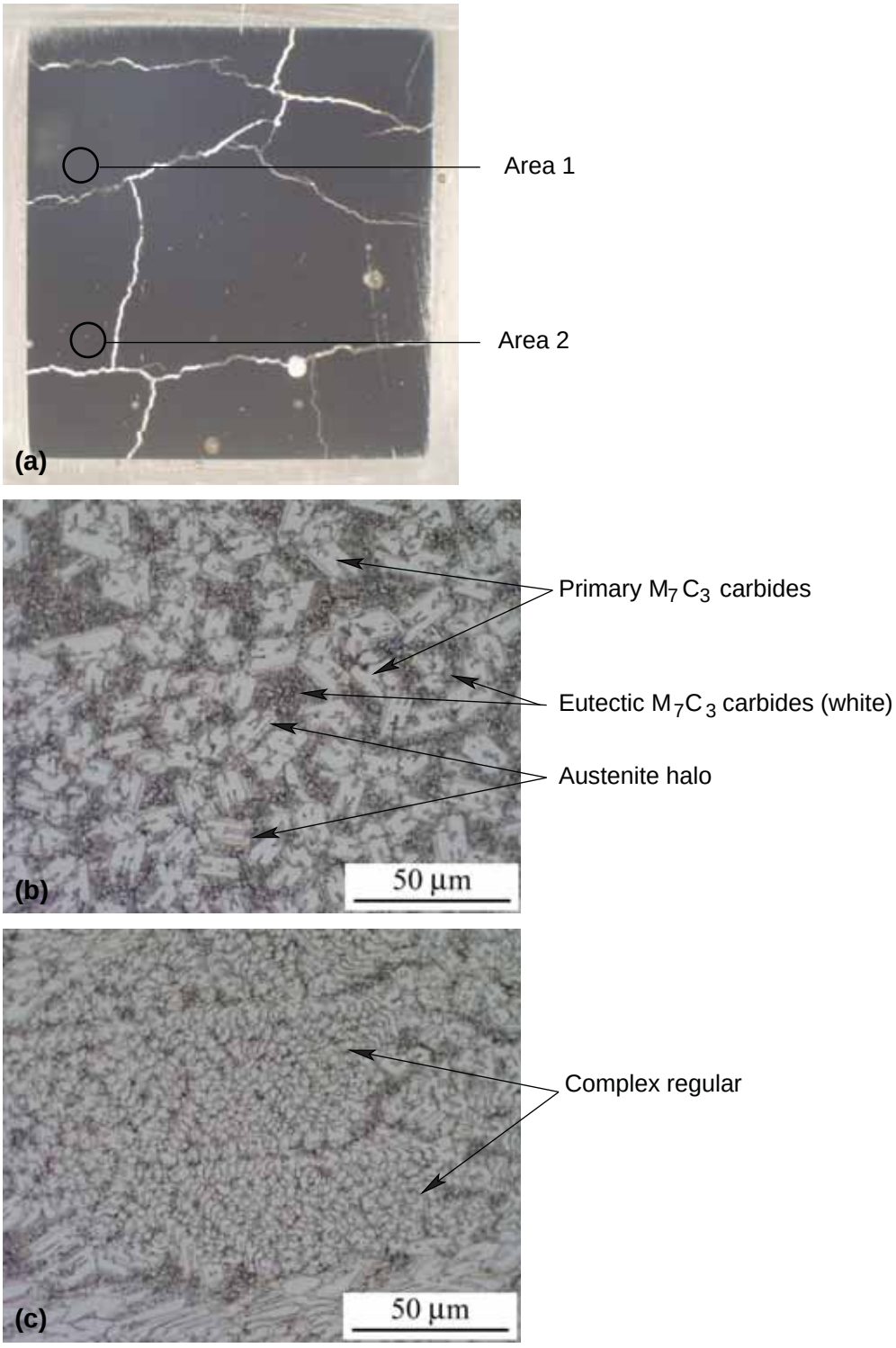

Figure 5.16: Metallographic examination of the surface of WeldoverlayB. (a) General overview of the metallographic sample showing the extent of check cracking and the location where micrographs were taken. (a) Micrograph of Area 1 showing primary M_7C_3 carbides and a eutectic of M_7C_3 carbides and austenite. A halo can also be seen surrounding the primary M_7C_3 carbides, 500x magnification. (b) Micrograph of Area 2 showing the complex regular carbide microstructure, 500x magnification.

The micrographs from the examination in the electron microscope are shown in Figure 5.17. The backscattered electron micrograph, Figure 5.17(a), clearly shows the halo that surrounds the primary carbides and the fine distribution of the eutectic carbide phase. The primary carbides are typically greater than 10μm in size and do not have a duplex morphology. The eutectic carbides were typically less than 3μm in diameter and the spacing between the eutectic carbides was also small, being less than 3μm, Figure 5.17(b).

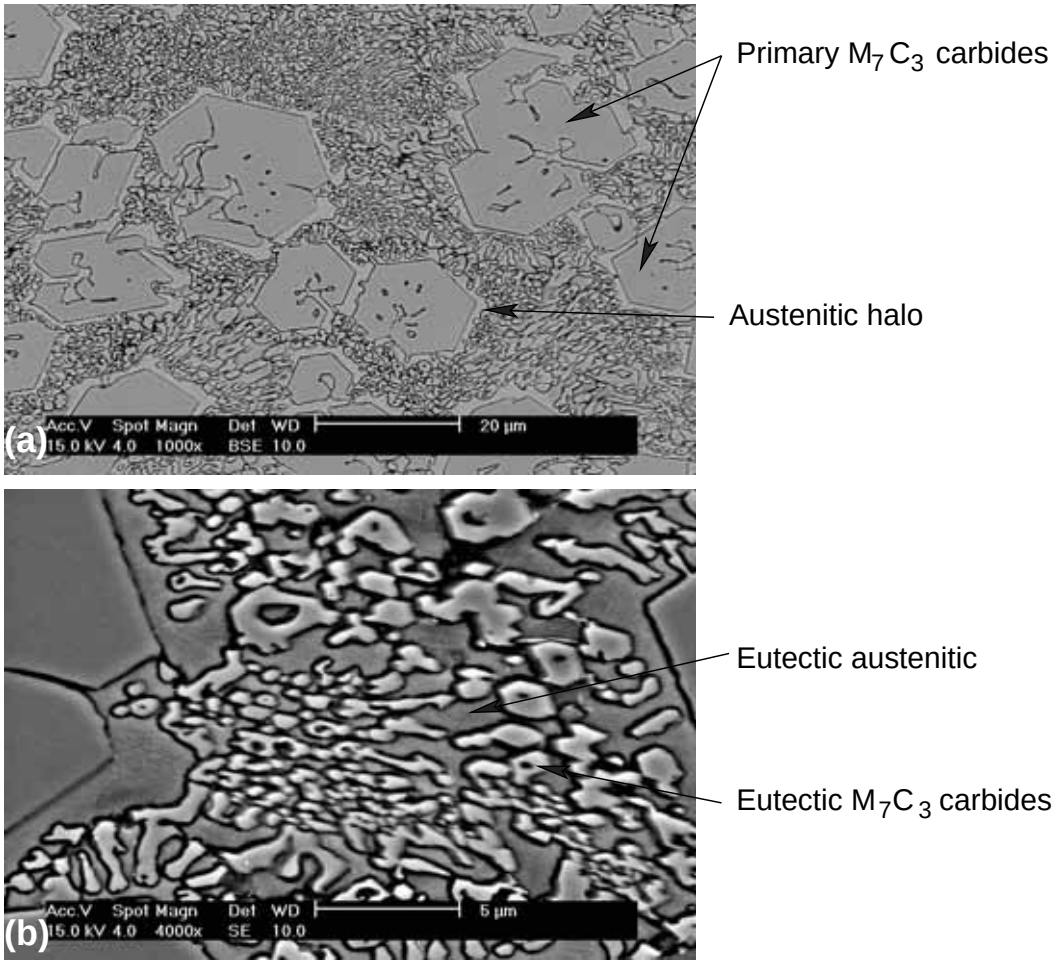

Figure 5.17: Electron micrographs of WeldoverlayB. The examination surface is parallel with the wear surface. (a) Micrograph showing the primary and eutectic M_7C_3 carbides in an austenitic matrix. (b) Higher magnification micrograph showing the eutectic carbides.

The bulk chemical composition and the chemical microanalysis results of the primary carbides and matrix are given in Table 5.10. The bulk carbon and chromium compositions are 4.9% and 27% chromium respectively, giving a chromium to carbon ratio of about 5.6. Due to the limited other alloying additions, this alloy is classified as an AS2576 23XX austenitic chromium carbide iron weld overlay. The chemical analysis of the primary M_7C_3 carbides found that the chromium and manganese contents were 47% and 1.3% respectively. The silicon, nickel and molybdenum contents were negligible. The eutectic M_7C_3 carbides could not accurately be measured due to their small size. The matrix chemical analysis, which represents the composition of the halo regions, was found to have 1.6% carbon, 10.6% chromium,

2% silicon, 1.4% manganese and small amounts of nickel. The carbide volume fraction of the primary and eutectic M_7C_3 carbides was measure to be 51%, Table 5.10.

Table 5.10: Bulk chemical composition, chemical composition of the primary carbides and austenitic matrix for WeldoverlayB.

WeldoverlayB	Chemical Composition wt%							CVF*
	C	Si	Cr	Mn	Fe	Ni	Mo	
Bulk	4.90	0.94	27.30	1.20	65.40	0.06	0.02	
Primary M_7C_3 carbides	9.09 ± 0.26	0.03 ± 0.01	46.55 ± 0.64	1.25 ± 0.02	43.17 ± 0.58	0.02 ± 0.02	0.01 ± 0.02	51.2 ± 3.4
Matrix	1.62 ± 0.13	1.94 ± 0.17	10.59 ± 1.31	1.44 ± 0.09	84.94 ± 1.54	0.22 ± 0.22	0.02 ± 0.03	
* Carbide volume fraction of primary and eutectic M_7C_3 carbides								

The bulk hardness of the alloy and the microhardness of the primary carbides are given in Table 5.11. The hardness of the matrix could not be measured due to the small inter-carbide spacings. The bulk hardness, measured on a plane parallel and adjacent to the wear surface, was found to be approximately 745 HV. The hardness of the primary M_7C_3 carbides was measured to be approximately 1560 HV.

Table 5.11: Bulk hardness and microhardness of the primary carbides for WeldoverlayB in the as-deposited condition.

WeldoverlayB		
Bulk hardness (HV_{30})	Microhardness Matrix ($HV_{0.3\ \&\ 0.1}$)	Microhardness Carbides ($HV_{0.05}$)
743±16	-	1558±146

5.3 Heat Treatments

5.3.1 Samples Investigated

Heat treatments were done on the four casting alloys, HypoA, EutecticA, HyperA and Hyper-EXP. The purpose of the heat treatments was to significantly alter the matrix microstructure to allow the changes in matrix microstructure to be related to the changes in corrosion and wear performance.

5.3.2 Heat Treatment Temperatures and Method

It has previously been reported that the maximum hardness for high chromium white irons is achieved through a destabilization heat treatment at temperatures between 920 and 1060°C for 1 to 6 hours (Pearce, 2002, Maratray and Poulalion, 1982). The destabilization heat treatments causes the precipitation of secondary carbides that reduce the carbon and chromium

content of the matrix and the subsequent transformation to martensite on cooling. The maximum bulk hardness is achieved when a combination of high carbon martensite and low retained austenite content is achieved. The temperature at which the maximum bulk hardness is achieved has been found to depend on the alloy content. It has also been reported that heat treatment temperatures greater than 1100°C can lead to the dissolution of any secondary carbides, reducing alloy segregation, producing a homogenized secondary carbide free austenitic structure (Tabrett et al., 1996).

To determine the optimum heat treatment temperatures, a heat treatment study was undertaken on the HyperA casting alloy. The HyperA casting was heat treated for 6 hours at temperatures from 800 to 1150°C in 50°C increments and furnace cooled. The heat treatment equipment and methodology is discussed in Section 5.3 with the results and a brief discussion given in Appendix A. It was found, for the HyperA alloy, that the maximum hardness is achieved at a heat treatment temperature of 950°C and a near fully austenitic matrix with very limited secondary carbide precipitation is achieved at a heat treatment temperature of 1150°C. These two heat treatment temperatures were chosen to heat treat all of the other castings investigated as they will give two distinctly different matrix microstructures.

When the 950°C and 1150°C heat treatments for 6 hours followed by furnace cooling were done on the HypoA and EutecticA castings, the alloys formed a pearlitic matrix. The presence of even small percentages of pearlite in high chromium white irons can significantly reduce the wear performance and for this reason alloys containing pearlite are not used in industry service environments. Thus, it would not be fruitful to comprehensively test alloys that contain pearlite. To prevent the formation of pearlite, after heat treatments, the samples were removed from the furnace and allowed to air cool. Air cooling after heat treatment was sufficient to prevent the formation of pearlite in the HypoA and EutecticA castings. The HyperA and HyperEXP castings were not affected by the cooling rate but air cooled samples following heat treatment are used for consistency. A comparison of the heat treated samples followed by furnace cooling and air cooling can be found in Appendix A.

5.3.3 Results of Heat Treatments on Casting Samples

5.3.3.1 HypoA

The HypoA casting was received in the heat treated, or destabilized condition, having a matrix microstructure of secondary carbides, martensite and retained austenite, Figure 5.1. The microstructure after the 1150°C heat treatment for 6 hours followed by air cooling is shown in Figure 5.18. The heat treatment at 1150°C has dissolved the majority of secondary carbides to form a homogeneous austenitic microstructure, Figure 5.18(b). The back scattered electron micrograph, Figure 5.19, shows that the carbides have not undergone any transformations to form a shell or duplex carbide morphology. It is found that there is very limited

secondary carbide precipitation that has occurred on the austenite grain boundaries. The heat treated alloy was found to be slightly magnetic, which would indicate the presence of martensite.

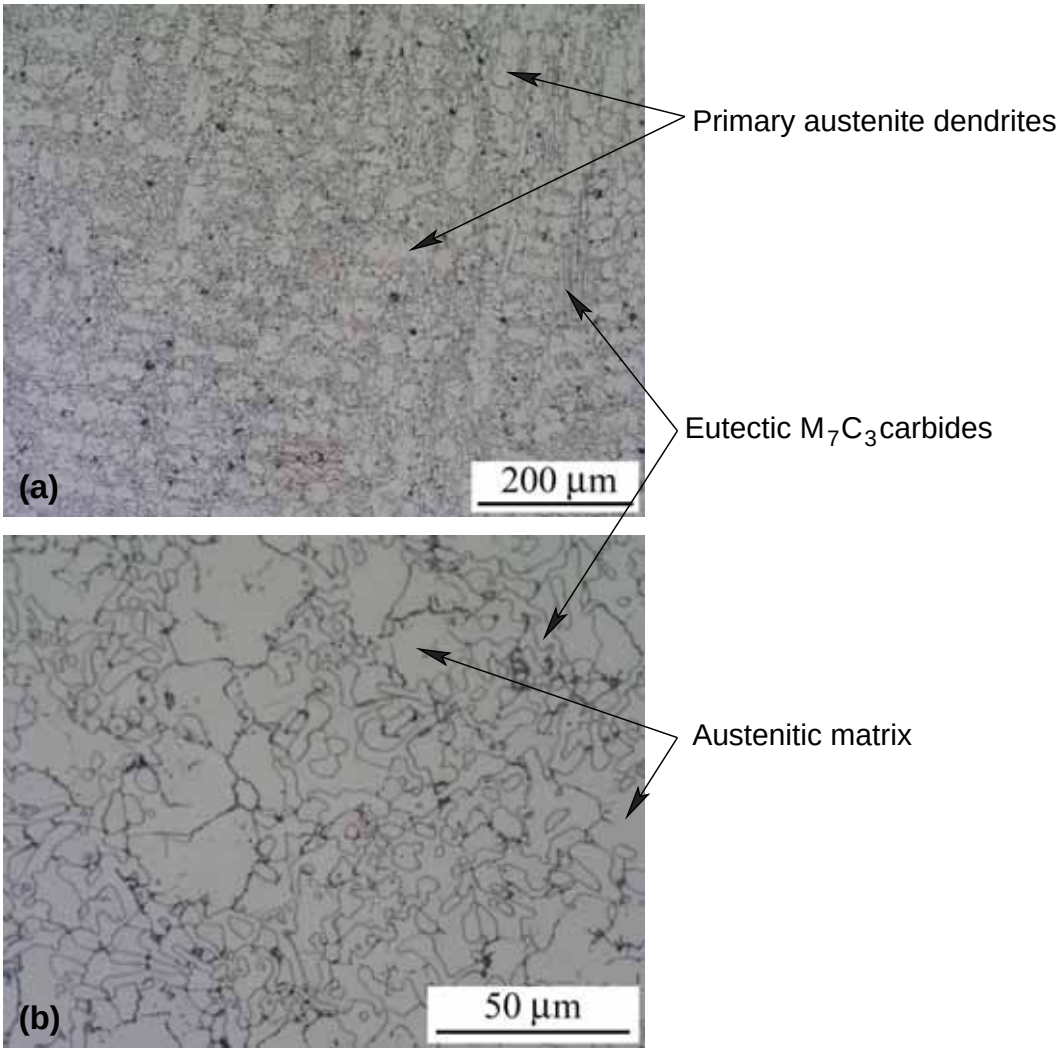

Figure 5.18: Optical micrographs of the HypoA casting after heat treatment at 1150°C for 6 hours followed by air cooling. (a) General micrograph showing the austenite dendrites. (b) Higher magnification micrograph showing the austenitic matrix.

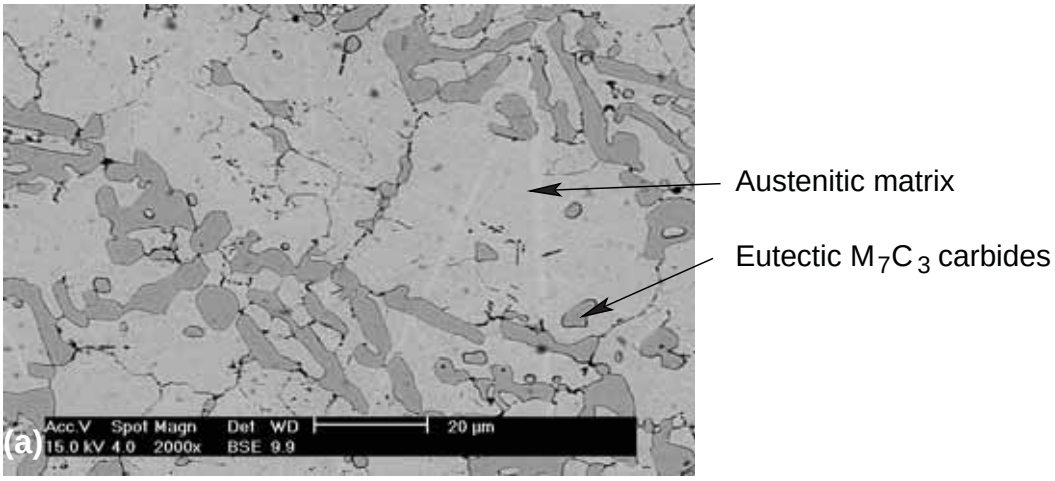

Figure 5.19: Back scattered electron micrograph of the HypoA casting after heat treatment at 1150°C for 6 hours followed by air cooling. There is limited secondary carbide precipitation on austenite grain boundaries.

The chemical composition of the matrix is given in Table 5.12. The matrix carbon and chromium content was found to be 0.7 and 14% respectively. The bulk hardness and matrix microhardness were measured to be a510 and 405 HV respectively, Table 5.13.

Table 5.12: Chemical composition of the matrix for the HypoA casting after heat treatment at 1150°C for 6 hours followed by air cooling.

HypoA		Chemical Composition wt%						
		C	Si	Cr	Mn	Fe	Ni	Mo
1150°C for 6 hours "Normalized"	Matrix	0.70 ± 0.11	1.27 ± 0.04	13.78 ± 0.24	0.76 ± 0.02	83.20 ± 0.38	0.18 ± 0.03	0.01 ± 0.02

Table 5.13: Bulk hardness and microhardness of the matrix for HypoA in the normalized condition.

HypoA		
Heat Treatment	Bulk hardness (HV_{30})	Microhardness Matrix ($HV_{0.3\ \&\ 0.1}$)
1150°C for 6 hrs - Normalized	510±15	405±28

5.3.3.2 EutecticA

The EutecticA casting, initially in the as-cast condition, was heat treated at both 950°C and 1150°C for 6 hours followed by air cooling. The microstructure of the EutecticA alloy after the 950°C heat treatment is shown in Figure 5.20. The optical micrograph, Figure 5.20(b), shows that there has been precipitation of secondary carbides and the matrix has transformed to martensite. The secondary carbides can not be resolved clearly in the optical micrographs. The electron micrographs of the 950°C heat treated sample, Figure 5.21, more clearly show the distribution of secondary carbides and the variation in etched matrix microstructure. The

back scattered electron micrograph, Figure 5.21(a), shows that the eutectic M_7C_3 carbides have not undergone any transformation to form a shell or duplex carbide. The secondary carbides are found to precipitate in regions that are separated from the eutectic carbides. The high magnification secondary electron image, Figure 5.21(b), shows that the secondary carbide morphology generally consist of small particles, sub micron in size, and have a cube morphology. Some small rod or blade secondary carbides were also noticed.

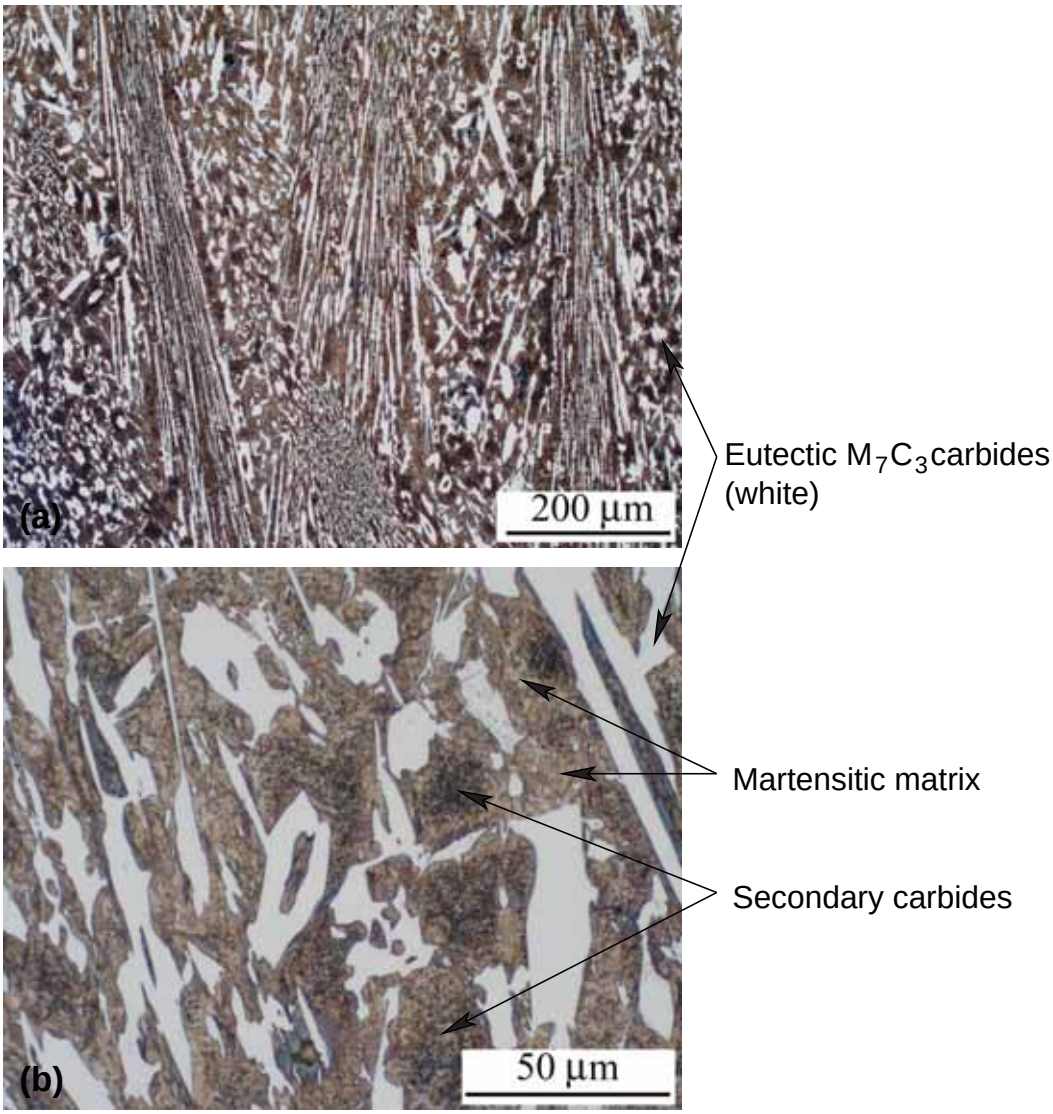

Figure 5.20: Optical micrographs of the EutecticA castings after heat treatment at 950°C for 6 hours followed by air cooling. (a) General micrograph showing that the matrix has transformed. (b) Higher magnification micrograph showing secondary carbides in a martensitic matrix.

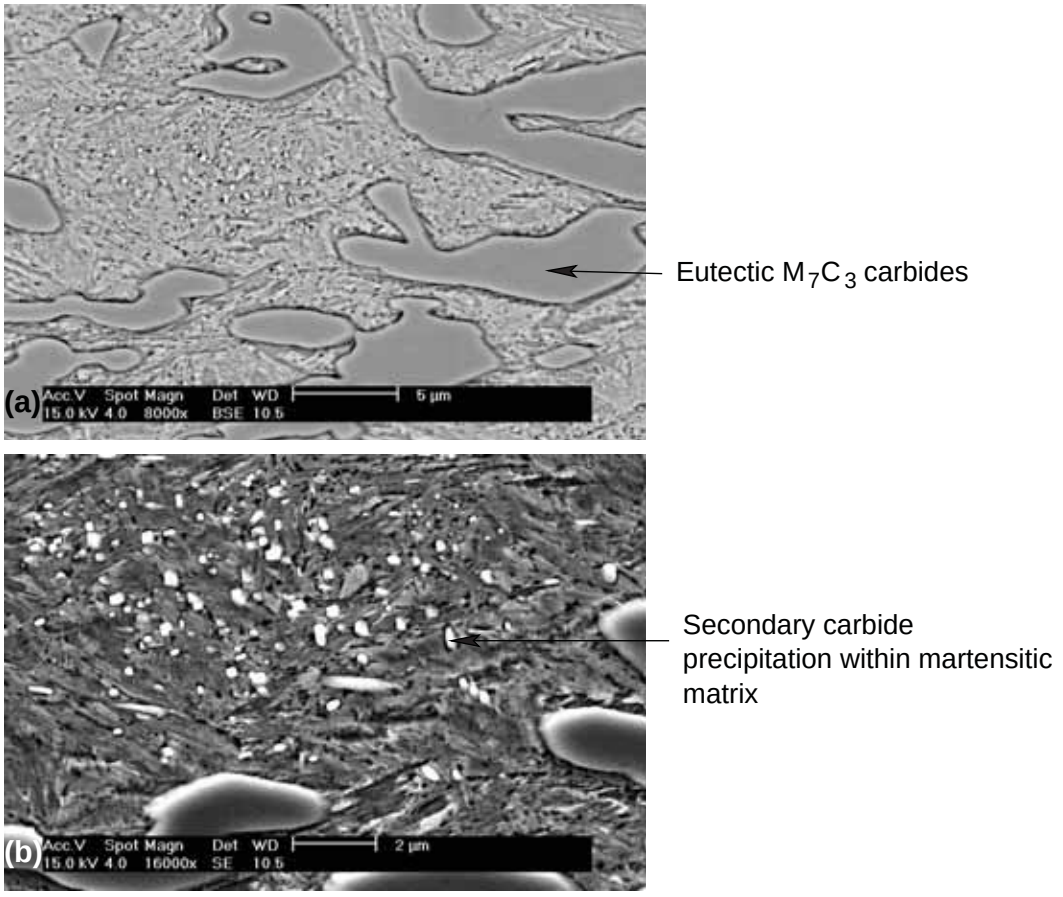

Figure 5.21: Electron micrographs of the EutecticA casting after heat treatment at 950°C for 6 hours followed by air cooling. (a) Back scattered electron micrograph showing the eutectic carbides have not undergone any transformation. (b) Secondary electron micrograph showing the morphology of the secondary carbides.

The microstructure of the EutecticA alloy after the 1150°C heat treatment is shown in Figure 5.22. The darker regions in Figure 5.22(a) are an etching effect associated with the closely spaced eutectic carbides. The higher magnification micrograph, Figure 5.22(b), shows that the matrix is substantially free of secondary carbides and pearlite that was found in the as-cast condition. The back scattered electron micrograph, Figure 5.23, showed that the carbides did not undergo any changes such as the formation of a duplex shell. However, the matrix did show some slight variations in contrast which is likely due to the presence of regions of martensite. The presence of martensite is supported by the heat treated alloy being magnetic.

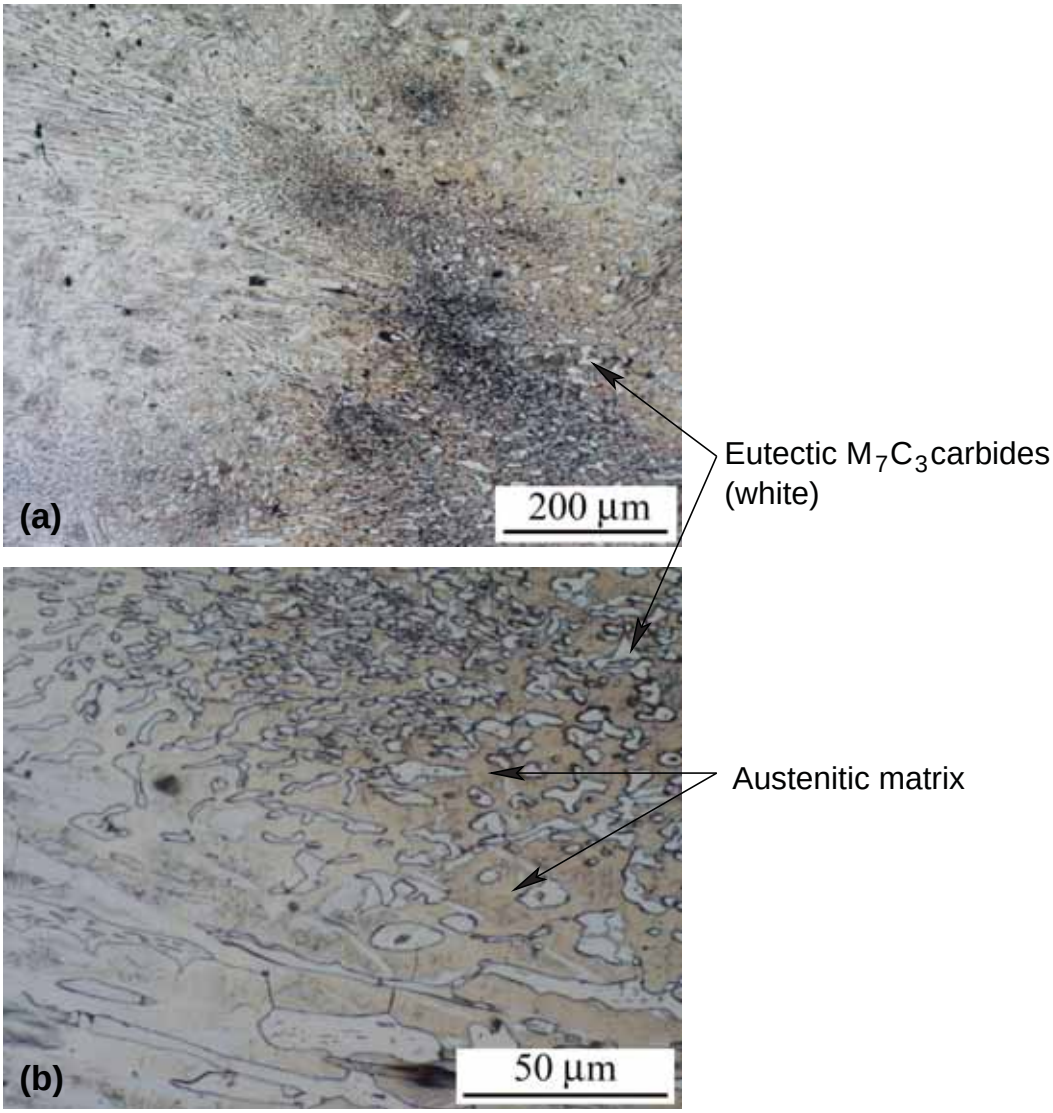

Figure 5.22: Optical micrographs of the EutecticA castings after heat treatment at 1150°C for 6 hours followed by air cooling. (a) General micrograph showing variation in the etched microstructure (b) Higher magnification micrograph showing the matrix is generally free of secondary carbides.

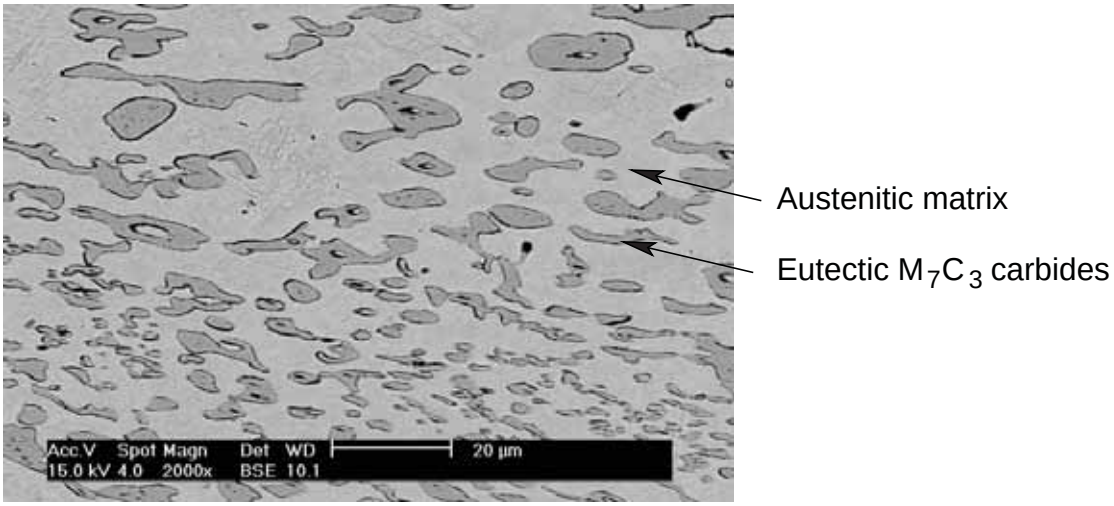

Figure 5.23: Back scattered electron micrograph of the EutecticA castings after heat treatment at 1150°C for 6 hours followed by air cooling. There is negligible secondary carbide precipitation and a slight variation in matrix contrast is noticed that is likely due to the presence of martensite.

The chemical composition of the matrix for the 950°C and 1150°C heat treatment conditions and the chemical composition of the eutectic M_7C_3 carbides is given in Table 5.14. The chemical composition of the carbides was analyzed on the 950°C heat treated sample as it was not done for the as-cast condition. The eutectic M_7C_3 carbides were found to contain 46% chromium, 0.7% manganese, 1.4% molybdenum and no silicon or nickel. The matrix of the 950°C heat treated condition had a composition of 7% chromium, 0.8% carbon 0.8% silicon and manganese and 1% molybdenum. After the 1150°C heat treatment, the matrix chromium content was found to increase by 4% to 11%, and the molybdenum content from 1% to 1.4%. The manganese and nickel contents were similar for the two heat treatment conditions. The matrix silicon and carbon compositions were found to decrease by 0.17%.

Table 5.14: Chemical composition of the matrix after heat treatment at 950 and 1150°C and the chemical composition of the eutectic carbides after heat treatment at 950°C for the EutecticA casting.

EutecticA		Chemical Composition wt%						
		C	Si	Cr	Mn	Fe	Ni	Mo
950°C for 6 hours "Destabilized"	Eutectic M_7C_3 carbides	8.38 ± 0.15	0.00 ± 0.00	45.63 ± 1.63	0.72 ± 0.06	44.19 ± 1.14	0.00 ± 0.00	1.39 ± 0.24
950°C for 6 hours "Destabilized"	Matrix	0.81 ± 0.11	0.79 ± 0.02	7.14 ± 0.30	0.76 ± 0.03	90.81 ± 0.88	0.18 ± 0.02	1.01 ± 0.48
1150°C for 6 hours "Normalized"	Matrix	0.63 ± 0.08	0.62 ± 0.02	10.85 ± 0.55	0.75 ± 0.08	85.59 ± 0.83	0.17 ± 0.10	1.41 ± 0.37

The bulk hardness and the matrix microhardness for the 950°C and 1150°C heat treatments are given in Table 5.15. The bulk hardness of the 950°C heat treated sample, having a matrix of secondary carbides and martensite, was measured to be 870 HV. The bulk hardness of the 1150°C heat treated sample, having a dominantly austenitic matrix, was measured to be 510

HV. The large variations in bulk hardness reflects the large variation in matrix microhardness. The matrix hardness of the 950°C and 1150°C heat treatments were measured to be 770 and 470 HV respectively. The microhardness of the eutectic M_7C_3 carbides for the 950°C heat treated alloy was measured to be approximately 1465 $\pm$160 HV.

Table 5.15: Bulk hardness and the microhardness of the matrix after heat treatment at 950 and 1150°C for the EutecticA casting.

EutecticA		
Heat Treatment	Bulk hardness (HV_{30})	Microhardness Matrix ($HV_{0.1}$)
950°C for 6 hrs - Destabilized	872$\pm$28	767$\pm$26
1150°C for 6 hrs - Normalized	508$\pm$26	467$\pm$48

5.3.3.3 HyperA Casting

The HyperA casting was received in the as-cast condition and was heat treated at 950°C and 1150°C for 6 hours followed by air cooling. After the heat treatment at 950°C, the resulting microstructure is shown in Figure 5.24. The heat treated microstructure, Figure 5.24, shows that considerable precipitation of secondary carbides has occurred. It is noticed that the secondary carbides did not precipitate in the regions immediately surrounding the carbides, Figure 5.24(b). The matrix is expected to be predominantly martensite and some retained austenite.

The electron micrographs better illustrate the extent of secondary carbide precipitation, Figure 5.25. The back scattered electron micrograph, Figure 5.25(b) shows that the precipitation of the secondary carbides did not occur in regions adjacent to the carbides. However, the precipitation of the secondary carbides was extensive throughout the matrix. Figure 5.25(c) shows that the secondary carbide morphology consists of sub micron rods and smaller cubic carbides. The secondary carbides are either M_7C_3 rods or $M_{23}C_6$ or cubic carbides.

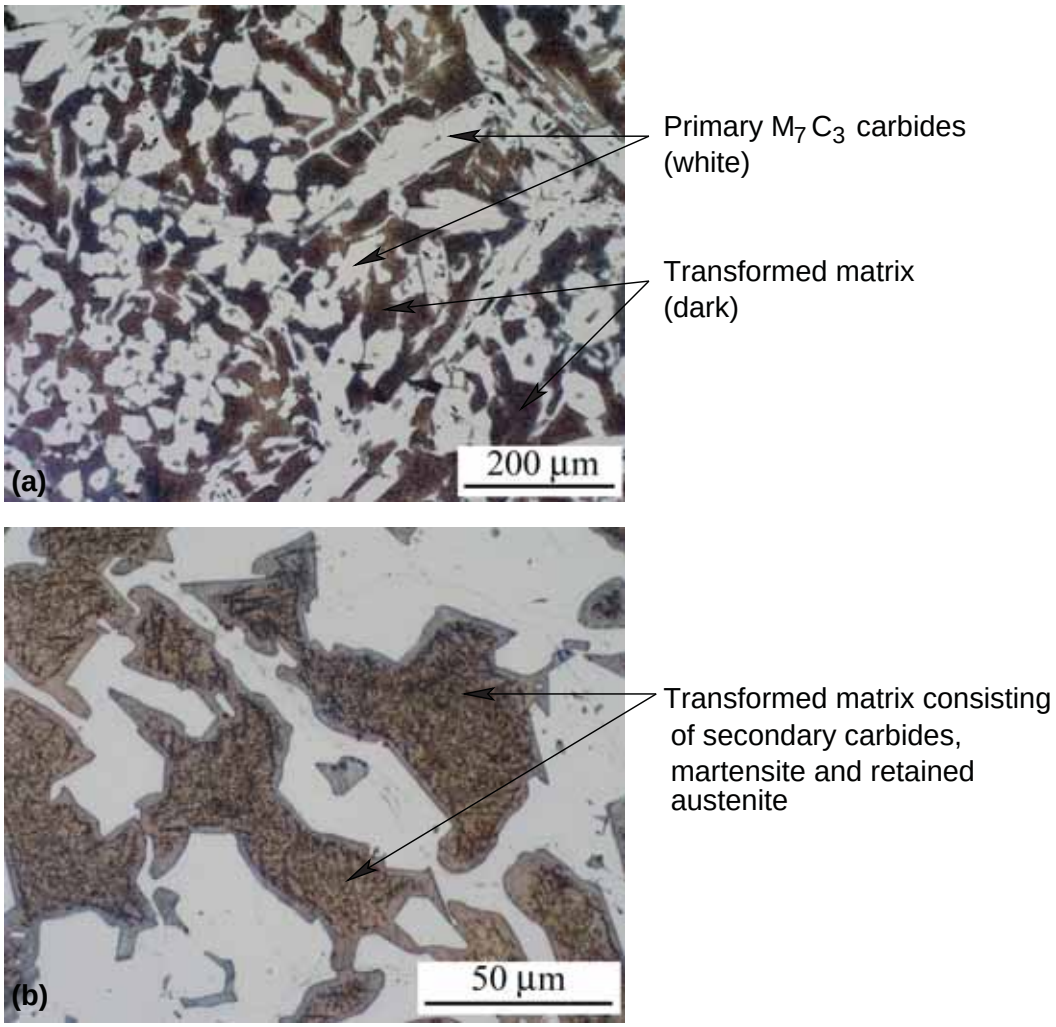

Figure 5.24: Optical micrographs of the HyperA castings after heat treatment at 950°C for 6 hours followed by air cooling. (a) General micrograph showing transformed matrix (b) Higher magnification micrograph showing the extensive precipitation of secondary carbides and a region surrounding the carbides where no precipitation occurred.

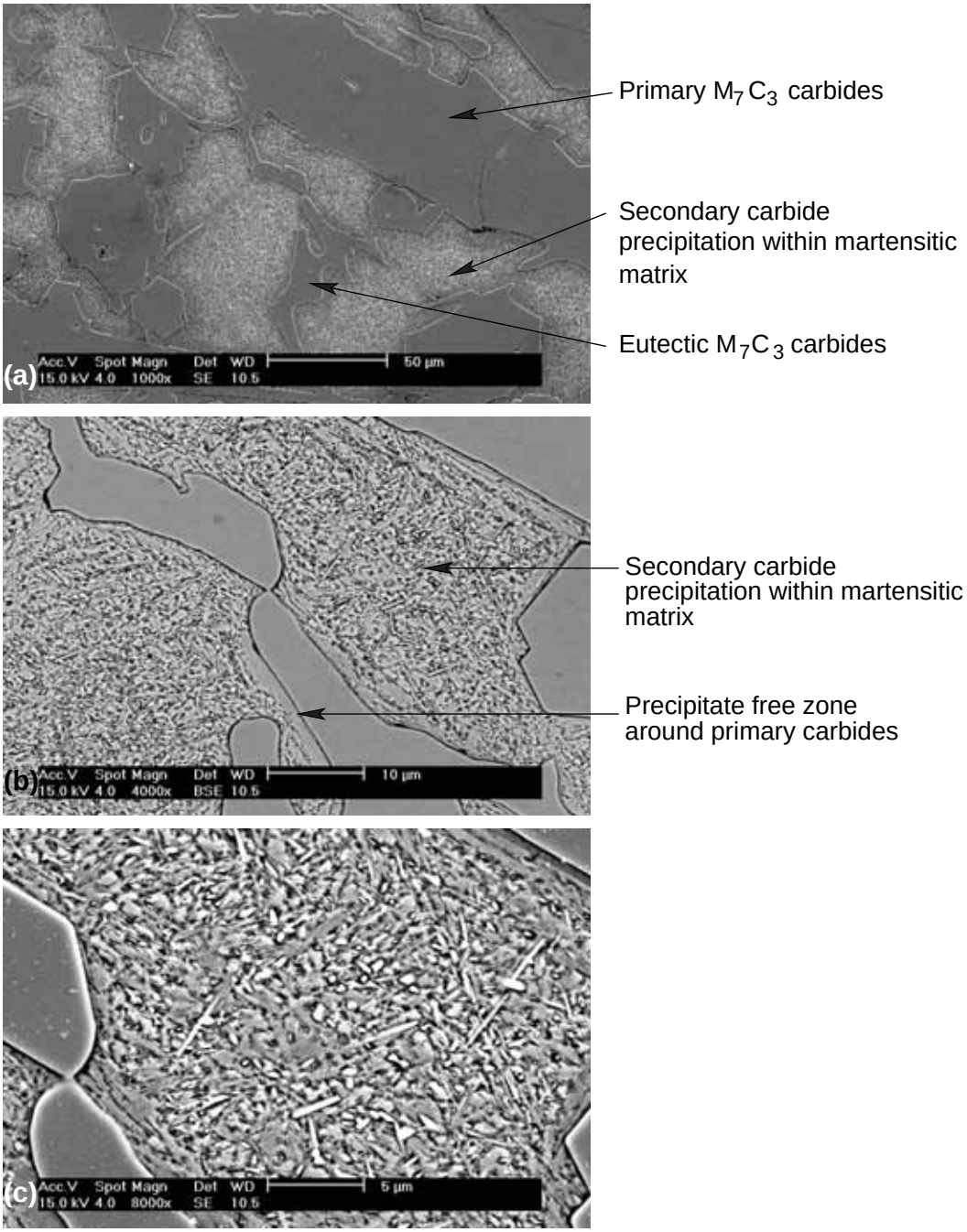

Figure 5.25: Electron micrographs of the HyperA casting after heat treatment 950°C for 6 hours followed by air cooling. (a) General secondary electron micrograph (b) Back scattered electron micrograph showing precipitate free zone around the carbides and the extensive precipitation of secondary carbides. (c) Secondary electron micrograph showing the morphology of the secondary carbides.

The microstructure after the 1150°C heat treatment for 6 hours and air cooling results in a matrix that is composed almost entirely of austenite, Figure 5.26. The sample was still slightly magnetic indicating there is some transformation of austenite to martensite. In a few isolated areas within the austenitic matrix there are some secondary carbides which either precipitated during heat treatment or did not completely dissolve during heat treatment, Figure 5.26(c). The back scattered electron image, Figure 5.27 shows the homogeneous

austenitic matrix and that the primary and eutectic carbides have not undergone any changes.

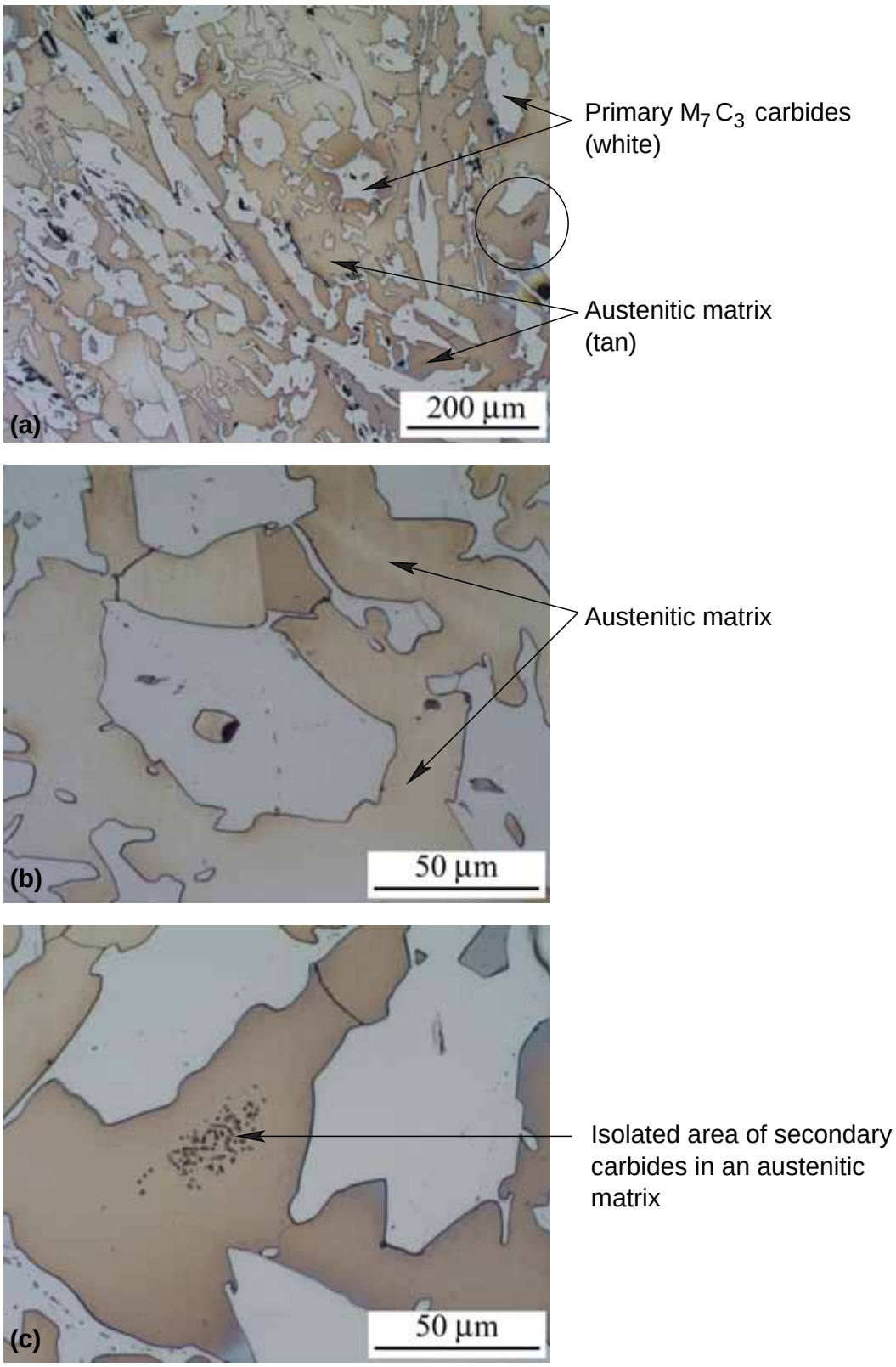

Figure 5.26: Optical micrographs of the HyperA castings after heat treatment at 1150°C for 6 hours followed by air cooling, (a) General micrograph showing the austenitic matrix. (b) Higher magnification micrograph showing the homogeneous nature of the austenitic matrix. (c) Higher magnification of the region circled in (a) showing secondary carbides.

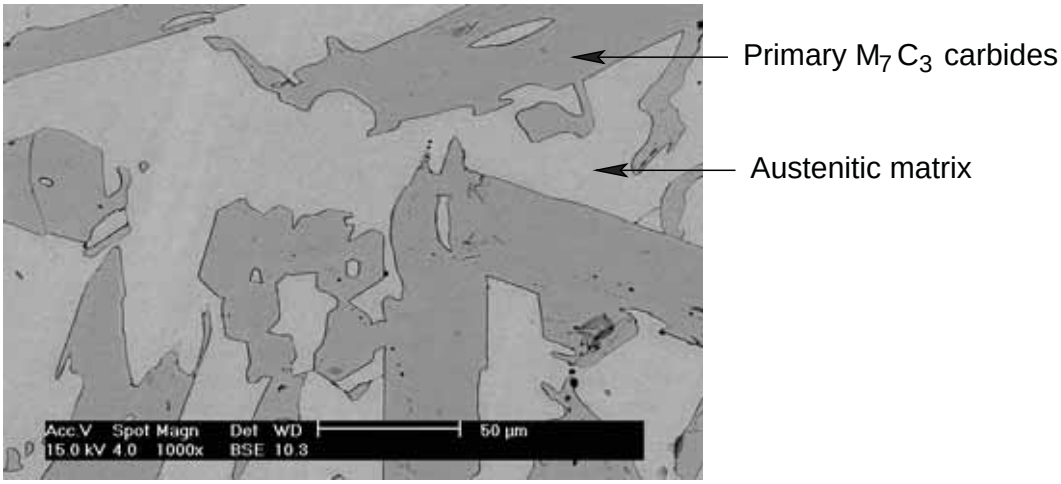

Figure 5.27: Back scattered electron micrographs of the HyperA casting after heat treatment at 1150°C for 6 hours followed by air cooling. The matrix is austenitic and the primary and eutectic carbides are unchanged.

The chemical composition of the matrix, the bulk hardness and the microhardness of the matrix after the 950 and 1150°C heat treatment is given in Table 5.16 and Table 5.17 respectively. After the 950°C heat treatment the carbon and chromium compositions of the transformed matrix was 0.95% and 9.6% respectively. The matrix also contained 0.9% silicon, 2.2% manganese and 1.6% molybdenum. After the 1150°C heat treatment the matrix carbon content was similar but the chromium composition had increased by 1.2% to 10.8%. The silicon and manganese composition decreased by 0.5% and the molybdenum composition increased by 0.2%. The bulk hardness of the 950°C heat treated alloy was measured to be 880 HV, compared with about 565 HV for the 1150°C heat treated alloy. The micro hardness of the matrix was measured to be 670 and 370 HV for the 950°C and 1150°C heat treated conditions respectively.

Table 5.16: Chemical compositions of the matrix, the bulk hardness and the microhardness of the matrix for the HyperA casting after heat treatment at 950 and 1150°C for 6 hours followed by air cooling.

HyperA		Chemical Composition wt%						
		C	Si	Cr	Mn	Fe	Ni	Mo
950°C for 6 hours "Destabilized"	Matrix	0.95 ± 0.18	0.91 ± 0.03	9.62 ± 0.73	2.28 ± 0.11	83.30 ± 0.90	0.60 ± 0.02	1.58 ± 0.54
1150°C for 6 hours "Normalized"	Matrix	0.91 ± 0.11	0.87 ± 0.01	10.80 ± 0.18	2.20 ± 0.06	83.75 ± 0.42	0.59 ± 0.02	1.78 ± 0.31

Table 5.17: Bulk hardness and the microhardness of the matrix after heat treatment at 950 and 1150°C for the HyperA casting.

HyperA		
Heat Treatment	Bulk hardness (HV_{30})	Microhardness Matrix ($HV_{0.3}$)
950°C for 6 hrs - Destabilized	880±13	671±11
1150°C for 6 hrs - Normalized	566±14	366±17

5.3.3.4 HyperEXP

The HyperEXP casting, originally in the as-cast condition was heat treated at 950°C and 1150°C for 6 hours followed by air cooling. The microstructure after the 950°C destabilization heat treatment is shown in Figure 5.28. The micrograph in Figure 5.28(b) shows that extensive secondary carbide precipitation within the matrix has occurred. The heat treated alloy was non magnetic and is therefore comprised of carbides and austenite only (i.e. no transformation to martensite occurred).

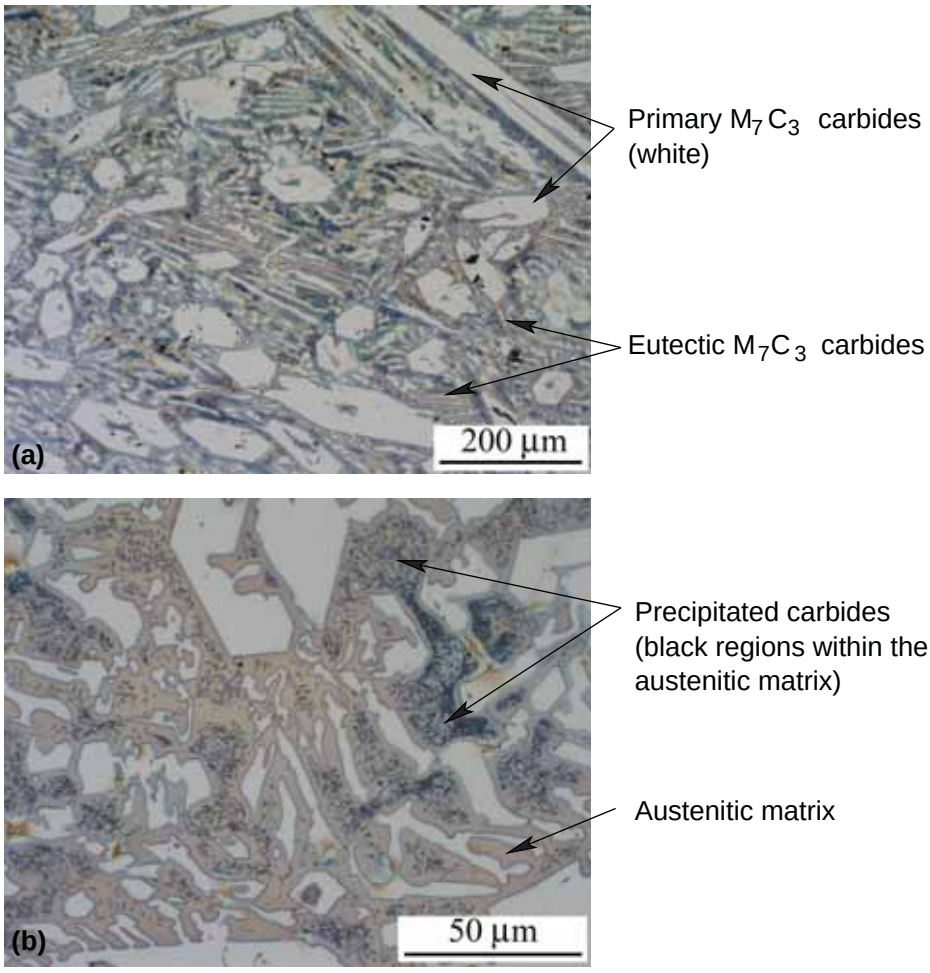

Figure 5.28: Optical micrographs of the HyperEXP castings after heat treatment at 950°C for 6 hours followed by air cooling. (a) General micrograph (b) Higher magnification micrograph showing the extensive precipitation of secondary carbides in an austenitic matrix.

The electron micrographs better illustrate the extent of secondary carbide precipitation, Figure 5.29. The back scattered electron micrograph, Figure 5.29(b) shows that the precipitation of secondary carbides occurs extensively throughout the matrix. The secondary carbides are separated from the primary and eutectic carbides. The high magnification secondary electron image, Figure 5.29, shows that the morphology of the secondary carbides are rod like up to 5μm in length or have a cubic appearance and are sub micron in size.

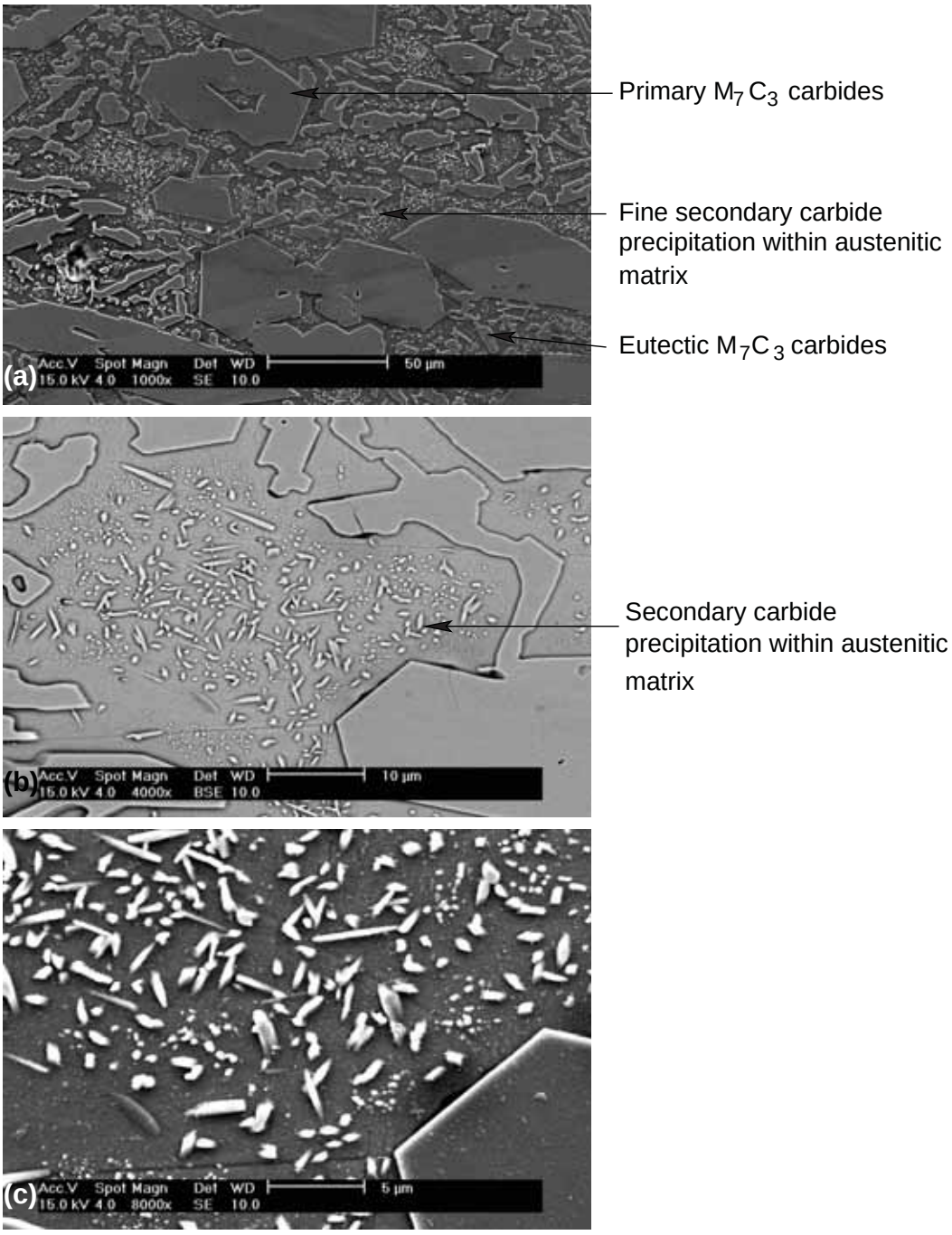

Figure 5.29: Electron micrographs of the HyperEXP after heat treatment at 950°C for 6 hours followed by air cooling. (a) Secondary electron micrograph showing the extensive secondary carbide precipitation (b) Back scattered electron micrograph showing that the primary and eutectic carbides have not undergone any changes. (c) Secondary electron micrograph showing secondary carbide morphology.

The microstructure after the 1150°C heat treatment is shown in Figure 5.30. The heat treated alloy was non magnetic and therefore has a fully austenitic matrix. Limited secondary carbide precipitation was found to occur, Figure 5.30(b). The back scattered electron micrograph, Figure 5.31, also shows that the matrix is homogeneous, that there is isolated secondary carbides and the primary and eutectic carbides have not undergone any changes.

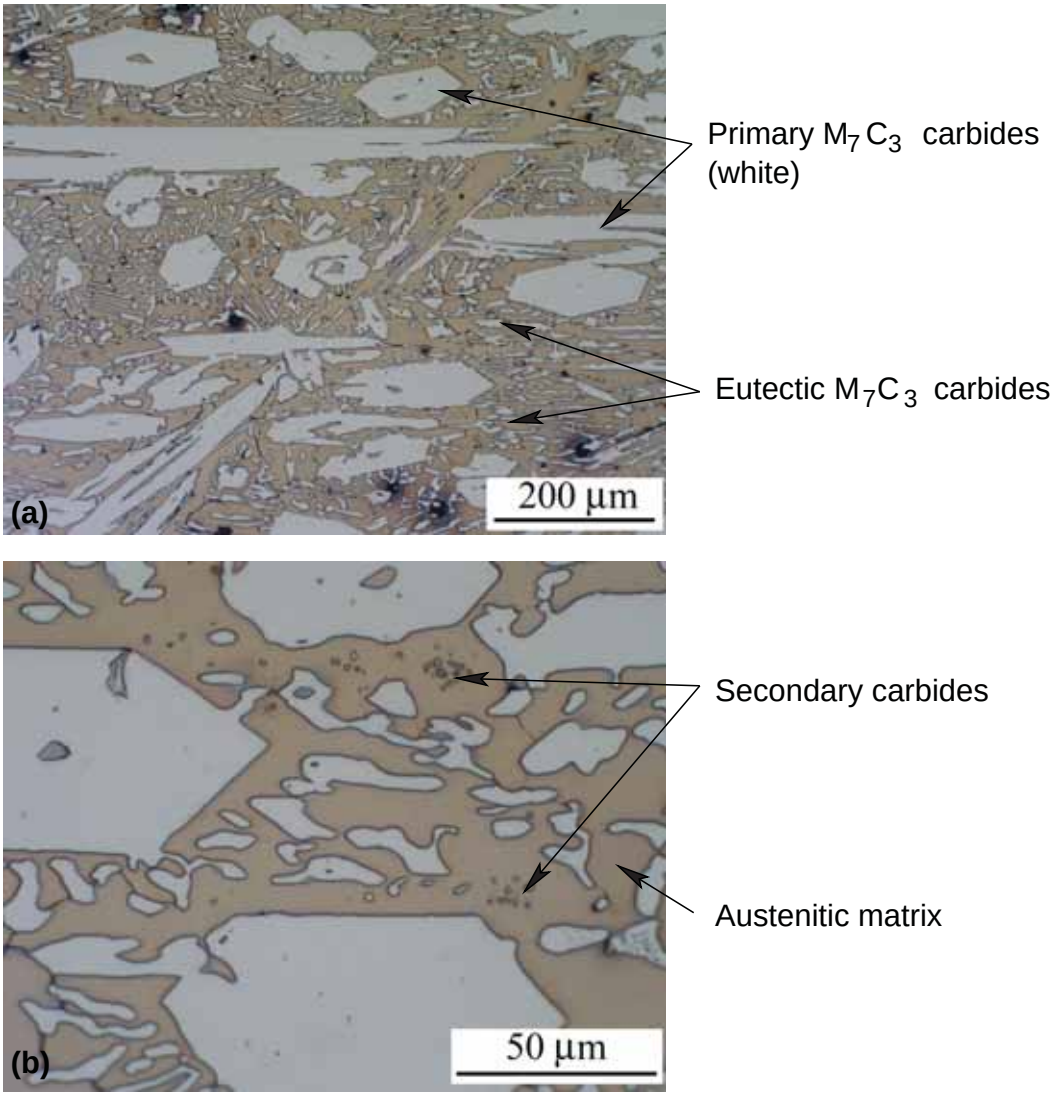

Figure 5.30: Optical micrographs of the HyperEXP castings after heat treatment at 1150°C for 6 hours followed by air cooling. (a) General micrograph (b) Higher magnification micrograph showing limited secondary carbide precipitation in an austenitic matrix.

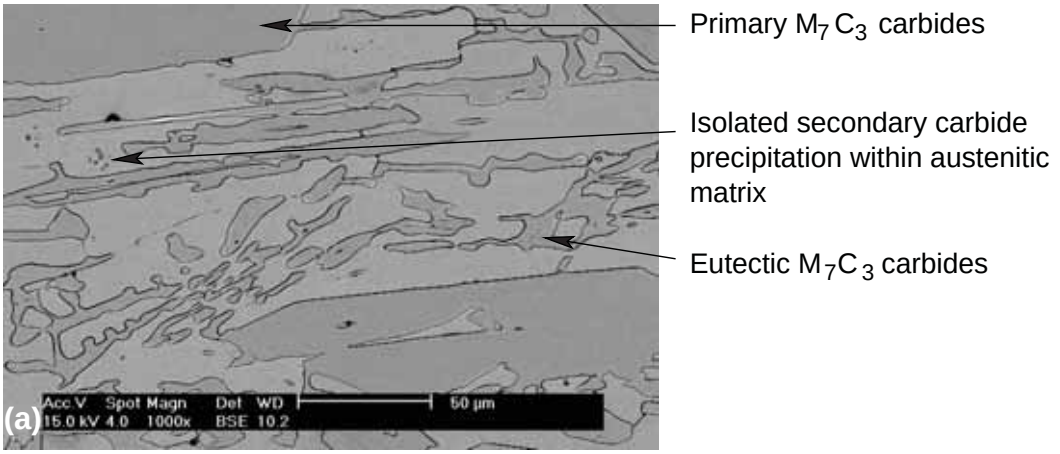

Figure 5.31: Back scattered electron micrographs of the HyperEXP after heat treatment at 1150°C for 6 hours followed by air cooling. Micrograph shows that the primary and eutectic carbides have not undergone any changes and isolated regions of secondary carbides.

The chemical composition of the matrix after the 950°C and 1150°C heat treatments are given in Table 5.18. The matrix of the 950°C heat treated alloy contained 0.76% carbon and 5.8% chromium. The silicon content was 0.9%, manganese 5.9%, nickel 8.8% and the molybdenum 0.3%. After the 1150°C heat treatment, the matrix composition of carbon had increased by 0.2% to 0.9% and chromium by 3% to 8.6%. The silicon and nickel composition decreased slightly by 0.1% and 0.3% respectively. The manganese and molybdenum composition were unchanged.

The chemical compositions of the primary and eutectic M_7C_3 carbides were also analyzed for the 1150°C heat treatment condition to determine if any change in composition had occurred, Table 5.18. Comparison of the chemical composition values with those for the as-cast condition, Table 5.6, finds that there are no significant variations.

Table 5.18: Chemical compositions of the matrix for the HyperEXP casting after heat treatment at 950 and 1150°C for 6 hours followed by air cooling and the chemical composition of the primary and eutectic carbides for the 1150°C heat treated condition.

HyperEXP		Chemical Composition wt%						
		C	Si	Cr	Mn	Fe	Ni	Mo
950°C for 6 hours "Destabilized"	Matrix	0.76 ± 0.08	0.91 ± 0.03	5.82 ± 0.44	5.87 ± 0.47	79.71 ± 0.52	8.79 ± 0.72	0.26 ± 0.14
1150°C for 6 hours "Normalized"	Primary M_7C_3 carbides	8.59 ± 0.18	0.01 ± 0.01	54.42 ± 0.82	4.34 ± 0.14	32.86 ± 0.70	0.58 ± 0.09	0.31 ± 0.04
1150°C for 6 hours "Normalized"	Eutectic M_7C_3 carbides	8.28 ± 0.14	0.01 ± 0.01	45.40 ± 1.21	7.10 ± 0.54	38.34 ± 0.45	0.63 ± 0.14	0.90 ± 0.31
1150°C for 6 hours "Normalized"	Matrix	0.92 ± 0.08	0.82 ± 0.03	8.62 ± 0.47	5.81 ± 0.44	76.50 ± 0.61	8.43 ± 0.41	0.28 ± 0.10

The bulk hardness and matrix microhardness results for the 950 and 1150°C heat treatment conditions are given in Table 5.19. The bulk hardness of the 950°C heat treated alloy, having a matrix of secondary carbides and austenite, was measured to be 464 HV. The bulk hardness

of the 1150°C heat treated alloy, having a matrix of austenite and limited secondary carbides, was measured to be 466 HV. The microhardness of the matrix was also similar for the two heat treatment conditions being 395 and 370 HV for the 950°C and 1150°C heat treatment conditions respectively.

Table 5.19: Bulk hardness and microhardness of the matrix after heat treatment at 950 and 1150°C for the HyperEXP casting.

HyperEXP		
Heat Treatment	Bulk hardness (HV_{30})	Microhardness Matrix ($HV_{0.3\ \&\ 0.1}$)
950°C for 6 hrs - Destabilized	464±14	393±10
1150°C for 6 hrs - Normalized	466±10	368±35

5.4 Summary

The microstructures of the high chromium white irons samples used for corrosion and wear testing have been reviewed. These comprised four castings ranging in composition from hypoeutectic to hypereutectic. Two hypereutectic weld overlays were also examined. Heat treatments typical of a destabilization heat treatment at 950°C and a high temperature normalizing heat treatment at 1150°C followed by air cooling were done on the four castings to investigate the influence of heat treatment on microstructure.

The metallographic examination involved optical light microscopy and electron microscopy. The bulk chemical composition along with the micro chemical compositions of the carbide and matrix phase, determined by EPMA, was reported. The bulk hardness of the alloys and of the carbide and matrix phase, was reported where possible.

The weld overlays were found to have varying microstructures that required examination of different sample orientation to gain a better understanding of the carbide morphology and microstructural development. The branched primary and complex regular carbide morphologies were seen in the weld overlays but not seen in the castings. The size and distribution of the primary and eutectic M_7C_3 carbides in the weld overlays was much smaller than the hypereutectic castings.

Heat treatments on the castings found that the hardness was increased by undertaking a destabilization heat treatment at 950°C as transformation of the prior austenite matrix to martensite would occur. However, the exception to this was the HyperEXP alloy which could not be hardened by conventional heat treatments. The high temperature heat treatment at 1150°C resulted in a homogeneous matrix of austenite with limited secondary carbides. With the exception of the Hyper EXP alloy, the high temperature heat treated alloys still showed a slight attraction to a magnet indicating the presence of some martensite (note:

martensite is the most likely ferromagnetic phase as ferrite (e.g. pearlite) is highly unlikely to form after the 1150^{o}C heat treatment due to the higher alloy content of the matrix).